DISSERTATION

EXPLORING PHASE SELECTIVITY AND MORPHOLOGICAL CONTROL IN Cu-Sb-Se NANOPARTICLE SYNTHESIS

Submitted by

Amanda R. Kale

Department of Chemistry

In partial fulfillment of the requirements

For the Degree of Doctor of Philosophy

Colorado State University

Fort Collins, Colorado

Summer 2023

Doctoral Committee

Advisor: Amy L. Prieto

Justin Sambur
Amber Krummel
Kaka Ma

ABSTRACT

EXPLORING PHASE SELECTIVITY AND MORPHOLOGICAL CONTROL IN Cu-Sb-Se NANOPARTICLE SYNTHESIS

Nanoparticles are used in a variety of applications, such as optoelectronics, medicine, and energy generation and storage. Different applications necessitate different nanoparticle compositions and morphologies. Thus, developing fine synthetic control over composition, phase, and morphology is of interest to the field. Solution-phase nanoparticle synthesis allows control over particle shape and size, though phase purity is often an issue in ternary syntheses. Often precursor reactivity must be balanced to avoid binary sinks; however, in the Cu-Sb-Se system, the ternaries compete with one another. In this dissertation we explore the knobs of a hot-injection synthesis in oleylamine that can be tuned to favor different Cu-Sb-Se ternary phases and control particle morphologies.

In Chapter I we begin with a discussion of the term precursor reactivity and how we define it here. We also address the common frameworks used to explain reactivity, and the specific challenges of balancing reactivity in multinary chalcogenide syntheses. We also discuss how these challenges manifest in the Cu-Sb-Se system, and why the structures and phase space of this material are interesting to study. In Chapter II we discuss a guide for fitting X-ray diffraction data for complex nanomaterial systems, outlining important considerations when working on the nanoscale as well as our sequential approach to refinements and recommended best practices. We also discuss a case study on the refinements of anisotropic, multiphase systems, which we use for the following chapter. The main synthetic work follows in the next two chapters, focusing first in

Chapter III on the decomposition of metastable Cu_3SbSe_3 to thermodynamic $CuSbSe_2$. We investigate how this can be manipulated through the addition of an amide base. In Chapter IV, we explore tuning morphology and specifically nanosheet branching in $CuSbSe_2$, in which we show that we can induce twinning in $CuSbSe_2$ and initial characterization suggests that this occurs in a different manner than in the very similar sulfide system. Finally, in Chapter V we reflect on the considerations and next steps for this work, including preliminary results on the use of soft base ligands to complex Cu, as well as on promising directions of field of nanoparticle synthesis as a whole.

ACKNOWLEDGEMENTS

I would like to extend a huge thank you my lab mates in the Prieto Group, as I could not see myself finishing my PhD without their support, both through tearful meetings and rigorous scientific discussions. I am extremely grateful to have had Kelly Nieto working on her dissertation by my side—knowing that I was not alone in this process made a world of difference. I would like to thank my advisor, Amy Prieto, for always having my best interests at heart, pushing me to do my best work and encouraging me to rise to new challenges. I would also like to thank my friends outside of the Prieto group, my a cappella group, and my family for always being there to support me and reminding me that life exists outside of chemistry.

TABLE OF CONTENTS

CHAPTER I: CONSIDERATIONS FOR PRECURSOR REACTIVITY IN Cu-Sb-Se NANOPARTICLE SYNTHESIS

1.1 The role of precursor reactivity in tuning nanoparticle syntheses

Synthesizing new semiconductor materials through the use of colloidal nanoparticle synthesis is appealing due to the large degree of control that can be obtained over particle size, size distribution, and morphology.[1,2] Additionally, nanocrystal syntheses can allow access to low temperature synthetic routes and access to metastable phases that bulk synthetic routes cannot.[3–5] In nanoparticle synthesis, a variety of parameters are involved, such as reaction time and temperature, and the identity and concentration of the components in the reaction, which can be tuned like the knobs on a radio to alter the products obtained (Figure 1.1).

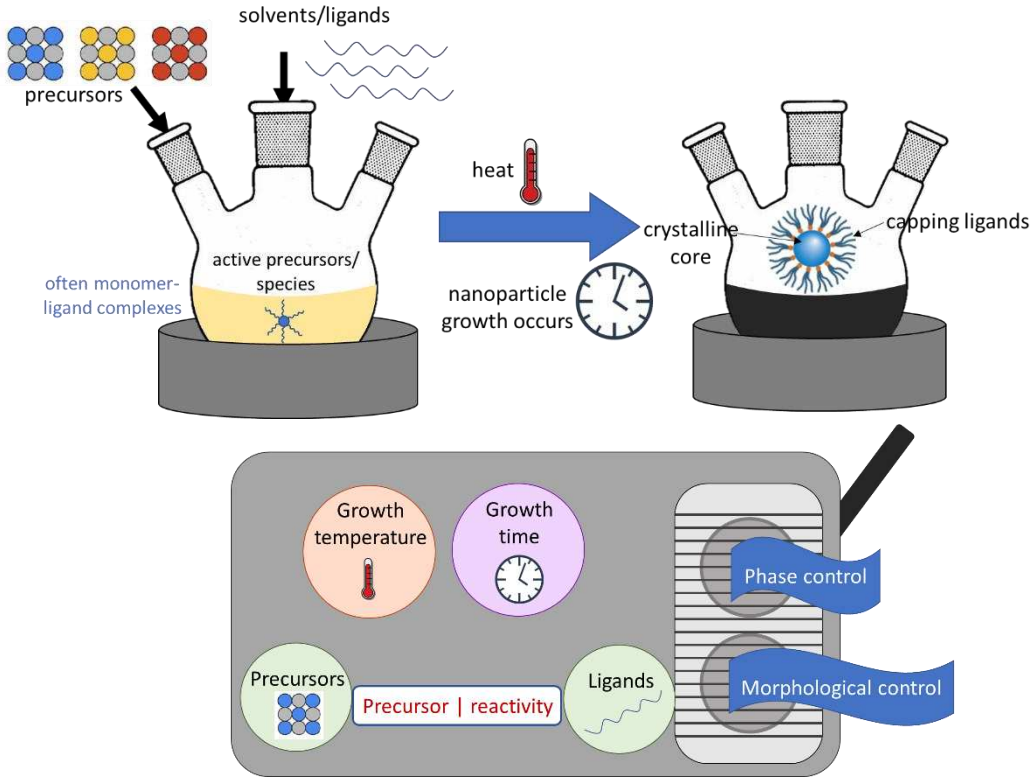

Figure 1.1. Pictoral representation of the parameters involved in nanoparticle synthesis.

Upon combining solid precursors, ligands, and solvents in solution, either before or after heating, metal-ligand complexes are often observed.[6] The formation and decomposition of these species greatly affects nanoparticle nucleation and growth,[7] which in turn affects the particle phase and morphology observed. In particular, the interaction between precursors and ligands can be tuned to alter the complexes that form, thus tuning their reactivity.[6] The species that form just prior to nucleation are can be called "active species"[8] or here we refer to "active complexes," to clarify the difference between the starting precursors and those that have formed *in situ* and are likely to influence particle nucleation and growth.

Descriptions of reactivity are often vague and have been historically hypothesized from reaction products, rather than directly characterized. For example, when certain reaction conditions result in a phase that is Cu-rich, one says that the Cu precursor must have been more reactive. When "reactivity" is used to describe precursors in literature, it can either mean that the starting precursor itself is extremely reactive or that the active species formed from that precursor is very reactive. It is often not specified which is the case and must be inferred, which can result in a clouded understanding of reactivity, given the complicated interactions that can occur between precursors, ligands, and solvents.[9] Describing reactivity with greater specificity as it relates to reaction pathways, and the conversion from precursors to intermediates to final products, whether hypothesized or characterized, is crucial if we wish to develop strategies for predicting reactivity in new systems, as has been emphasized in recent reviews.[9,10] Here, we focus on the role of metal-ligand complexes, and how their hypothesized reactivity can be used to control reaction phase and morphology. In this work, while we are only hypothesizing about the active species that are present, we define the term precursor reactivity as the stability of the active complex/species that forms just prior to nanocrystal nucleation. For example, a less stable active complex, with easily

dissociating leaving groups, will be more likely to decompose and have its atom incorporate into a nanocrystal structure and this precursor is defined as more reactive.

When the identity of active species is not known, two frameworks are commonly used to hypothesize their reactivity: hard-soft acid base (HSAB) theory and bond dissociation energies (BDEs). In HSAB theory, harder cations, which are small and highly charged, are expected to coordinate preferentially to harder ions or ligands, and vice versa. This makes hard-hard or soft-soft pairings more stable and less likely to decompose to allow atom incorporation into a structure than a soft-hard pairing. In Cu-M-S nanoparticles, Mantella et al. found that the reactivity of the Cu precursor had to be tuned according to the thiophilicity of the M cation in order to synthesize the desired ternary phase as opposed to binary M-S phases.[11] The stability of the Cu precursors, CuI, Cu(OAc), Cu(acac), can be rationalized with HSAB theory, with the soft-soft pairing of CuI being the most stable precursor and least reactive. This framework is commonly used to rationalize reactivity of metal-ligand complexes as well. In a $CuInS_2$ synthesis, Cu-S binaries formed when hard ligands such as carboxylic acids were used, as the unfavorable soft Cu^+ and hard carboxylic acid pairing likely led to an unstable coordination complex.[12] The ternary was isolated by stabilizing Cu^+ with soft thiol ligands, thus suppressing Cu reactivity and allowing incorporation of Cu and In at similar rates, favoring ternary formation over Cu-S binaries. The HSAB framework is commonly used in ternary copper chalcogenide systems like this one and more examples will be discussed in the following section.

Bond dissociation energies can be used to assess how easily a bond will break, which also correlates to how quickly atoms will incorporate into a given structure. We have seen the use of BDEs to rationalize precursor reactivity most commonly used for organo-chalcogenides.[13–15] The Vela group calculated C-S and S-S bond energies and determined that C-S bond strength could be

manipulated to yield shape control in CdS nanocrystals.[13] They hypothesized the relative rate of formation of R-S and S radicals based on BDEs, which they were able to use to predict particle morphology obtained with combinations of different organosulfide precursors. Building upon this work from Guo et al., Tappan et al. found that the C-Se bond strength directed the Cu-Se binary formed, which then led to a thermodynamic or metastable $CuInSe_2$ phase.[14] In metal dichalcogenide syntheses, characterization of species via NMR along with BDEs allowed Kapuria et al. to estimate S reactivity and in turn rationalize or predict the formation of metastable polymorphs.[15] These studies show that while the active species and kinetics were not directly characterized/measured, BDEs can be used as a framework to estimate the rate of active species formation (chalcogenide radicals) to be estimated, which allowed for the rationalization or prediction of phases formed. Unfortunately for primarily synthetic groups, use of BDEs as a predictive tool requires that values are known in the literature or collaboration with computational groups to calculate BDEs.

1.2 Balancing reactivity in multivalent ternary chalcogenide NP synthesis

As mentioned previously, the hard-soft acid base framework is commonly used to discuss reactivity in multivalent, ternary chalcogenide syntheses, as one cation is often harder than the other. When only one ligand is present, it will often preferentially coordinate to one cation over the other and often results in the formation of binary phases or solid solutions rich in one cation.[16] The Cu-Sb-Se system that will be discussed in this work is an example, as the Cu^+ is much softer than Sb^{3+}. Two methods are generally used to overcome this challenge in M^+/M^{3+} reactivity imbalance, as have been detailed in reviews on copper chalcogenides.[16,17]

In the first method, amide-promoted synthesis, an amide salt is usually co-injected with the chalcogenide at elevated temperatures forming reactive metal-amide intermediates. The goal of using amide precursors is to make both cationic precursors so reactive that differences in hardness are negated. The Brönsted base lithium bis(trimethylsilylamide) (LiHMDS) has been used to form reactive complexes in syntheses with trioctylphosphine (TOP)[18–20] as well as oleylamine (OLA),[21,22] creating reactive metal silylamide or oleylamide complexes in solution.[23,24] Upon addition of silylamide to oleylamine, an equilibrium forms between the oleylamine, silylamide, deprotonated oleylamide, and silylamine. As such, the complexes formed can be either metal-oleylamine, metal-oleylamide, or metal-silylamide complexes (Figure 1.2).[23] Some metals have a stronger preference for the metal-oleylamide coordination than others, and complexes vary in stability depending on the metal. In the case of Sn, the metal-oleylamide complex is strongly favored and Sn-silylamide complex is not observed by ^{1}H-NMR or ^{119}Sn NMR.[23,25] Other metals, such as In, did not show a strong preference for the metal-oleylamide complex until a high concentration of silylamide was added.[23] In a study by He et al., only "stable" metal-amide complexes were characterized; other complexes, including those of Bi^{3+}, Cu^{+}, Sb^{3+}, and Zn^{2+} were deemed "unstable" if they reduced rapidly under reaction conditions upon the injection of base and were not characterized.[23] Despite minimal knowledge of their complexation, Cu^{+} and Sb^{3+} "unstable" oleylamides have been used in syntheses, and reactivity has been successfully balanced to obtain desired compositions.[22,26] Given the expected high reactivity of Cu^{+} and Sb^{3+} oleylamide

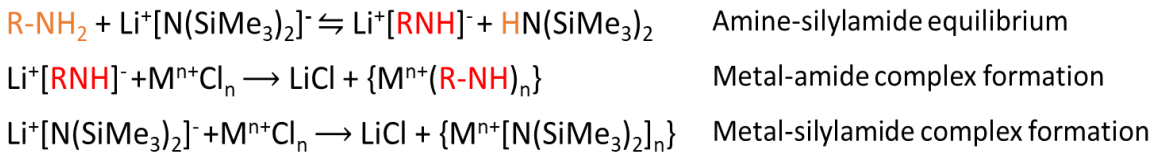

Figure 1.2 Series of equations showing how the competing amine-silylamide equilibrium can result in either metal-amide or metal-silylamide complexes.

complexes, we test the amide-promoted approach as a method of controlling precursor reactivity in a hot-injection Cu-Sb-Se synthesis.

Another method used to control reactivity in multivalent chalcogenide systems is to selectively stabilize each cation with favorable ligand interactions, resulting in strong metal-ligand bonds and stable complexes for each cation. In this type of synthesis, hard-hard or soft-soft pairings are desired. In the Cu-Sb-S system, controlling the ratio of soft dodecanethiol to hard (when deprotonated) oleic acid allowed the Cu:Sb ratio in the product to be controlled.[27] The soft dodecanethiol binds strongly to the soft Cu(I) and the oleic acid to the Sb(III). Alkanethiol-mediated is the specific name given to this type of synthesis, most commonly used for sulfur ternaries, as the thiol can also be used as the S precursor. This method has been successful in some selenide systems due to the strong coordination of the soft sulfur to the soft cation (often Cu), as long as temperatures are not high enough to cause the alkanethiol to decompose.[28] As we use lower reaction temperatures in our syntheses, we have been able to use this approach for some reactions without observing unwanted thiol incorporation.

1.3 Motivation for the study of Cu-Sb-Se materials

1.3.1 Applications and structural distinctions

The Cu-Sb-Se family of materials is notable for their energy-relevant applications. In the Cu-Sb-Se phase space, three ternary phases have been observed as minerals and synthesized experimentally: Cu_3SbSe_4, Cu_3SbSe_3, and $CuSbSe_2$. All three phases are p-type semiconductors[29,30] due to the susceptibility of Cu vacancies, [31] resulting in an increase in hole carriers. The $CuSbSe_2$ phase has been explored for photovoltaic[32,33] and thermoelectric applications,[34–36] and Cu_3SbSe_3 and Cu_3SbSe_4 have been explored for applications in thermoelectrics.[37,37–39] As the potential for the Cu-Sb-Se phases as photovoltaic absorbers has been

reviewed extensively elsewhere,[29,30] here we discuss their structural features in context of their thermoelectric properties.

The crystal structures of the selenide ternaries, as well as their isostructural sulfur analogues, are shown in figure 1.3. Because of the isostructural chalcogenide phases, solid solutions can be formed by substituting sulfur in for selenium and have been synthesized for $CuSbSe_{2-x}S_x$ and $Cu_3SbSe_{4-x}S_x$ solid solutions offer a unique opportunity for tunable optical and electronic properties depending on the degree of substitution that occurs.[40–42]

The phase with the highest symmetry is that of Cu_3SbSe_4, crystallizing in the tetragonal *I-42m* space group, with corner-sharing tetrahedra of $CuSe_4$ and $SbSe_4$. The symmetric connectivity and lack of Sb lone pair gives it the highest electronic and thermal conductivity of the three ternaries,[43] and dopants are added to increase phonon scattering and decrease thermal

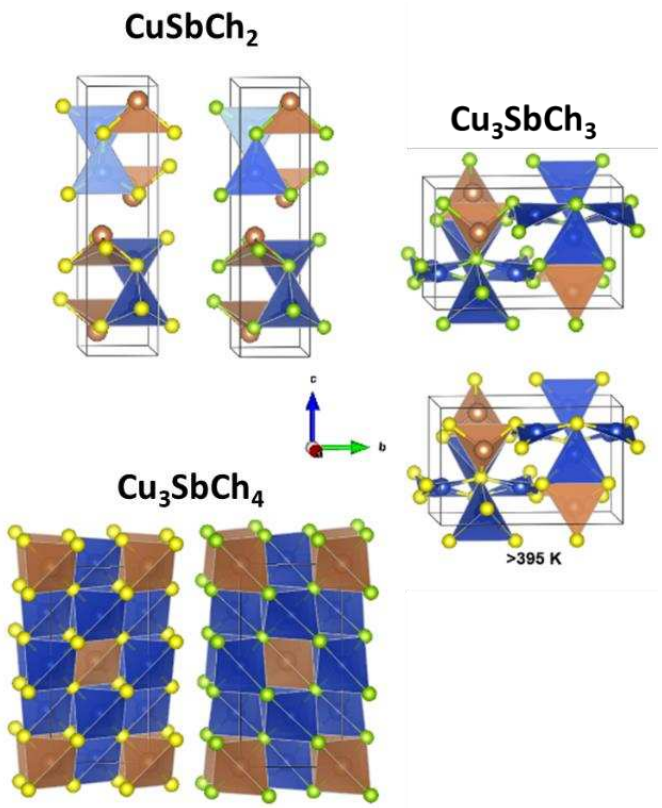

Figure 1.3. Crystal structures of the Cu-Sb-Se phases and their S analogues. Blue is Cu, brown is Sb, yellow is S and green is Se.

conductivity[37,38,44] to further increase the thermoelectric figure of merit, ZT. $CuSbSe_2$ and Cu_3SbSe_3 both exhibit the lower symmetry of the orthorhombic *Pnma* space group. The most Sb-rich phase, $CuSbSe_2$, exhibits the chalcostibite structure-type with $CuSe_4$ tetrahedra and $SbSe_3$ trigonal pyramids caused by the lone pair on Sb^{3+}, resulting in a van der Waals interlayer gap. Cu_3SbSe_3 is the most copper-rich and most selenium-deficient and contains the same $SbSe_3$ trigonal pyramids, as well as $CuSe_3$ trigonal polyhedral and $CuSe_4$ tetrahedra. Rather than existing in a rigid sublattice, the Cu ions seems to exhibit "liquid-like" characteristics at and above room-temperature,[45,46] as shown in figure 1.4. Because of this, Rietveld refinements can result in large Cu displacement parameters and low occupancies,[46] which we have seen in our own Rietveld refinements on this material. The Sb^{3+} lone pairs in both $CuSbSe_2$ and Cu_3SbSe_3 lead to a high level of anharmonicity and therefore low thermal conductivity in both phases, though the higher degree of anharmonicity and disorder in Cu_3SbSe_3 leads to even lower conductivity.[43]

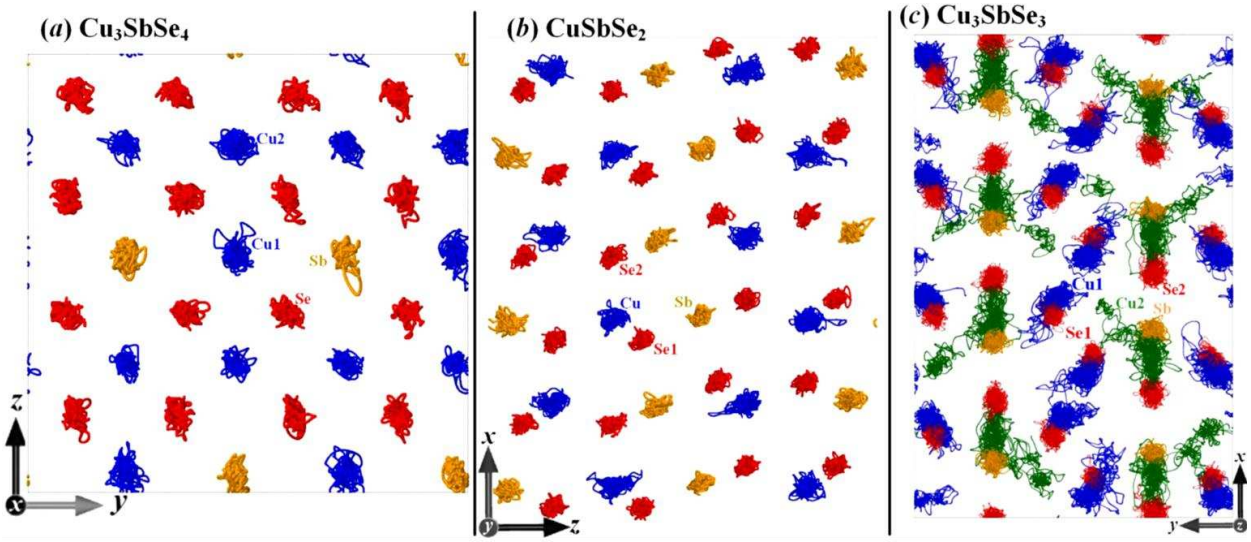

Figure 1.4. Atom trajectories from molecular dynamics simulations for (a) Cu_3SbSe_4, (b) $CuSbSe_2$, and (c) Cu_3SbSe_3 at 400 K. Reproduced from Ref 45.

In all phases, it is generally accepted that the oxidation states are Cu^{+} and Se^{2-}, with Cu_3SbSe_4, containing $Sb^{5+,}$ and the other two phases containing Sb^{3+}. However, the presence of Cu^{2+} and Sb^{3+} alongside the commonly observed oxidation states have been observed for Cu_3SbSe_4,[44] though we note that this could possibly be due to slight oxidation of the material. As mentioned previously, the Sb^{3+} has a $5s^2$ lone pair that results in substantial structural distortions (Figure 1.5). The presence of the Sb^{3+} lone pair in both the di- and triselenide phases seems to be the driving factor for the anisotropic growth observed in these nanoparticles,[34,47] which makes the study of nanoparticle morphology in these phases of interest.

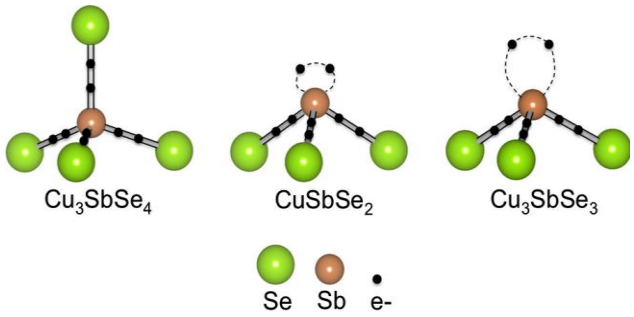

Figure 1.5. Illustration of Sb coordination environments for all three ternaries, showing the steric effect caused by the Sb^{3+} lone pair. Reproduced from Ref 43.

1.3.2 Cu-Sb-Se phase space and previous syntheses

The complex phase space of this family leads to synthetic challenges. These three phases exist close in atomic composition and exhibit similar formation energies (figure 1.6). Cu_3SbSe_3 phase has a formation energy above the hull, as shown in Figure 1.6b, which means that at that a composition of Cu:Sb:Se of 3:1:3, this phase is unstable and expected to decompose.[48] Based solely on formation energies, it is expected to decompose into the thermodynamically stable phases $CuSbSe_2$, Cu_3Se_2, and Cu.[48] The other two ternaries are thermodynamically stable, with lower formation energies and a value of 0 for energy above the hull, meaning these phases are the most stable at their given compositions.

Challenges with phase impurities have been observed in Cu-Sb-Se nanoparticle syntheses, which are commonly other ternaries, but are also Sb_2Se_3 and Cu_2Se. [37,47,49] Colloidal $CuSbSe_2$ nanocrystals have been synthesized as both sheets[34,40,41] and spheres.[50] Most colloidal Cu_3SbSe_4 nanocrystals have been synthesized as spheres[37,39,50,51] and Cu_3SbSe_3 nanoparticles have been synthesized as spheres[52] and disks.[47] Despite a multitude of published syntheses, the conditions favoring the different ternary phases have not been identified. The complex nature of this system nature requires fine control over precursor reactivity in order to be able to tune between different phases and morphologies, making it an ideal model system for exploration.

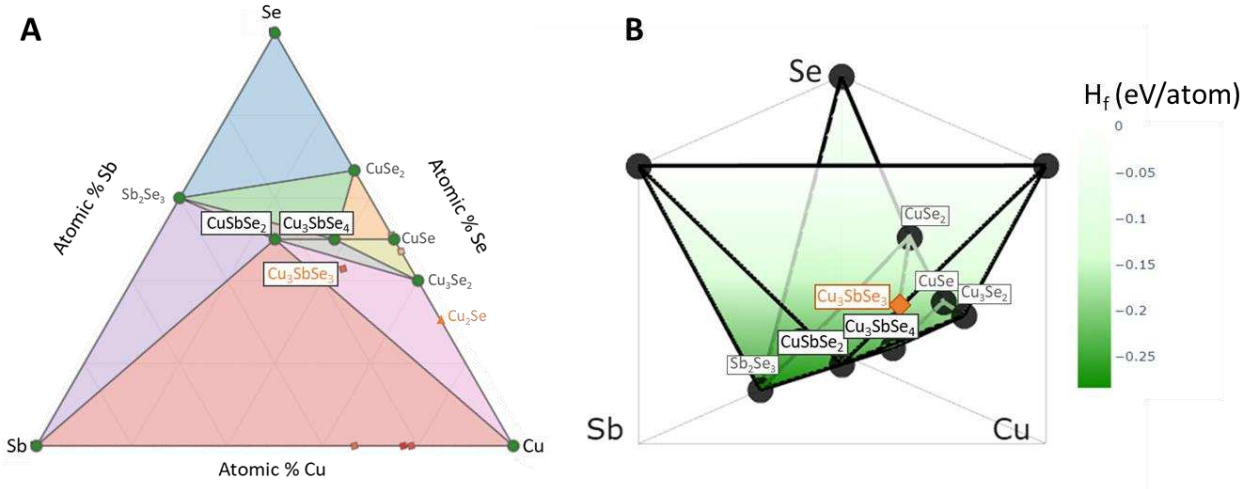

Figure 1.6. Ternary phase diagrams at 0 K for the Cu-Sb-Se system. Metastable phases of interest are shown in orange. Adapted from ref 48.

1.4 Chapter outline

Chapter II is a methodology paper prepared for submission in Chemistry of Materials that discusses considerations for performing Rietveld refinements on nanoscale materials. We outline a sequential approach to refinements to allow for the most relevant parameters to be included. We discuss specific case studies, including the use of a model for anisotropic crystalline domains to perform refinements on anisotropic, multiphase systems, which was used on X-ray diffraction patterns of the nanoparticles synthesized in Chapter III.

Chapter III has been accepted as a communication in Nano Letters and focuses on the conversion of the metastable Cu_3SbSe_3 to the more thermodynamically stable $CuSbSe_2$ in a hot-injection synthesis in oleylamine.[53] We characterize particle phase and morphology through transmission electron microscopy (TEM) and X-ray diffraction (XRD), and we quantify the changes that occur over time through Rietveld refinements of XRD patterns, using the method discussed in the previous chapter. Additionally, we attempt to tune precursor reactivity with the addition of the amide base LiHMDS, hoping to form reactive metal-amide complexes. Interestingly, under our reaction conditions, Cu_3SbSe_3 was always present in the initial aliquot, perhaps suggesting that Cu remains too reactive and Sb reactivity cannot be increased with this amide base. It is also possible that Cu_3SbSe_3 formation is favored as a Se deficient phase. Future work could involve exploring different selenium precursors in this synthesis.

Chapter IV discusses morphological control in $CuSbSe_2$, and specifically investigates attempts to control and characterize nanosheet branching under different synthesis conditions. Characterization of nanosheets through electron microscopy and electron diffraction suggests that branching results from a twinned particle core. We use two approaches to induce twinning: an alkanethiol-promoted approach and an amide-promoted approach. Surprisingly, electron diffraction shows that $CuSbSe_2$ does not twin along the plane as has been reported in literature. We propose potential twin planes, though additional characterization across this boundary is needed to support a specific plane.

Chapter V summarizes the work presented on phase and morphological control in Cu-Sb-Se nanoparticles. We discuss future directions needed for the work presented with a particular emphasis on characterization of active complexes. Additionally, we discuss preliminary work regarding control of Cu complexes with soft bases. Throughout this dissertation we hope to show

that working towards a more specific understanding of reactivity and speciation as it relates to reaction pathway in individual systems, such as the Cu-Sb-Se system, will eventually lead to a more comprehensive understanding of how different precursors control products in different systems, which could lead to a broader understanding of how to manipulate reactivity in new nanoparticle systems.

References

(1) Yin, Y.; Alivisatos, A. P. Colloidal Nanocrystal Synthesis and the Organic–Inorganic Interface. *Nature* **2005**, *437* (7059), 664–670. https://doi.org/10.1038/nature04165.

(2) Murray, C. B.; Norris, D. J.; Bawendi, M. G. Synthesis and Characterization of Nearly Monodisperse CdE (E = Sulfur, Selenium, Tellurium) Semiconductor Nanocrystallites. *J. Am. Chem. Soc.* **1993**, *115* (19), 8706–8715. https://doi.org/10.1021/ja00072a025.

(3) Chen, C.-C.; Herhold, A. B.; Johnson, C. S.; Alivisatos, A. P. Size Dependence of Structural Metastability in Semiconductor Nanocrystals. *Science* **1997**, *276* (5311), 398–401. https://doi.org/10.1126/science.276.5311.398.

(4) Grünwald, M.; Lutker, K.; Alivisatos, A. P.; Rabani, E.; Geissler, P. L. Metastability in Pressure-Induced Structural Transformations of CdSe/ZnS Core/Shell Nanocrystals. *Nano Lett.* **2013**, *13* (4), 1367–1372. https://doi.org/10.1021/nl3007165.

(5) Manna, L.; Milliron, D. J.; Meisel, A.; Scher, E. C.; Alivisatos, A. P. Controlled Growth of Tetrapod-Branched Inorganic Nanocrystals. *Nat. Mater.* **2003**, *2* (6), 382–385. https://doi.org/10.1038/nmat902.

(6) Heuer-Jungemann, A.; Feliu, N.; Bakaimi, I.; Hamaly, M.; Alkilany, A.; Chakraborty, I.; Masood, A.; Casula, M. F.; Kostopoulou, A.; Oh, E.; Susumu, K.; Stewart, M. H.; Medintz, I. L.; Stratakis, E.; Parak, W. J.; Kanaras, A. G. The Role of Ligands in the Chemical Synthesis and Applications of Inorganic Nanoparticles. *Chem. Rev.* **2019**, *119* (8), 4819–4880. https://doi.org/10.1021/acs.chemrev.8b00733.

(7) Whitehead, C. B.; Finke, R. G. Particle Formation Mechanisms Supported by in Situ Synchrotron XAFS and SAXS Studies: A Review of Metal, Metal-Oxide, Semiconductor and Selected Other Nanoparticle Formation Reactions. *Mater. Adv.* **2021**, *2* (20), 6532–6568. https://doi.org/10.1039/D1MA00222H.

(8) Lee, J. M.; Miller, R. C.; Moloney, L. J.; Prieto, A. L. The Development of Strategies for Nanoparticle Synthesis: Considerations for Deepening Understanding of Inherently Complex Systems. *J. Solid State Chem.* **2019**, *273*, 243–286. https://doi.org/10.1016/j.jssc.2018.12.053.

(9) De Roo, J. Chemical Considerations for Colloidal Nanocrystal Synthesis. *Chem. Mater.* **2022**, *34* (13), 5766–5779. https://doi.org/10.1021/acs.chemmater.2c01058.

(10) Loiudice, A.; Buonsanti, R. Reaction Intermediates in the Synthesis of Colloidal Nanocrystals. *Nat. Synth.* **2022**, *1* (5), 344–351. https://doi.org/10.1038/s44160-022-00056-x.

(11) Mantella, V.; Varandili, S. B.; Pankhurst, J. R.; Buonsanti, R. Colloidal Synthesis of Cu−M−S (M = V, Cr, Mn) Nanocrystals by Tuning the Copper Precursor Reactivity. *Chem. Mater.* **2020**, *32* (22), 9780–9786. https://doi.org/10.1021/acs.chemmater.0c03788.

(12) Xie, R.; Rutherford, M.; Peng, X. Formation of High-Quality I−III−VI Semiconductor Nanocrystals by Tuning Relative Reactivity of Cationic Precursors. *J. Am. Chem. Soc.* **2009**, *131* (15), 5691–5697. https://doi.org/10.1021/ja9005767.

(13) Guo, Y.; Alvarado, S. R.; Barclay, J. D.; Vela, J. Shape-Programmed Nanofabrication: Understanding the Reactivity of Dichalcogenide Precursors. *ACS Nano* **2013**, *7* (4), 3616–3626. https://doi.org/10.1021/nn400596e.

(14) Tappan, B. A.; Barim, G.; Kwok, J. C.; Brutchey, R. L. Utilizing Diselenide Precursors toward Rationally Controlled Synthesis of Metastable CuInSe2 Nanocrystals. *Chem. Mater.* **2018**, *30* (16), 5704–5713. https://doi.org/10.1021/ACS.CHEMMATER.8B02205.

(15) Kapuria, N.; Nitish Patil, N.; Sankaran, A.; Laffir, F.; Geaney, H.; Magner, E.; Scanlon, M.; M. Ryan, K.; Singh, S. Engineering Polymorphs in Colloidal Metal Dichalcogenides: Precursor-Mediated Phase Control, Molecular Insights into Crystallisation Kinetics and Promising Electrochemical Activity. *J. Mater. Chem. A* **2023**, *11* (21), 11341–11353. https://doi.org/10.1039/D2TA09892J.

(16) Yarema, O.; Yarema, M.; Wood, V. Tuning the Composition of Multicomponent Semiconductor Nanocrystals: The Case of I–III–VI Materials. *Chem. Mater.* **2018**, *30* (5), 1446–1461. https://doi.org/10.1021/acs.chemmater.7b04710.

(17) Coughlan, C.; Iba, M.; Dobrozhan, O.; Singh, A.; Cabot, A.; Ryan, K. M. Compound Copper Chalcogenide Nanocrystals. Chem. Rev. **2017**, *117* (9), 5865–6109. https://doi.org/10.1021/acs.chemrev.6b00376.

(18) Yarema, O.; Bozyigit, D.; Rousseau, I.; Nowack, L.; Yarema, M.; Heiss, W.; Wood, V. Highly Luminescent, Size- and Shape-Tunable Copper Indium Selenide Based Colloidal Nanocrystals. *Chem. Mater.* **2013**, *25* (18), 3753–3757. https://doi.org/10.1021/cm402306q.

(19) Yarema, O.; Yarema, M.; Bozyigit, D.; Lin, W. M. M. M.; Wood, V. Independent Composition and Size Control for Highly Luminescent Indium-Rich Silver Indium Selenide Nanocrystals. *ACS Nano* **2015**, *9* (11), 11134–11142. https://doi.org/10.1021/acsnano.5b04636.

(20) Yarema, O.; Yarema, M.; Lin, W. M. M.; Wood, V. Cu-In-Te and Ag-In-Te Colloidal Nanocrystals with Tunable Composition and Size. *Chem. Commun.* **2016**, *52* (72), 10878–10881. https://doi.org/10.1039/c6cc05571k.

(21) Miller, R. C.; Neilson, J. R.; Prieto, A. L. Amide-Assisted Synthesis of Iron Germanium Sulfide (Fe_2GeS_4) Nanostars: The Effect of $LiN(SiMe_3)_2$ on Precursor Reactivity for Favoring Nanoparticle Nucleation or Growth. *J. Am. Chem. Soc.* **2020**, *142* (15), 7023–7035. https://doi.org/10.1021/jacs.0c00260.

(22) Moser, A.; Yarema, O.; Yarema, M.; Wood, V. Synthesis of Small Ag-Sb-Te Nanocrystals with Composition Control. *J. Mater. Chem. C* **2020**, *8* (45), 15985–15989. https://doi.org/10.1039/d0tc00880j.

(23) He, M.; Protesescu, L.; Caputo, R.; Krumeich, F.; Kovalenko, M. V. A General Synthesis Strategy for Monodisperse Metallic and Metalloid Nanoparticles (In, Ga, Bi, Sb, Zn, Cu, Sn, and Their Alloys) via in Situ Formed Metal Long-Chain Amides. *Chem. Mater.* **2015**, *27* (2), 635–647. https://doi.org/10.1021/cm5045144.

(24) Yarema, M.; Caputo, R.; Kovalenko, M. V. Precision Synthesis of Colloidal Inorganic Nanocrystals Using Metal and Metalloid Amides. *Nanoscale* **2013**, *5* (18), 8398–8410. https://doi.org/10.1039/c3nr02076b.

(25) Kravchyk, K.; Protesescu, L.; Bodnarchuk, M. I.; Krumeich, F.; Yarema, M.; Walter, M.; Guntlin, C.; Kovalenko, M. V. Monodisperse and Inorganically Capped Sn and Sn/SnO_2 Nanocrystals for High-Performance Li-Ion Battery Anodes. *J. Am. Chem. Soc.* **2013**, *135* (11), 4199–4202. https://doi.org/10.1021/ja312604r.

(26) Yarema, O.; Bozyigit, D.; Rousseau, I.; Nowack, L.; Yarema, M.; Heiss, W.; Wood, V. Highly Luminescent, Size- and Shape-Tunable Copper Indium Selenide Based Colloidal Nanocrystals. *Chem. Mater.* **2013**, *25* (18), 3753–3757. https://doi.org/10.1021/cm402306q.

(27) Liang, Q.; Huang, K.; Ren, X.; Zhang, W.; Xie, R.; Feng, S. Synthesis of Cu-Sb-S Nanocrystals: Insight into the Mechanism of Composition and Crystal Phase Selection. *Cryst. Eng. Comm.* **2016**, *18* (20), 3703–3710. https://doi.org/10.1039/c6ce00474a.

(28) Cassette, E.; Pons, T.; Bouet, C.; Helle, M.; Bezdetnaya, L.; Marchal, F.; Dubertret, B. Synthesis and Characterization of Near-Infrared Cu−In−Se/ZnS Core/Shell Quantum Dots for In Vivo Imaging. *Chem. Mater.* **2010**, *22* (22), 6117–6124. https://doi.org/10.1021/cm101881b.

(29) Peccerillo, E.; Durose, K. Copper—Antimony and Copper—Bismuth Chalcogenides—Research Opportunities and Review for Solar Photovoltaics. *MRS Energy Sustain.* **2018**, *5* (1), 1–59. https://doi.org/10.1557/mre.2018.10.

(30) De Souza Lucas, F. W.; Zakutayev, A. Research Update: Emerging Chalcostibite Absorbers for Thin-Film Solar Cells. *APL Mater.* **2018**, *6* (8), 084501. https://doi.org/10.1063/1.5027862.

(31) Welch, A. W.; Baranowski, L. L.; Zawadzki, P.; Lany, S.; Wolden, C. A.; Zakutayev, A. $CuSbSe_2$ Photovoltaic Devices with 3% Efficiency. *Appl. Phys. Express* **2015**, *8* (8), 082301. https://doi.org/10.7567/APEX.8.082301.

(32) Wang, C.; Yang, B.; Ding, R.; Chen, W.; Kondrotas, R.; Zhao, Y.; Lu, S.; Li, Z.; Tang, J. Reactive Close-Spaced Sublimation Processed $CuSbSe_2$ Thin Films and Their Photovoltaic Application. *APL Mater.* **2018**, *6* (8), 084801. https://doi.org/10.1063/1.5028415.

(33) Xue, D.-J.; Yang, B.; Yuan, Z.-K.; Wang, G.; Liu, X.; Zhou, Y.; Hu, L.; Pan, D.; Chen, S.; Tang, J. $CuSbSe_2$ as a Potential Photovoltaic Absorber Material: Studies from Theory to Experiment. *Adv. Energy Mater.* **2015**, *5* (23), 1501203. https://doi.org/10.1002/aenm.201501203.

(34) Luo, Y.; Du, C.; Liang, Q.; Zheng, Y.; Zhu, B.; Hu, H.; Khor, K. A.; Xu, J.; Yan, Q.; Kanatzidis, M. G. Enhancement of Thermoelectric Performance in $CuSbSe_2$ Nanoplate-Based Pellets by Texture Engineering and Carrier Concentration Optimization. *Small* **2018**, *14* (50), 1803092. https://doi.org/10.1002/smll.201803092.

(35) Li, D.; Qin, X. Y. Thermoelectric Properties of $CuSbSe_2$ and Its Doped Compounds by Ti and Pb at Low Temperatures from 5 to 310 K. *J. Appl. Phys.* **2006**, *100* (2), 023713. https://doi.org/10.1063/1.2218592.

(36) Zhang, D.; Yang, J.; Jiang, Q.; Fu, L.; Xiao, Y.; Luo, Y.; Zhou, Z. Ternary $CuSbSe_2$ Chalcostibite: Facile Synthesis, Electronic-Structure and Thermoelectric Performance Enhancement. *J. Mater. Chem. A* **2016**, *4* (11), 4188–4193. https://doi.org/10.1039/C6TA00039H.

(37) Liu, Y.; García, G.; Ortega, S.; Cadavid, D.; Palacios, P.; Lu, J.; Ibáñez, M.; Xi, L.; De Roo, J.; López, A. M.; Martí-Sánchez, S.; Cabezas, I.; Mata, M. de la; Luo, Z.; Dun, C.; Dobrozhan, O.; Carroll, D. L.; Zhang, W.; Martins, J.; Kovalenko, M. V.; Arbiol, J.; Noriega, G.; Song, J.; Wahnón, P.; Cabot, A. Solution-Based Synthesis and Processing of Sn- and Bi-Doped Cu_3SbSe_4 Nanocrystals, Nanomaterials and Ring-Shaped Thermoelectric Generators. *J. Mater. Chem. A* **2017**, *5* (6), 2592–2602. https://doi.org/10.1039/C6TA08467B.

(38) Li, D.; Li, R.; Qin, X. Y.; Song, C. J.; Xin, H. X.; Wang, L.; Zhang, J.; Guo, G. L.; Zou, T. H.; Liu, Y. F.; Zhu, X. G. Co-Precipitation Synthesis of Nanostructured Cu_3SbSe_4 and Its Sn-Doped Sample with High Thermoelectric Performance. *J. Chem. Soc. Dalton Trans.* **2014**, *43* (4), 1888–1896. https://doi.org/10.1039/c3dt52447g.

(39) Agocs, D. B.; Danna, T.; Prieto, A. L. Ambient Surface Stability of Thin Film Nanocrystalline Cu_3SbSe_4 and Structure-Property Relationships. *ACS Appl. Energy Mater.* **2019**, *2* (3), 1903–1910. https://doi.org/10.1021/acsaem.8b02019.

(40) Ramasamy, K.; Gupta, R. K.; Palchoudhury, S.; Ivanov, S.; Gupta, A. Layer-Structured Copper Antimony Chalcogenides ($CuSbSe_xS_{2-x}$): Stable Electrode Materials for Supercapacitors. *Chem. Mater.* **2015**, *27* (1), 379–386. https://doi.org/10.1021/cm5041166.

(41) Zhang, Y.; Li, L.; Li, D.; Wang, Q. Large-Scale Synthesis of Single Crystalline $CuSb(S_xSe_{1-x})_2$ Nanosheets with Tunable Composition. *J. Phys. Chem. C* **2015**, *119* (3), 1496–1499. https://doi.org/10.1021/jp5113747.

(42) Wu, Y.; Qiao, X.; Fan, X.; Zhang, X.; Cui, S.; Wan, J. Facile Synthesis of Monodisperse Cu_3SbSe_4 Nanoparticles and Thermoelectric Performance of Cu_3SbSe_4 Nanoparticle-Based Materials. *J. Nanoparticle Res.* **2015**, *17* (7), 285. https://doi.org/10.1007/s11051-015-3094-2.

(43) Skoug, E. J.; Morelli, D. T. Role of Lone-Pair Electrons in Producing Minimum Thermal Conductivity in Nitrogen-Group Chalcogenide Compounds. *Phys. Rev. Lett.* **2011**, *107* (23), 235901. https://doi.org/10.1103/PhysRevLett.107.235901.

(44) Ghanwat, V. B.; Mali, S. S.; Mane, R. M.; Patil, P. S.; Hong, C. K.; Bhosale, P. N. Thermoelectric Properties of Nanocrystalline Cu_3SbSe_4 Thin Films Deposited by a Self-Organized Arrested Precipitation Technique. *New J. Chem.* **2015**, *39* (7), 5661–5668. https://doi.org/10.1039/C5NJ00686D.

(45) Qiu, W.; Wu, L.; Ke, X.; Yang, J.; Zhang, W. Diverse Lattice Dynamics in Ternary Cu-Sb-Se Compounds. *Sci. Rep.* **2015**, *5* (1), 13643. https://doi.org/10.1038/srep13643.

(46) Kirkham, M.; Majsztrik, P.; Skoug, E.; Morelli, D.; Wang, H.; Porter, W. D.; Payzant, E. A.; Lara-Curzio, E. High-Temperature Order/Disorder Transition in the Thermoelectric Cu_3SbSe_3. *J. Mater. Res.* **2011**, *26* (15), 2001–2005. https://doi.org/10.1557/jmr.2011.43.

(47) Agocs, D. Hot Injection Synthesis and Characterization of Copper Antimony Selenide Non-Canonical Nanomaterials toward Earth-Abundant Renewable Energy Conversion, Colorado State University, 2018.

(48) Jain, A.; Ong, S. P.; Hautier, G.; Chen, W.; Richards, W. D.; Dacek, S.; Cholia, S.; Gunter, D.; Skinner, D.; Ceder, G.; Persson, K. A. Commentary: The Materials Project: A Materials Genome Approach to Accelerating Materials Innovation. *APL Mater.* **2013**, *1* (1). https://doi.org/10.1063/1.4812323.

(49) Hsiang, H. I.; Yang, C. T.; Tu, J. H. Characterization of $CuSbSe_2$ Crystallites Synthesized Using a Hot Injection Method. *RSC Adv.* **2016**, *6* (101), 99297–99305. https://doi.org/10.1039/c6ra20692a.

(50) Yarema, O.; Yarema, M.; Moser, A.; Enger, O.; Wood, V. Composition- And Size-Controlled I-V-VI Semiconductor Nanocrystals. *Chem. Mater.* **2020**, *32* (5), 2078–2085. https://doi.org/10.1021/acs.chemmater.9b05191.

(51) Balow, R. B.; Tomlinson, E. P.; Abu-Omar, M. M.; Boudouris, B. W.; Agrawal, R. Solution-Based Synthesis and Characterization of Earth Abundant $Cu_3(As,Sb)Se_4$ Nanocrystal Alloys: Towards Scalable Room-Temperature Thermoelectric Devices. *J. Mater. Chem. A* **2016**, *4* (6), 2198–2204. https://doi.org/10.1039/C5TA07546G.

(52) Liu, Y.; Yang, J.; Gu, E.; Cao, T.; Su, Z.; Jiang, L.; Yan, C.; Hao, X.; Liu, F.; Liu, Y. Colloidal Synthesis and Characterisation of Cu_3SbSe_3 Nanocrystals. *J. Mater. Chem. A* **2014**, *2* (18), 6363–6367. https://doi.org/10.1039/c4ta00085d.

(53) Kale, A. R.; Bullett, W. E.; Prieto, A. L. Controlling Phase Conversion of Cu-Sb-Se Nanoparticles through the Use of an Amide Base. *Nano Lett.* **2023**. https://doi.org/10.1021/acs.nanolett.3c00506.

CHAPTER II: A GUIDE FOR PERFORMING RIETVELD REFINEMENTS ON COMPLEX NANOSCALE SYSTEMS[1]

2.1 Introduction

Powder X-ray diffraction (PXRD) is one of the most common characterization techniques for nanocrystalline materials, used to identify the crystalline phases formed and often also used to estimate crystallite size.[1,2] However, pattern interpretation can become challenging when crystallite sizes are reduced to the nanoscale, especially as nanomaterials become increasingly complex.[2] Such complications are discussed thoroughly in an approachable editorial by Holder and Schaak: major factors include small crystallite sizes that lead to broadened peaks and non-spherical particles that can lead to differences in intensity and peak width,[1] both of which can make phase identification and deconvolution a challenge. Fitting diffraction patterns of nanomaterials can improve both of these, as well as allow for extraction of a wealth of additional structural and microstructural information.

Different techniques can be used to fit X-ray diffraction data, with the Rietveld method being the most common.[3] Although initially developed for fitting neutron diffraction data,[3] Rietveld refinements have become ubiquitous in solid state literature. In the Rietveld method, a theoretical line profile is constructed by refining various parameters of a crystal structure until the difference is minimized via a least-squares approach to the experimental pattern.[3,4] Rietveld refinements allow users to obtain a plethora of information relating to a sample's composition,

[1] This chapter is in preparation for submission to Chemistry of Materials as a methods paper. Amanda R. Kale carried out syntheses, characterization, method development, and manuscript preparation. Nathan Neisius assisted with method development and manuscript editing. Amy L. Prieto assisted with project administration and manuscript editing.

structure, and microstructure, and can be performed on multiple phases, which also allows for quantification of the present phases or determination of crystalline content.[3,4]

In the past few years, the application of Rietveld refinements for the XRD patterns of nanocrystalline products has become increasingly common, and has been used to report precise structural parameters,[5–8] show phase purity,[5,6,9–11] identify atomic composition,[8,9,12] allow for the deconvolution and quantification of multiple phases,[10,12,13] obtain microstructural parameters such as crystallite sizes and strain,[7,10,11] and model anisotropic particles.[10,14]

However, in nanomaterials, different structural factors can lead to similar artifacts in diffraction patterns, and as such, refinements need to be approached systematically.[2] With improvements in Rietveld software as well as pattern resolution, refinements of many bulk materials can be performed by refining all the parameters of interest at once, making it unnecessary in most cases to have a sequential refinement approach, and in such cases, comprehensive guides aimed at bulk materials exist.[4] To our knowledge, no comprehensive guide exits for performing refinements for nanostructured materials, making the technique inaccessible to non-experts and leads to refinements that are not physically meaningful. In this guide, we outline the main considerations for performing refinements on nanoscale systems, as well as our methodology, with case studies focused on anisotropic, multiphase nanoparticles, which can further complicate the refinement process.

2.2 Considerations for nanoscale refinements

2.2.1 Types of line profile fitting in the Rietveld method

Within the Rietveld method, there are different approaches to fitting the peak shapes, or peak profiles (also called the line profile in literature). The most commonly used are a Voigt or double-Voigt approach to Rietveld refinements and whole powder pattern modeling

(WPPM). Peak profiles resulting from sample microstructure are neither fully Gaussian or fully Lorentzian,[15] thus a convolution of the two, known as a Voigt function, is often used.[3,4] A Lorentzian function can describe the X-ray emission profile in addition to crystallite size and microstrain, while a Gaussian component is needed to account for factors that cause a normal distribution of measurements, such as thermal motion, as well as crystallite size and microstrain.[4] The Voigt approach requires the convolution of the Lorentzian and Gaussian functions on top of a previously determined instrument function. As this convolution can be computationally intensive, the Voigt approach can be approximated with a pseudo-Voigt approach. In the double-Voigt approach, Lorentizian and Gaussian convolutions used for both crystallite size and strain. In a size-strain round robin study, it was found that a double-Voigt approach was needed to accurately describe crystallite size.[15] In WPPM, this convolution approach is taken further by allowing additional line-profile components originating from the sample. While WPPM is a more comprehensive approach that can be used in single phase nanocrystalline systems, and can account for anisotropic peak broadening, we propose that the double-Voigt approach is a better choice when overlapping peaks are involved, such as is the case for anisotropic, multiphase systems, and is the technique we will be discussing in detail here. For a detailed discussion of WPPM, we refer the reader to works by Scardi et al.[1,7]

2.2.2 Factors affecting peak positions, peak profiles, and peak intensities

As mentioned above, performing refinements on nanoscale materials leads to additional challenges compared to bulk samples. In particular, the degree of information that can be extracted depends on the system, supporting data from alternate characterization methods, and the signal to noise ratio in the data itself. To make intentional choices about which parameters should be included in a fit, one must first understand how these parameters manifest in the diffraction

patterns. Here we discuss the various parameters involved in Rietveld refinements with an emphasis on common factors present in nanocrystalline samples. (We note that there more factors involved, but for simplicity, we have focused on the most common ones to consider). The different components involved in fitting diffraction patterns are peak positions, peak intensity, and peak/line profile, and the effects of each on the diffraction pattern are detailed below and in table 1.

Factors affecting peak positions: Lattice parameters and sample height. In nanostructured materials, compositions often vary more than the bulk, and can have higher concentrations of defects, which can affect lattice parameters as well.

Factors affecting intensity: atoms present in a given lattice plane. This includes atomic coordinates, atomic substitutions and defects/occupancy. Common in nanocrystalline materials, changes in atomic composition and defect concentrations have a substantial effect on peak intensity. The thermal vibrations of atoms result in atomic displacement, and thus effects on intensity are magnified in highly disordered materials. Preferential orientation (discussed in depth by Holder and Schaak) of particles can also cause certain lattice planes to be emphasized in the diffraction pattern more than would be expected for a randomly oriented sample,[2] which will be discussed more later.

Factors affecting peak profiles: primarily crystallite size (i) and other components of sample microstructure (ii).

i. The dominant factor affecting peak profiles is crystallite size.[3,4] Fewer of a specific lattice plane in a crystalline domain leads to less constructive interference and a greater distribution of interplanar distances, which results in broader peaks corresponding to that plane. The structure factor, the expected intensity from a given plane, remains the same and the area under the peak is conserved but broadened over a larger range of 2θ. When

crystallites are non-spherical, or anisotropic, peak widths change with the crystallite size in the direction of that lattice plane.

ii. Additionally, any factors that increase the distribution of interplanar distances in a sample, including microstrain as well as a distribution of crystallite sizes, will also lead to peak broadening. In nanocrystals, other common factors that can lead to a distribution of plane distances include variations in composition and defects. We note that both crystallite size and microstrain are major factors that can result in *anisotropic* peak broadening, which will be discussed in detail later.

Table 2.1. Sample-related factors and how they affect diffraction patterns.

	Peak Position	Peak Profile	Peak Intensity
General Factors			
Crystallite Size		Y	
Unit Cell Parameters	Y		
Atoms Present (in a given lattice plane)			Y High atomic disorder → greater deviations in peak intensities
Specific Factors Common to NC Systems			
Defects/ compositional deviation	Y If causes change in unit cell parameters	Y If induces microstrain	Y
Non-Spherical/ Anisotropic Particles		Y Anisotropic peak broadening	Y Preferential orientation, esp. if drop-cast
Distribution of Crystallite Sizes		Y (e.g. bimodal distributions can lead to super-Lorentizian peaks)	
Microstrain		Y	
Other factors that lead to a distribution of interplanar distances		Y	

2.3 Methodology

2.3.1 Considerations before refinements

Recommended additional characterization. A number of characterization techniques lend themselves well to complimenting X-ray diffraction patterns, and in some cases can also provide information to help inform refinements. We recommend that a secondary technique is used to assess both crystallite size and particle composition if possible.

- Crystallite size: electron microscopy
- Composition: electron diffraction, energy-dispersive X-ray spectroscopy, Raman, elemental analysis

Without access to other techniques, use of related literature can aid in assessing what parameters are expected for a given system and should be included in a refinement.

Sample Preparation. To decrease the effects of preferential orientation, which can complicate the identification of other factors affecting intensity, we recommend samples are dried, then ground with a mortar and pestle to ensure that aggregates are broken up. This makes samples more randomly oriented than when deposited from solution and more closely resembles what would be expected with bulk powder samples (reference patterns contain randomly oriented crystallites). Additionally, if quantification phase analysis will be attempted, there are additional considerations to make with the selection and preparation of a standard.[16]

Deconvoluting anisotropic peak broadening and preferred orientation. If working with anisotropic materials, it is crucial to understand the difference between anisotropic peak broadening and preferential orientation. Diffraction patterns obtained from samples dropcast from solution can be compared to those that are dried and ground to determine if preferential orientation results from the preparation method, which often suggests the presence of anisotropic particles. Electron microscopy can also complement XRD pattern fitting by supporting or disproving the

presence of non-spherical particles. Holder and Schaak discuss anisotropic peak broadening and preferential orientation in detail,[1] so we refer the reader to their tutorial for a detailed explanation with examples.

Instrument contribution. The instrument contribution is generally assessed by running a scan on a standard such as LaB_6. The instrument parameters are input into refinement software and additional convolutions are added to account for differences between the fit and the standard.3 A better fit for the instrumental contribution is important if the goal is to extract microstructural information from a sample.[3] To make this fit more precise, the scan of the standard should be obtained under the same conditions as sample scans are.[4] If working with small crystallite samples and/or low signal-to-noise ratios, background scans of the substrate with no sample should be taken to aid in distinguishing poorly crystalline particles from potential broad signal from the substrate. In extreme cases, additional corrections may be required, as described by Lipp et al. with ultrasmall particles in Benchtop XRD.[17]

Identify the majority crystalline phase and other phases. We recommend this is done in XRD processing software such as EVA (Bruker AXS), in which peaks are automatically identified and compared to patterns in a database. If there is a clear majority phase, begin by using only the one phase in refinements. If it appears to be a substantial mixture, allow both phases to be used. Upload .cif or .str files to refinement software.

2.3.2 Sequential approach to refinements

Freely refining too many parameters can lead to runaway fits that will have less physical meaning. Therefore, we recommend a sequential approach to Rietveld refinements, especially

when working in a new system (both when in the graphical user interface (GUI) and in input files), which is illustrated as a flowchart in figure 2.1.

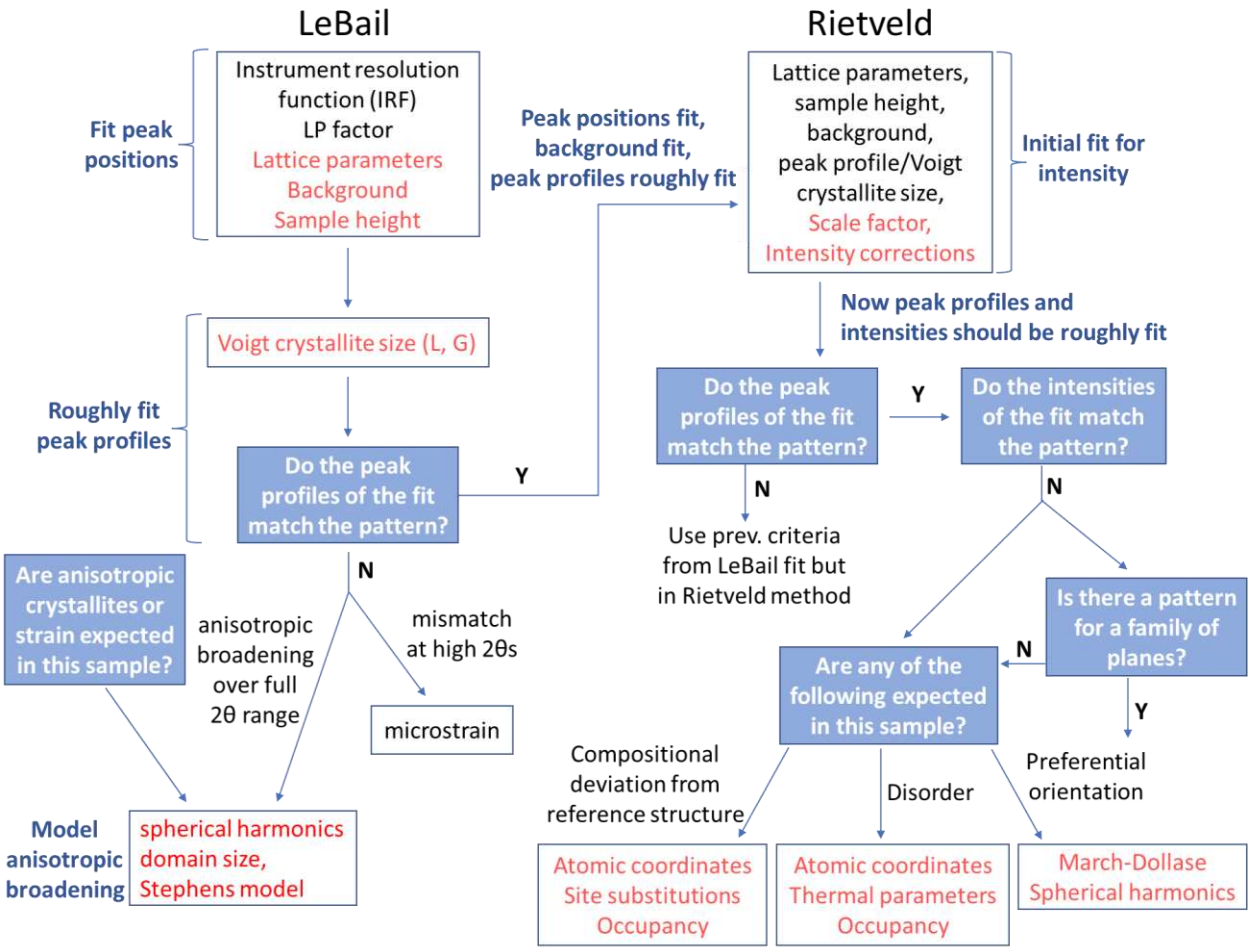

Figure 2.1. Flowchart of sequential approach to Rietveld refinements.

1. *Fit lattice parameters, corrections, and background.* As nanocrystalline systems can vary in composition more than in the bulk and have a greater variation in lattice parameters, we recommend the use of a LeBail fit first, which uses the unit cell symmetry to fit peak positions to obtain lattice parameters, without using atomic sites to generate intensities. Enable sample displacement correction for Bragg-Brentano geometry, as slight changes can substantially shift peak displacement. The goal is to start with a minimum number of background terms. If the background does not slope considerably, 3 background terms

should be sufficient to start. If you run a scan at low °2θ (below 25 °2θ), even with a knife blade, you will likely need 4-5 background terms (and maybe also 1/x correction). Including too many background terms, especially at the start of the refinement, can lead to accounting for a poorly crystalline phase with the background.

2. *Roughly fit intensities and peak profiles.* Copy lattice parameters and sample displacement correction from LeBail fit and fix them. This allows us to only investigate parameters that affect peak intensities and peak profiles. Refine scale and Lorentzian crystallite size. By roughly fitting intensities and peak profiles, it is easier to identify which additional parameters need to be accounted for to fit the diffraction pattern.
3. *Assess peak profiles; refine additional parameters*
    - If profiles are isotropic but peak shapes are still not a great match for the pattern, or intensities are too high at high 2thetas, add in additional convolutions for strain and/or crystallite size.
    - If peak profiles appear anisotropic, then you need to account for anisotropic broadening (either strain or crystallite size), which will be discussed in the case study.
4. *Assess peak intensities; refine additional parameters*
    - If peak intensities of the fit do not match the pattern, try refining atomic site position, thermal parameters, and/or atomic composition. We note that this is an iterative approach and suggest that the user only add 1-2 of the most likely additional parameters at a time, as many factors can affect peak intensity.
    - If intensities are still mismatched, or the refinement yields values that are unreasonable, fit preferential orientation.

- If any of the following are expected in your material due to information from additional characterization techniques or literature, refine the relevant parameters:
    - Material is expected to vary in composition from bulk/have defects: refine atomic position/ defects/ occupancy
    - Material is expected to be disordered: refine thermal parameters and account for defects/ occupancy
    - Material grows anisotropically: preferential orientation is likely, once anisotropic broadening is accounted for, refine preferential orientation with spherical harmonics, or March-Dollase if a specific plane for preferred orientation is expected.
- Minor phases: if you expect another phase might be present, proceed to step 5.

5. *Add in minor phases.* Begin by fixing the parameters for the major phase aside from the scale, then proceed to step 2. Now allow the parameters for the major phase to refine as steps 3 and 4 are performed.
6. Allow all parameters to refine. Once a satisfactory fit has been achieved, unfix all parameters and allow them to refine. This is important for obtaining accurate measures of error.

2.3.3 Common pitfalls

As multiple factors can result in similar artifacts in diffraction patterns, it is helpful to be aware of some common pitfalls when performing these refinements:

- *Setting all relevant parameters to freely refine from the start.* In the least squares minimization of the difference curve, Rietveld software may shift lattice parameters to

an unreasonable degree or fit actual peaks as background, and such effects are exacerbated in anisotropic systems.

- *Fitting with too many background terms.* With too many terms, broad peaks that are from the crystalline sample may be fit as background.
- *Using arbitrary preferential orientation to account for differences in peak intensities compared to the bulk.* Be sure to refine the relevant factors mentioned above.
- *In anisotropic samples, using only preferential orientation to increase the intensity of peaks of more crystalline phases.* If working with anisotropic materials, it is very important to understand the difference between anisotropic peak broadening and preferential orientation.

2.3.4 When is a refinement good enough to report?

A common problem in Rietveld refinements is refining random parameters (e.g. parameters that you have no reason to believe are in your sample) in order to minimize the various R values reported by the software as much as possible. We strongly discourage this practice as 1) many factors can lead to peak broadening, and the ones most likely to impact a particular system should be included, and 2) the different R values, agreement factors, weight different components differently.[4] R_p is the difference between the observed and actual profile. R_{wp} is the R_p weighted such that the fit of stronger reflections are not weighted more heavily than weaker ones and also includes experimental uncertainties. R_{exp}, expected R value, is the highest possible R that could be obtained given the counting statistics. The goodness of fit factor (GOF), χ, is a ratio between the R_{exp} and R_{wp}, with a value of 1-1.5 generally considered sufficient,[4] and is the best factor to use to compare between refinements, as the effect of different statistical conditions between measurements is minimized.

2.3.5 Modelling anisotropic peak broadening with the double-Voigt approach

As mentioned previously, anisotropic peak broadening primarily originates from anisotropic crystalline domains or anisotropic strain. In Topas, anisotropic strain can be modeled with the Stephens model from the GUI. However, in many nanoparticle systems, the anisotropy is primarily due to variation in the crystalline domain shape of the particle. For users working in Topas, we recommend modeling crystalline domain anisotropy through the use of a macro as published by Ectors et al.,[14,18,19] which are available in the SI of the work. This model requires the input of starting axes to describe how crystal growth is oriented with respect to a specific shape model. A follow-up publication of this work allows for the inclusion of a Gaussian convolution that also accounts for particle size distribution (for particles of the same shape), and also includes a spreadsheet for easier interpretation of the macro results.[18] A more recent publication mentions that the model can be used with the inclusion of isotropic strain,[19] which allows for a true double-Voigt approach.

2.4 Case study: modeling one anisotropic phase

The methodology above can be demonstrated with $CuSbSe_2$ nanosheets. PXRD was recorded on samples prepared with two different methods: one was drop-cast and another was deposited as a dried and ground powder (Figure 2.2). A substantial difference in certain peak intensities is seen between the two patterns, and the higher intensities for certain planes in the drop-cast sample correspond to the {001} family of planes. The {001} peaks are also broader, corresponding to a smaller crystallite size. This suggests that preferential orientation occurs substantially upon drop-casting, likely due to the presence of platelets or sheets that are thin in the [001]. With only two PXRD patterns, we can predict that these particles are anisotropic, and indeed this is confirmed with electron microscopy.[20] Prior to fitting any PXRD data, we know that

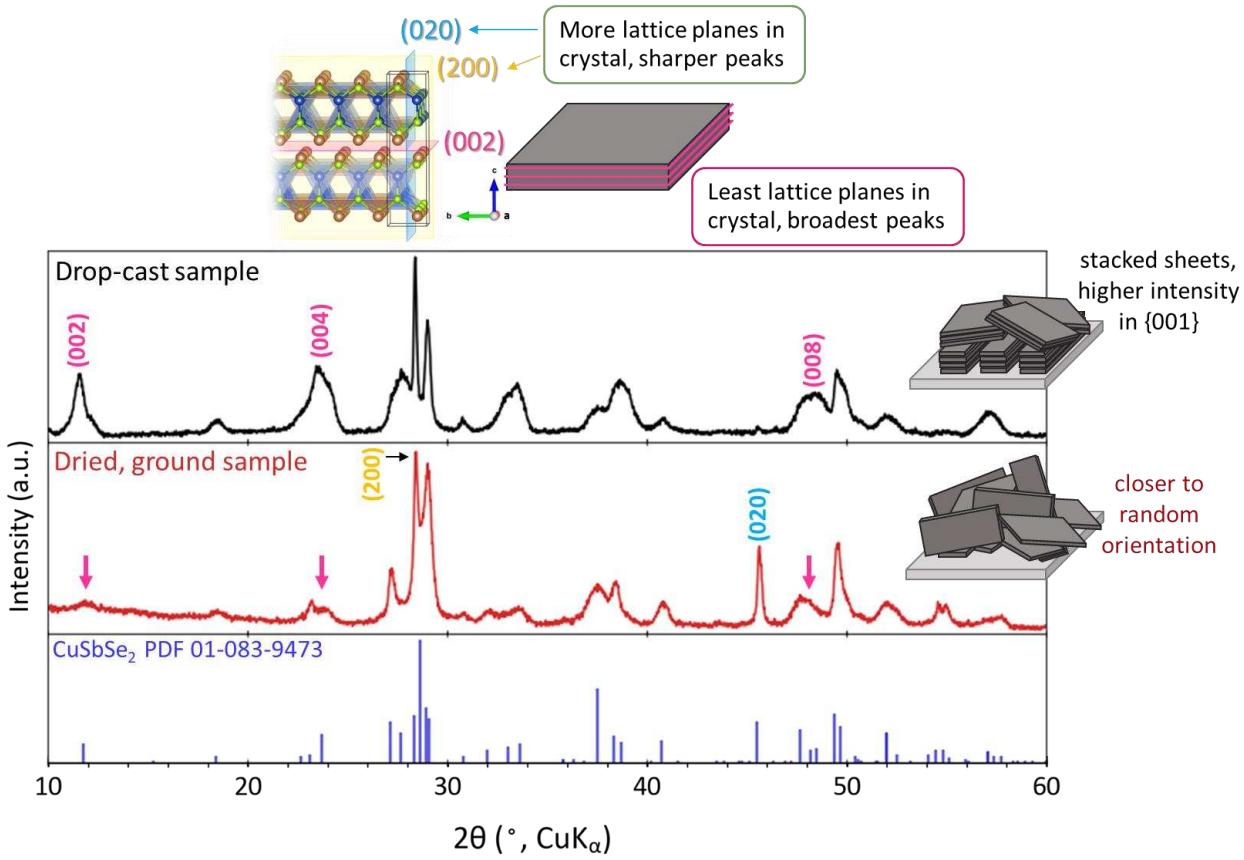

Figure 2.2 PXRD patterns of $CuSbSe_2$ nanosheets (A) drop-cast from a dispersion in hexanes and (B) deposited as a dried, ground sample.

anisotropic peak broadening is due to anisotropic crystalline domains, which helps to inform our refinement process. Because of the high degree of preferential orientation, we performed refinements on the dried, ground powder sample.

In figure 2.3a, we show the Rietveld refinement obtained on the ground sample once steps 1-2 have been performed, but without including an anisotropic model. Peak positions appear to be well-aligned, while peak profiles and peak intensities are not a good match. Initial instinct might be to fix intensity issues by adding in (200) preferential orientation, as in 2.3b. However, this will not fix issues with peak profiles, and does not provide physical meaning in the sample (the apparent increase in intensity may be due to a higher crystallinity in the [200], rather than substantial

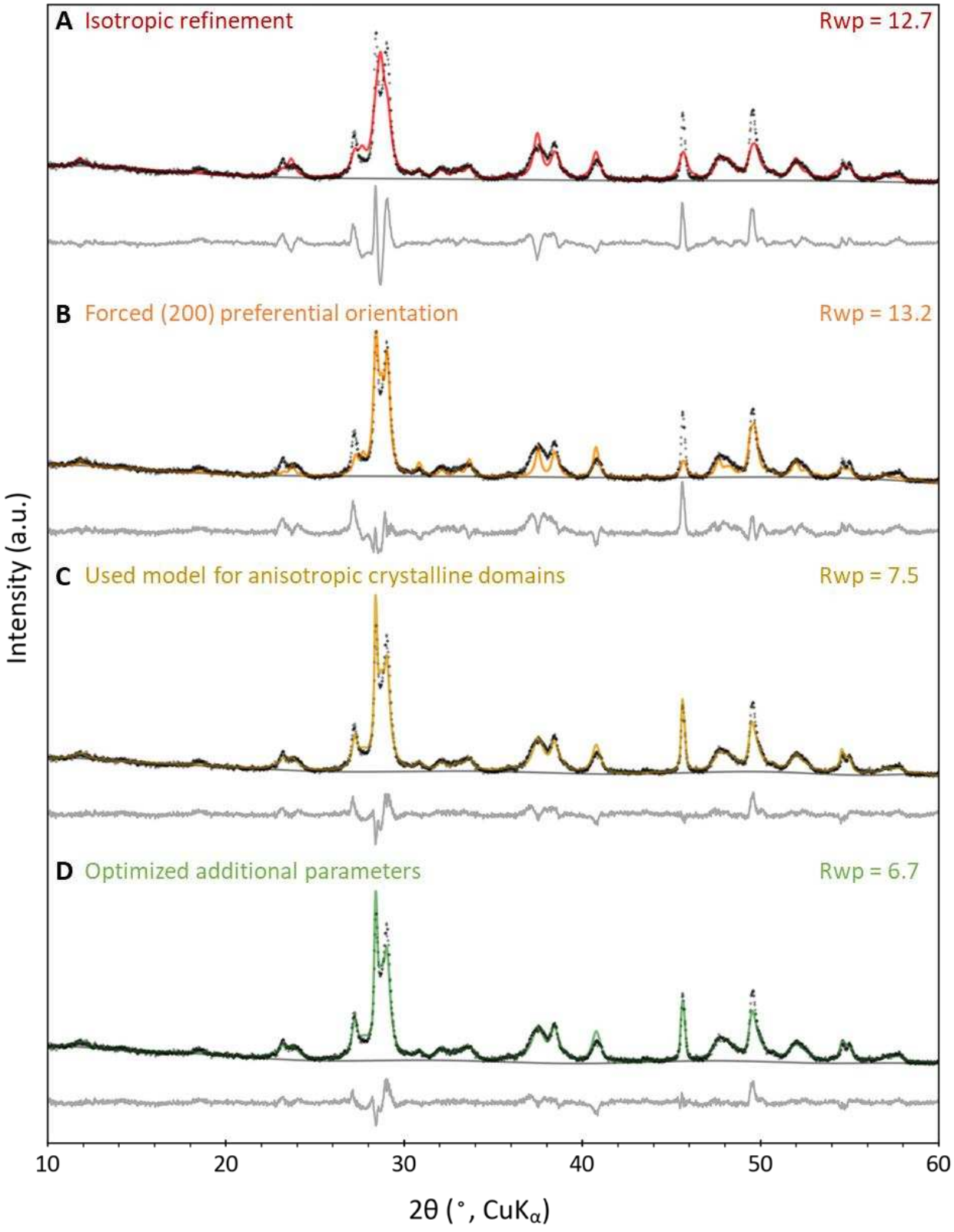

Figure 2.3. Diffraction pattern of $CuSbSe_2$ nanosheets with different Rietveld refinement parameters.

preferential orientation in the (200)). Instead, peak profiles should be fit more accurately first, as it is then easier to identify if intensity corrections need to be made. To account for the anisotropic peak broadening observed, the model by Ectors et al. was used.[14,18,19] We chose the cuboid model based on the sheets observed in electron microscopy. The anisotropic growth model requires an initial input or guess for the orientation of axes, and as electron microscopy supports that sheets grow thin in [001], we choose this as an initial vector. A perpendicular direction can be chosen from the fact that this crystal structure is orthorhombic. As we had access to electron diffraction, we knew that sheets grew long in the [020] and used this as our second axis.[20]

When this macro is used to model domain anisotropy as in figure 2.3c, we can see that nearly all intensity issues have been resolved, and the fit has greatly improved. Then we allowed additional parameters to refine, including site positions, occupancy, and atomic displacement/thermal parameters. If adding in preferential orientation at this point improves the fit, it should be included. We note that the same refinement process can be used on the drop-cast sample, in which preferential orientation will also have to be included. The orientation of crystalline domains obtained from the model match what we have observed in electron microscopy and with selected area electron diffraction.[20]

2.5 Case Study: modeling multiple anisotropic phases

Here we will show multiple fits for two different phases of anisotropic particles, and how different methods of fitting peak profiles leads to different weight percentages. Using reference patterns, we can identify that both Cu_3SbSe_3 and $CuSbSe_2$ are present. We already know from the analysis above that at least $CuSbSe_2$ will require anisotropic fitting; however, for purposes of exemplifying the importance of accurately fitting peak profiles, we will start with fitting each phase isotropically. Both phases appear to be present with decent intensity, so we include both in

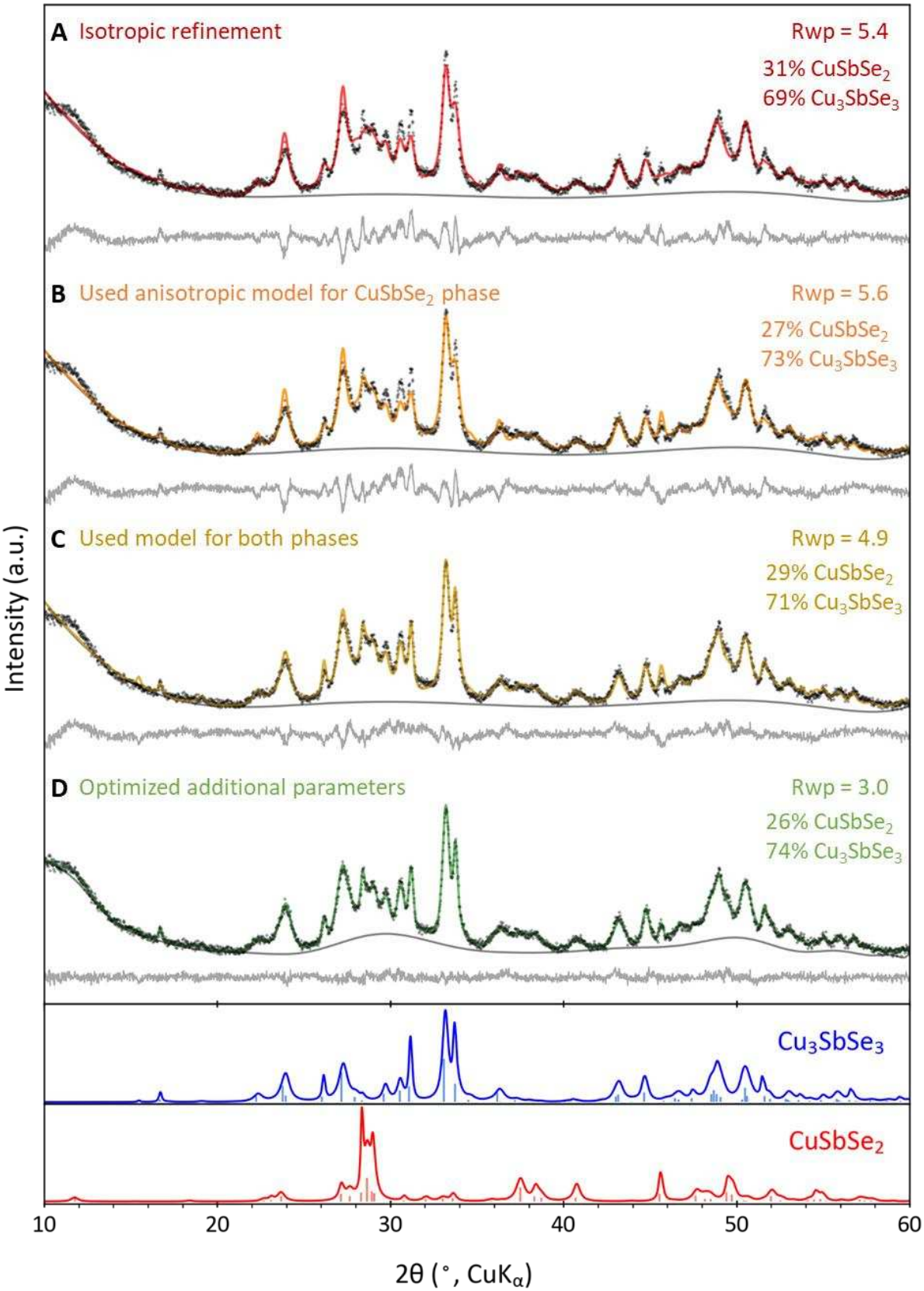

Figure 2.4: Rietveld refinements on a sample that is mixed with two anisotropic phases.

the initial fit, and performing steps 1 and 2 give the refinement in figure 2.4a. Based on previous information about $CuSbSe_2$, we can hypothesize that the same morphology is observed in this mixed phase pattern. Indeed, including the anisotropic fit for $CuSbSe_2$ gives a smaller R_{wp} value, indicating an improved fit. Electron microscopy shows that both particles grow anisotropically, and when an anisotropic crystallite is used for Cu_3SbSe_3 as well, the fit is even further improved (Figure 2.4c). Additional parameters can now be refined, and in addition to the ones mentioned above, the last fit in figure 2.4d includes the addition of more background terms, and this apparent background could be due to a very low crystallinity phase; however additional characterization techniques would be needed to support the presence of such a phase.

2.6 Limitations of the methodology proposed for Rietveld refinements

As mentioned previously, there are many factors that can affect peak broadening in particular, so it is possible to obtain a low R_{wp} or goodness of fit value and have a refinement that is not actually representative of the specimen. This is most likely to occur when peaks are extremely broad and/or signal to noise ratios are very low. It is still possible to obtain information on ultrasmall nanoparticles; however additional considerations need to be included.[17] In general we recommend looking at literature precedents and additional sample characterization to support information obtained from XRD models. In the case of anisotropic particles, electron microscopy is necessary to support the morphologies obtained by anisotropic modeling. By far the greatest drawback is that when working with multiphase, anisotropic refinements, it is necessary to have an informed guess on the orientation of crystal growth of at least one phase. While electron diffraction is a great method for this, by comparing XRD patterns drop-cast onto a diffraction plate vs ground as a powder and looking at the differences in preferential orientation observed, one can gain insight into a potential growth orientation. Although supplemental characterization

techniques are needed, this method provides a way to better fit anisotropic nanoparticles when multiple phases are present and to obtain information about anisotropic growth without access to a TEM.

2.7 Applications of the methodology proposed for Rietveld refinements

Despite the limitations above, we propose that the methodology outlined above can be used for a wide variety of nanoscale systems that include:

- *Phase identification and deconvolution.* As discussed above, various artifacts can cause nanocrystal diffraction patterns to vary considerably from bulk references, and as such, Rietveld refinements can support or disprove whether a given diffraction pattern results from that phase, and whether that phase alone can account for the diffraction pattern.
- *Phase quantification or percent crystallinity.* Weight percentages of phases can be determined in composite nanomaterials or mixtures of nanocrystals of different phases. The weight percent of crystalline material can also be obtained, though we note that distinguishing mass from amorphous content within a nanoparticle/ on the surface from ligand mass must be done with alternative characterization techniques.
- *Structural analysis.* Determining information such as lattice parameters can be particularly useful if aiming to describe how a material differs from the bulk or trying to quantify a solid solution substitution with Vegard's law.
- *Determining crystallite size and microstrain.* As long as a diffraction pattern is taken over a wide enough range of 2theta, the Rietveld method can distinguish between these two components. Being able to do this through Rietveld refinements is particularly useful for anisotropic samples.

- *Identification of atomic composition and defect concentration.* One can determine the occupancy for site substitutions, allowing for samples that vary considerably in composition from the bulk to be characterized.

In this guide, we provide a systematic, approachable framework for performing Rietveld refinements on the nanoscale. Artifacts of working on the nanoscale, such as small crystallite size, shape, and size distributions, as well as their propensity to deviate from bulk references in terms of unit cell parameters and composition, can complicate interpretation of diffraction patterns, and we propose that the use of Rietveld refinements can help with pattern interpretation. With the use of complimentary techniques to support data obtained from Rietveld refinements, we propose that this technique could be used more in the field to report microstructural information as well as detailed crystallite composition and accurate phase weight percentages. This guide will make nanoscale Rietveld refinements accessible to a non-expert, which we hope leads to an increase in the report of good quality refinements in the field.

References

(1) Holder, C. F.; Schaak, R. E. Tutorial on Powder X-Ray Diffraction for Characterizing Nanoscale Materials. *ACS Nano* **2019**, *13* (7), 7359–7365. https://doi.org/10.1021/acsnano.9b05157.

(2) Cervellino, A.; Frison, R.; Masciocchi, N.; Guagliardi, A. X-Ray Powder Diffraction Characterization of Nanomaterials. In *X-ray and Neutron Techniques for Nanomaterials Characterization*; Kumar, C. S. S. R., Ed.; Springer: Berlin, Heidelberg, 2016; pp 545–608. https://doi.org/10.1007/978-3-662-48606-1_10.

(3) Scardi, P. Diffraction Line Profiles in the Rietveld Method. *Cryst. Growth Des.* **2020**, *20* (10), 6903–6916. https://doi.org/10.1021/acs.cgd.0c00956.

(4) Dinnebier, R. E.; Leineweber, A.; Evans, J. S. O. Rietveld Refinement: Practical Powder Diffraction Pattern Analysis Using TOPAS. In *Rietveld Refinement*; De Gruyter, 2018. https://doi.org/10.1515/9783110461381.

(5) Safi, R.; Ghasemi, A.; Shoja-Razavi, R.; Ghasemi, E.; Sodaee, T. Rietveld Structure Refinement, Cations Distribution and Magnetic Features of $CoFe_2O_4$ Nanoparticles Synthesized by Co-Precipitation, Hydrothermal, and Combustion Methods. *Ceram. Int.* **2016**, *42* (5), 6375–6382. https://doi.org/10.1016/j.ceramint.2016.01.032.

(6) Lal, G.; Punia, K.; Dolia, S. N.; Alvi, P. A.; Dalela, S.; Kumar, S. Rietveld Refinement, Raman, Optical, Dielectric, Mössbauer and Magnetic Characterization of Superparamagnetic Fcc-CaFe2O4 Nanoparticles. *Ceram. Int.* **2019**, *45* (5), 5837–5847. https://doi.org/10.1016/j.ceramint.2018.12.050.

(7) Canchanya-Huaman, Y.; Mayta-Armas, A. F.; Pomalaya-Velasco, J.; Bendezú-Roca, Y.; Guerra, J. A.; Ramos-Guivar, J. A. Strain and Grain Size Determination of CeO_2 and TiO_2 Nanoparticles: Comparing Integral Breadth Methods versus Rietveld, μ-Raman, and TEM. *Nanomaterials* **2021**, *11* (9), 2311. https://doi.org/10.3390/nano11092311.

(8) Srinivas, Ch.; Deepty, M.; Kumar, E. R.; Prasad, S. A. V.; Tirupanyam, B. V.; Meena, S. S.; Prajapat, C. L.; Sastry, D. L. Rietveld Refinement and FTIR Spectroscopic Studies of Ni^{2+}-Substituted Zn-Ferrite Nanoparticles. *Appl. Phys. A* **2019**, *125* (8), 554. https://doi.org/10.1007/s00339-019-2840-1.

(9) Delekar, S. D.; Yadav, H. M.; Achary, S. N.; Meena, S. S.; Pawar, S. H. Structural Refinement and Photocatalytic Activity of Fe-Doped Anatase TiO_2 Nanoparticles. *Appl. Surf. Sci.* **2012**, *263*, 536–545. https://doi.org/10.1016/j.apsusc.2012.09.102.

(10) Ramos-Guivar, J. A.; Gonzalez-Gonzalez, J. C.; Litterst, F. J.; Passamani, E. C. Rietveld Refinement, μ-Raman, X-Ray Photoelectron, and Mössbauer Studies of Metal Oxide-Nanoparticles Growth on Multiwall Carbon Nanotubes and Graphene Oxide. *Cryst. Growth Des.* **2021**, *21* (4), 2128–2141. https://doi.org/10.1021/acs.cgd.0c01551.

(11) Henry, K.; Ahlburg, J. V.; Andersen, H. L.; Granados-Miralles, C.; Stingaciu, M.; Saura-Múzquiz, M.; Christensen, M. In-Depth Investigations of Size and Occupancies in Cobalt Ferrite Nanoparticles by Joint Rietveld Refinements of X-Ray and Neutron Powder Diffraction Data. *J. Appl. Crystallogr.* **2022**, *55* (5), 1336–1350. https://doi.org/10.1107/S1600576722008123.

(12) Singh, J.; Kumar, R.; Verma, V.; Kumar, R. Role of Ni^{2+} Substituent on the Structural, Optical and Magnetic Properties of Chromium Oxide ($Cr_{2-X}Ni_xO_3$) Nanoparticles. *Ceram. Int.* **2020**, *46* (15), 24071–24082. https://doi.org/10.1016/j.ceramint.2020.06.185.

(13) Anupama, A. V.; Keune, W.; Sahoo, B. Thermally Induced Phase Transformation in Multi-Phase Iron Oxide Nanoparticles on Vacuum Annealing. *J. Magn. Magn. Mater.* **2017**, *439*, 156–166. https://doi.org/10.1016/j.jmmm.2017.04.094.

(14) Ectors, D.; Goetz-Neunhoeffer, F.; Neubauer, J. A Generalized Geometric Approach to Anisotropic Peak Broadening Due to Domain Morphology. *J. Appl. Crystallogr.* **2015**, *48* (1), 189–194. https://doi.org/10.1107/S1600576714026557.

(15) Balzar, D.; Audebrand, N.; Daymond, M. R.; Fitch, A.; Hewat, A.; Langford, J. I.; Le Bail, A.; Louër, D.; Masson, O.; McCowan, C. N.; Popa, N. C.; Stephens, P. W.; Toby, B. H. Size–Strain Line-Broadening Analysis of the Ceria Round-Robin Sample. *J. Appl. Crystallogr.* **2004**, *37* (6), 911–924. https://doi.org/10.1107/S0021889804022551.

(16) Gualtieri, A. F.; Gatta, G. D.; Arletti, R.; Artioli, G.; Ballirano, P.; Cruciani, G.; Guagliardi, A.; Malferrari, D.; Masciocchi, N.; Scardi, P. Quantitative Phase Analysis Using the Rietveld Method: Towards a Procedure for Checking the Reliability and Quality of the Results. *Period. Mineral.* **2019**, *88* (2). https://doi.org/10.2451/2019PM870.

(17) Lipp, J.; Banerjee, R.; Patwary, Md. F.; Patra, N.; Dong, A.; Girgsdies, F.; Bare, S. R.; Regalbuto, J. R. Extension of Rietveld Refinement for Benchtop Powder XRD Analysis of Ultrasmall Supported Nanoparticles. *Chem. Mater.* **2022**, *34* (18), 8091–8111. https://doi.org/10.1021/acs.chemmater.2c00101.

(18) Ectors, D.; Goetz-Neunhoeffer, F.; Neubauer, J. Domain Size Anisotropy in the Double-Voigt Approach: An Extended Model. *J. Appl. Crystallogr.* **2015**, *48* (6), 1998–2001. https://doi.org/10.1107/S1600576715018488.

(19) Ectors, D.; Goetz-Neunhoeffer, F.; Neubauer, J. Routine (an)Isotropic Crystallite Size Analysis in the Double-Voigt Approximation Done Right? *Powder Diffr.* **2017**, *32* (S1), S27–S34. https://doi.org/10.1017/S0885715617000070.

(20) Kale, A. R.; Bullett, W. E.; Prieto, A. L. Controlling Phase Conversion of Cu-Sb-Se Nanoparticles through the Use of an Amide Base. *Nano Lett.* **2023**. https://doi.org/10.1021/acs.nanolett.3c00506.

CONTROLLING PHASE CONVERSION OF Cu-Sb-Se NANOPARTICLES THROUGH THE USE OF AN AMIDE BASE[1]

3.1 Overview

The family of copper antimony selenides is important for renewable energy applications. Several phases are accessible within narrow energy and compositional ranges, and tunability between phases is not well-established. Thus, this system provides a rich landscape to understand the phase transformations that occur in hot-injection nanoparticle syntheses. Rietveld refinements on X-ray diffraction patterns model anisotropic morphologies to obtain phase percentages. Reactions targeting the stoichiometry of $CuSbSe_2$ form Cu_3SbSe_3 before decomposing to thermodynamically stable $CuSbSe_2$ over time. An amide base was added to balance cation reactivity and directly form $CuSbSe_2$. Interestingly, Cu_3SbSe_3 remained present, but converts to $CuSbSe_2$ more rapidly. We propose that initial Cu_3SbSe_3 formation may be due to the selenium species not being reactive enough to balance the high reactivity of the copper complex. The unexpected effect of base on cation reactivity in this system provides insight into the advantages and limitations for its use in other multivalent systems.

3.2 Introduction

Copper antimony chalcogenides are of interest for photovoltaics[1,2] and thermoelectrics[3,4] due to their attractive optoelectronic properties and because they are composed of less toxic, more abundant elements. In the Cu-Sb-Se system, three ternary phases exist ($CuSbSe_2$, Cu_3SbSe_3, Cu_3SbSe_4) that have been shown to have similar stabilities in solution, making phase impurities a

[1] This chapter has been published in Nano Letters: https://doi.org/10.1021/acs.nanolett.3c00506. Amanda R. Kale carried out syntheses, reaction planning, characterization, and manuscript preparation, and William E. Bullett assisted with synthesis and characterization. Amy L. Prieto assisted with project administration and manuscript editing.

challenge in some syntheses.[5–7] While all three ternary nanoparticle phases have been synthesized in isolation[5,8,9], an understanding of the synthetic parameters that favor each ternary phase has not been demonstrated. Thus, the Cu-Sb-Se system is rich for the exploration of the effect of precursor reactivity on phase formation.

A common problem in multinary copper chalcogen syntheses is that one cationic precursor is often more reactive than the other, resulting in the formation of binary phases as 'sinks' or solid solutions rich in one cation.[10] One method to control precursor reactivity in these systems is through the addition of a reagent that favors the formation of more reactive cation complexes.[10] The base lithium bis(trimethylsilylamide) (LiHMDS) has been used to form reactive complexes in syntheses with trioctylphosphine (TOP)[11–13], where reactive metal silylamide intermediates form. LiHMDS has also been used in syntheses with oleylamine (OLA),[14,15] acting as a Brønsted base and deprotonating the oleylamine to form reactive oleylamide complexes in solution.[16,17]

While the understanding of precursor reactivity in nanoparticle synthesis has greatly increased in recent years, the development of unifying trends that can be used to design syntheses of new and unexplored systems remains a challenge in the field. If we can collectively define precursor reactivity with respect to the relative rate of atom-incorporation into the final product, then synthetic methods using similar precursors could be more readily applied to new materials. Here we define precursor reactivity in relation to the stability of the active complex that forms just prior to injection. A less stable active complex with easily dissociating leaving groups will be more likely to decompose and have its atom incorporate into a crystal structure, and we would call this precursor more reactive.

In this work, we aim to explore phase control in the Cu-Sb-Se system through the control of precursor reactivity. We show that metastable Cu_3SbSe_3 particles are generally formed first,

which then decompose into thermodynamically stable $CuSbSe_2$ sheets in reactions with oleylamine. We then attempted to alter precursor reactivity through the addition of LiHMDS in order to bypass the formation of the metastable phase and directly nucleate $CuSbSe_2$. In doing so, we test the applicability of LiHMDS to control reactivity in unexplored chalcogenide systems.

In the standard synthesis, $CuCl_2$ (0.5 mmol), $SbCl_3$ (0.5 mmol), and oleylamine (4 or 7 mL, OLA) were combined air-free in a flask and held at 90 °C for 30 min under N_2. In reactions with LiHMDS, 1 mmol was added to the flask containing the metal salts. The standard Se precursor was prepared by dissolving Se (1 mmol), in an alkahest solution of oleylamine and dodecanethiol.[18] The flask was heated to 150 °C and changed in color from blue to orange while heating. This color change has been observed in other Cu systems and is commonly cited as the conversion from Cu^{2+} to Cu^{+}.[19] Upon reaching 150 °C, the room-temperature Se precursor was injected, and particles were quenched into test tubes after the desired growth time. Powder X-ray diffraction (PXRD) patterns and subsequent Rietveld refinements were used to assess the nanocrystalline phases present and their relative quantities. Anisotropic particle morphologies were modeled for each phase using the method of Ectors et al. (additional details in SI).[20] Transmission and scanning electron microscopy (TEM, SEM) were used to image nanoparticles and assess morphology.

3.3 Results and discussion

To determine how the phase transformation pathway of Cu-Sb-Se ternary phases proceeded, we performed PXRD on the reaction products as time progressed. Despite a starting precursor ratio of 1:1:2 Cu:Sb:Se, PXRD patterns show that primarily crystalline Cu_3SbSe_3 is present at 2 min (Figure 3.1). The peaks denoted by *a* are $CuSbSe_2$, which increase in intensity over time as Cu_3SbSe_3 peaks corresponding to Cu_3SbSe_3 disappear. At 20 min, $CuSbSe_2$ dominates, with substantial preferential orientation observed in the {001} planes, *b*, due to nanosheet stacking.

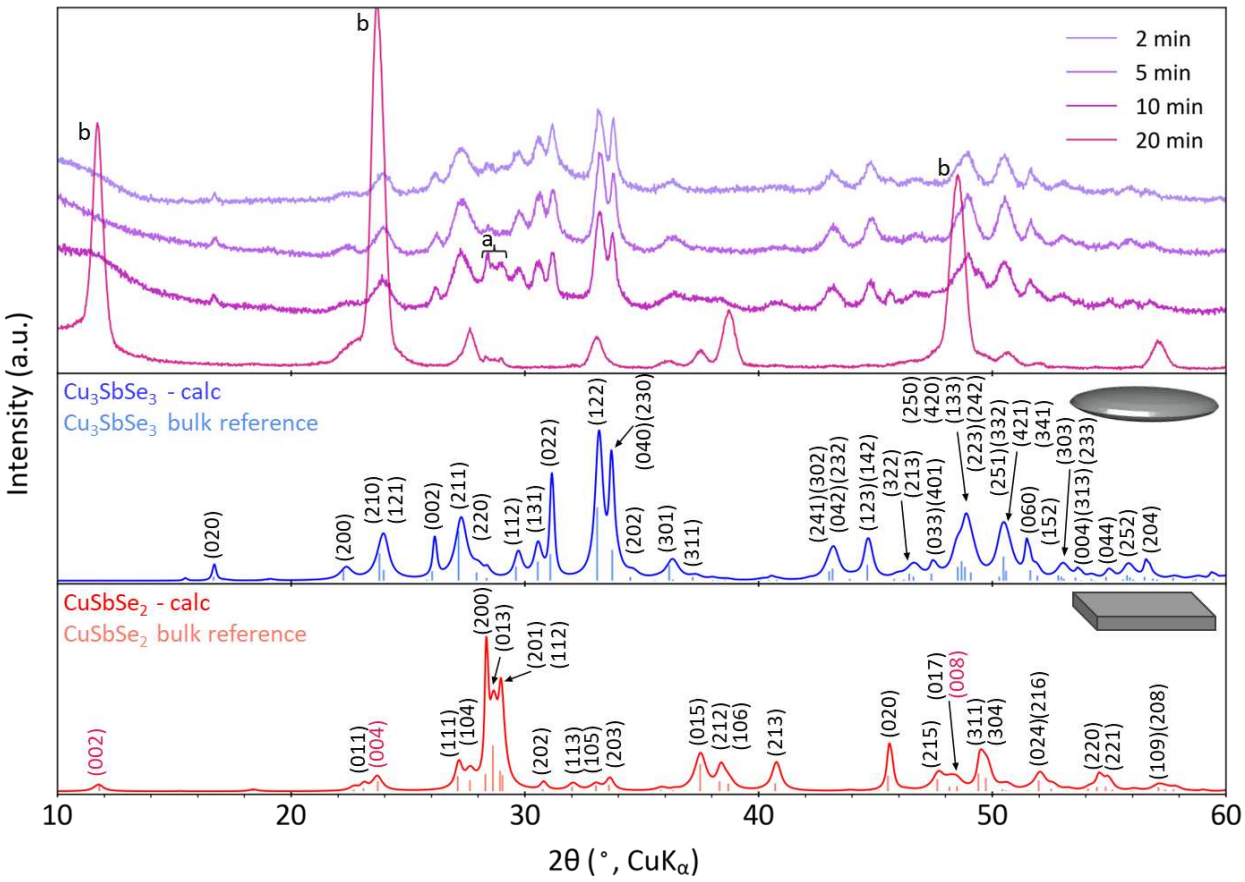

Figure 3.1. Powder X-ray diffraction patterns of 7 mL OLA, 2 mL injection syntheses. Calculated patterns of Cu_3SbSe_3 and $CuSbSe_2$ sheets of the approximate dimensions in PXRD patterns have been provided superimposed onto the bulk reference patterns.

TEM images and fast-Fourier transforms (FFT)s of lattice planes (FFTs) show particles with a variety of crystalline phases and morphologies (Figure 3.2, S3.1). At short times, 2 and 5 min, mostly small Cu_3SbSe_3 platelets are observed, along with small particles of low crystallinity (Figure 3.2A-H). In the 10 min aliquot, long, polycrystalline $CuSbSe_2$ ribbons are observed. As the reaction progresses to 20 min, larger, crystalline $CuSbSe_2$ sheets are observed that may have been formed from the coalescence of ribbons observed in the 10 min aliquot.

The anisotropic morphologies observed in TEM are consistent with patterns of anisotropic broadening observed in and modeled from PXRD patterns. This correlation is illustrated in figure 3.3. $CuSbSe_2$ sheet growth is limited in the [001], which has been attributed to van der Waals gaps

between the layers, caused by the Sb lone pairs.[4] Cu_3SbSe_3 platelet growth is limited in the [100], which is also consistent with growth inhibited by Sb lone pairs. It is possible that oleylamine binds strongly to these Sb sites, further discouraging growth.

We hypothesized that Cu-rich Cu_3SbSe_3 initially forms due to the active copper complex being more reactive than the active antimony complex. This difference in reactivity between

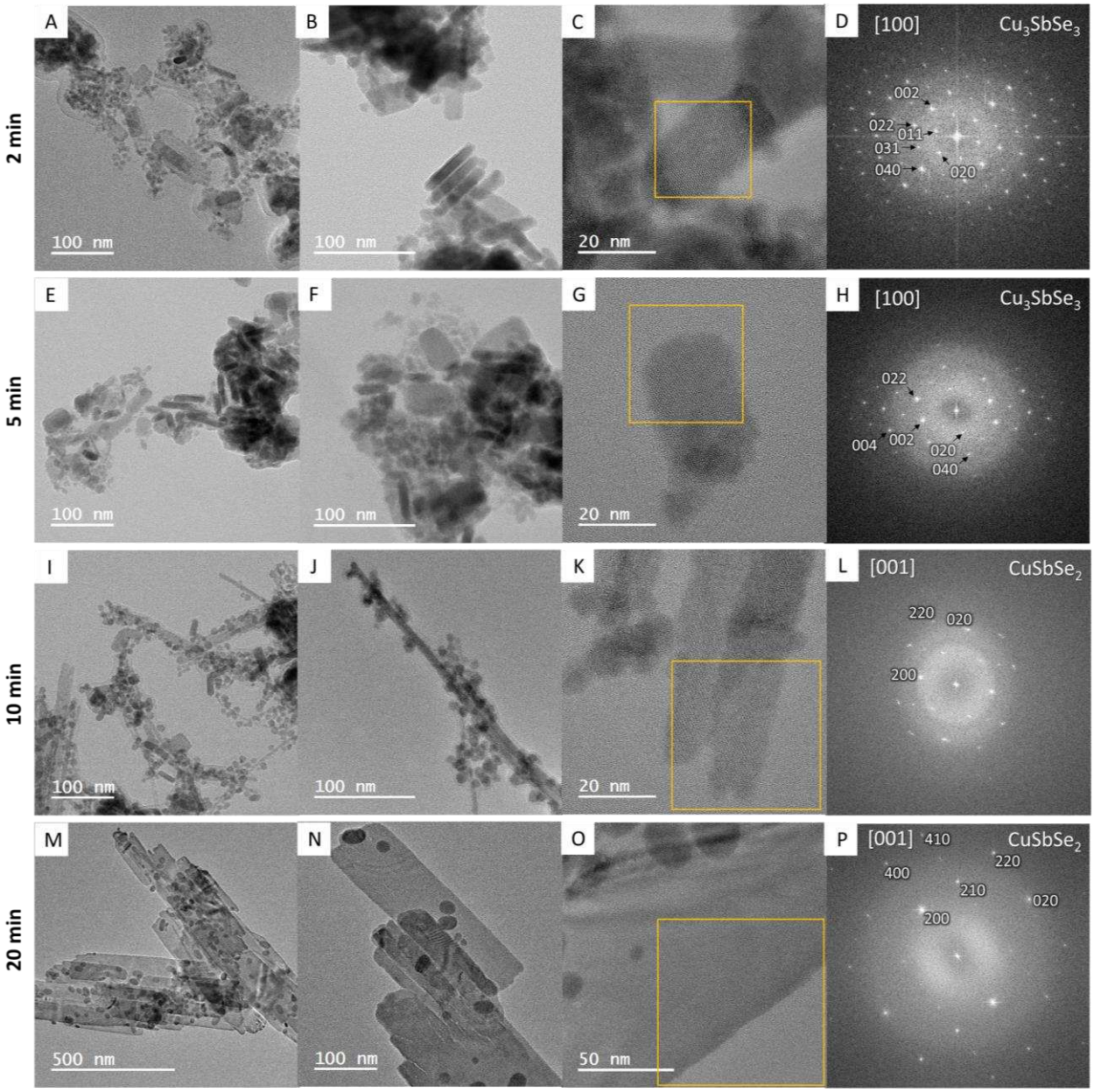

Figure 3.2. TEM images of 7 mL OLA syntheses of 2 (A-C), 5 min (E-G), 10 (I-L) and 20 min (M-P) aliquots. D,H,L, and P are FFTs of the image on the left.

cations has been explained with hard-soft acid-base theory.[21] As Sb^{3+} is a harder acid than Cu^{+} and oleylamine and chloride are hard bases, it is expected that hard-hard interaction of Sb^{3+} will lead to stronger bonds with available ligands, making its active coordination complex less likely to decompose to incorporate into a crystal structure. However, Cu^{+}, as a soft acid, is expected to form weaker bonds with the available ligands, making its complex less stable and more likely to incorporate into a crystal structure, favoring a Cu-rich phase.

The degradation of Cu_3SbSe_3 to $CuSbSe_2$ over time is supported by thermodynamic values. Of the three ternary phases, $CuSbSe_2$ has the most negative calculated H_f, -0.249 eV/atom, while Cu_3SbSe_3 has the most positive H_f, -0.175 eV/atom, and is the only ternary predicted to be unstable at its composition.[22,23] We propose that Cu_3SbSe_3 is a metastable phase that decomposes to the

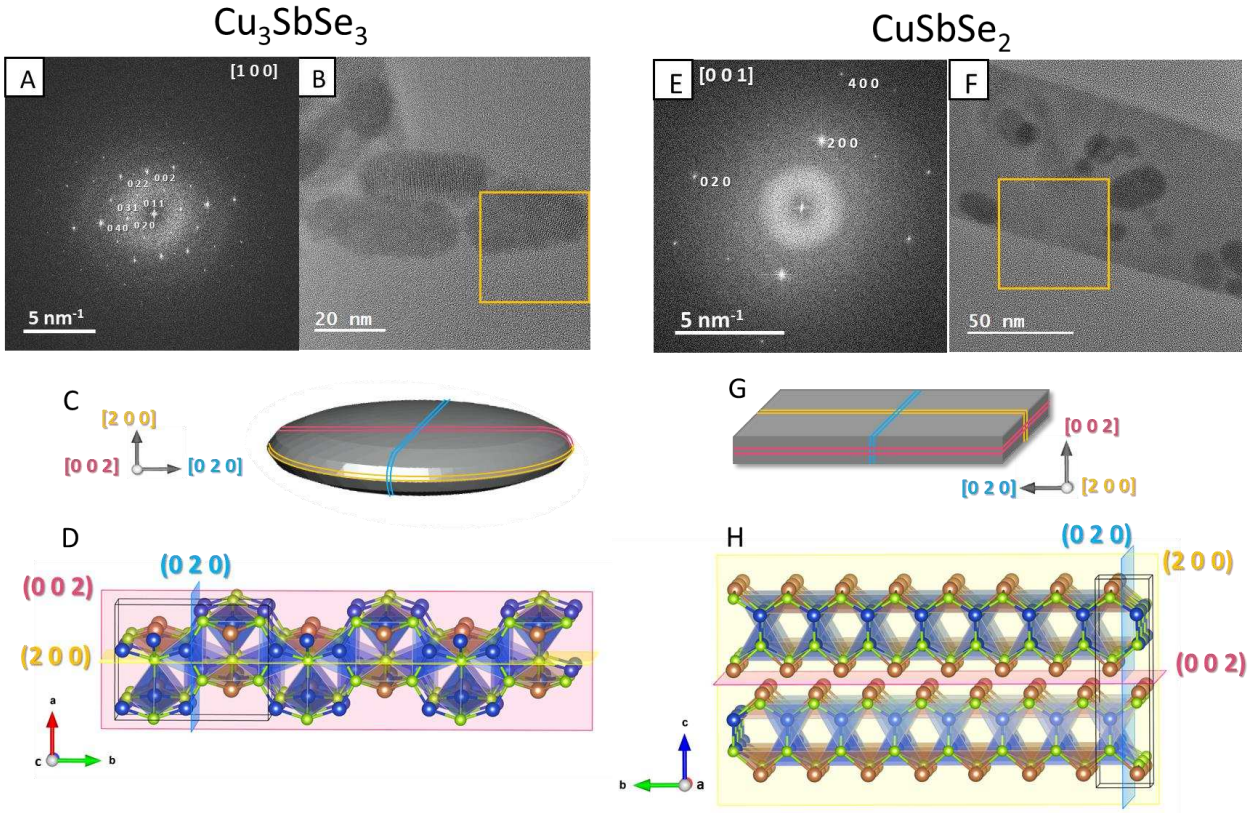

Figure 3.3. Structural characterization comparison of $CuSbSe_2$ (A-D) and Cu_3SbSe_3 (E-F). FFT and corresponding image of (A, B) Cu_3SbSe_3 and (E, F) $CuSbSe_2$.Anisotropic growth model showing the aspect ratio obtained from PXRD patterns for Cu_3SbSe_3 (C) and $CuSbSe_2$ (G). Crystal structure corresponding to anisotropic growth for (D) Cu_3SbSe_3 and (H) $CuSbSe_2$.

thermodynamically stable $CuSbSe_2$. To further test the metastable behavior, Cu_3SbSe_3 particles were isolated using an established phase-pure synthesis in similar solution conditions[24] and were heated in oleylamine or squalane. PXRD patterns of these products show that Cu_3SbSe_4 forms instead of the predicted $CuSbSe_2$ (Figure S3.2). The formation of Cu_3SbSe_4 impurities from Cu_3SbSe_3 particles has been observed in literature,[5] further supporting that the conversion landscape of Cu_3SbSe_3 particles is highly dependent on solution conditions. In particular, it appears that Cu and Sb species are required for $CuSbSe_2$ formation, as shown in equation 1. As many possible active complexes exist, those listed here are simply potential species. While it is possible that conversion could occur through Sb and Se diffusion into Cu_3SbSe_3, we do not see evidence of this in XRD or TEM and propose that Cu_3SbSe_3 decomposes back into Cu and Sb species prior to $CuSbSe_2$ formation.

$$Cu_3SbSe_3 + 2\ SbCl_3(RNH_2)_{3-x} + 3\ Se_8^{2-}(RNH_3^+)_y \rightarrow 3\ CuSbSe_2 + \text{oleylamine} + \text{byproducts} \quad (1)$$

One question that remains is why does Cu_3SbSe_3 form initially under these conditions instead of Cu_3SbSe_4, given that both are copper-rich phases? The compound Cu_3SbSe_3 is Se deficient compared to Cu_3SbSe_4, so its formation could be encouraged by slower incorporation of selenium. We performed the synthesis with a ratio of 3:1:4 Cu:Sb:Se to test whether Cu_3SbSe_3 would still form. Mostly Cu_3SbSe_4 is formed, though some Cu_3SbSe_3 is present at 5 min (Figure S3.3). We propose that some Cu_3SbSe_3 may form initially with both 1:1:2 and 3:1:4 ratios of Cu:Sb:Se either because the room-temperature Se precursor is not as reactive as the 150 °C cation complexes.

With the goal of bypassing the Cu_3SbSe_3 intermediate phase and directly nucleating the $CuSbSe_2$ phase that matches the starting stoichiometry, we used a silylamide-promoted approach,

which has been successful with other ternary Cu and Sb chalcogenide systems.[13,15] We aimed to test whether the addition of a silylamide base could be used to increase the reactivity of the harder acid Sb^{3+} in this system. We hypothesized that increasing the reactivity of the Sb complex would encourage Cu and Sb incorporation at similar rates and would allow us to directly nucleate $CuSbSe_2$.

Rietveld refinements were performed on XRD patterns to estimate the percent of crystalline phases in aliquots at each time from reactions with and without base (Figure 3.4, S3.4-3.6, Table S1). In most reactions, a majority of Cu_3SbSe_3 platelets are observed initially, which converted to larger $CuSbSe_2$ sheets over time. In the 4 mL OLA, 4 mL injection synthesis (Figure S3.7), almost entirely Cu_3SbSe_3 is formed initially both with and without base. The formation of mostly Cu_3SbSe_3 at short times when base is present disproves our initial hypothesis that the base would cause direct nucleation of $CuSbSe_2$. However, the addition of base does cause faster conversion from Cu_3SbSe_3 to $CuSbSe_2$. This is exaggerated in reactions with smaller volumes of OLA, which is likely due to the higher concentration of base. (Figure S3.6). This is also apparent in SEM images, as a greater proportion of large $CuSbSe_2$ sheets are present in the 5-minute LiHMDS sample than the one without base (Figure S3.8).

In previous work, our group characterized solutions of oleylamine with varying concentrations of LiHMDS and showed that substantial oleylamide formation is observed when the ratio of amine to LiHMDS is 14:1. In the reaction with 4 mL OLA, the ratio is ~12:1, and we propose that the higher ratio in the 4 mL reaction causes a greater formation of oleylamide species, increasing the reactivity of the cations more than in the 7mL synthesis. Although this ratio would decrease upon addition of the Se precursor, other work has shown that when a metal is present, the equilibrium between OLA and oleylamide is often pushed toward the amide products,[16] and thus we

propose that the formation of oleylamide species would be greater in the 4 mL synthesis. Additionally, the higher concentration of cations in the flask may make it more favorable for the unstable oleylamides to complex to the metal ions. We propose that the faster conversion to the $CuSbSe_2$ phase over time in the presence of base may be due to the decomposition of Sb-amide in solution *after* Cu_3SbSe_3 has already formed. Future characterization of these species would help to further elucidate reaction pathway.

Reactions were also performed with n-butylithium (n-BuLi), anticipating that the stronger base would produce higher concentrations of metal amide complexes, in turn encouraging more rapid formation of $CuSbSe_2$. Instead, a similar proportion of $CuSbSe_2$ was observed as when

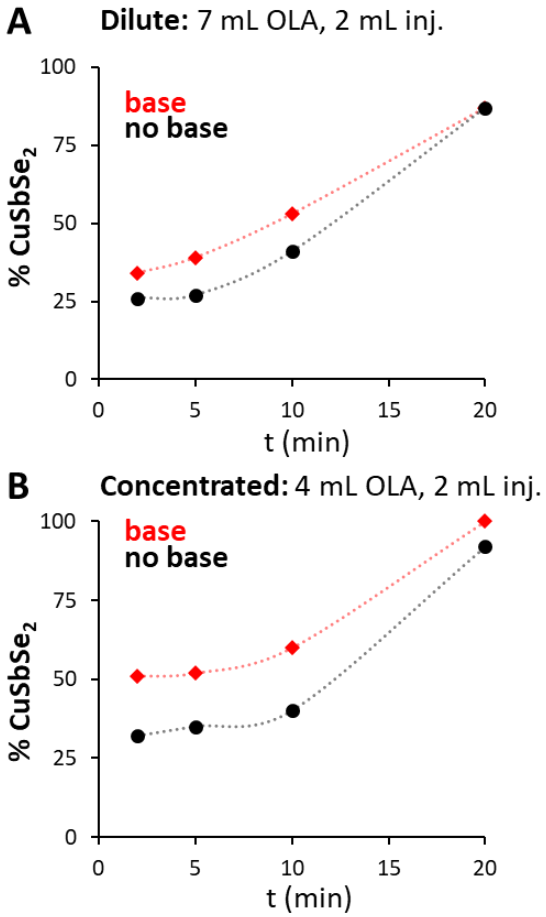

Figure 3.4. Transformation of crystalline phases present over time under various reaction conditions. Rietveld refinements were used to estimate mol percentages (Figures S3.4-3.6). Note that dotted lines are included to guide the reader's eye and do not represent fits of the data.

LiHMDS was added for the 7 mL reaction (Figure S3.9). We propose that a similar concentration of amide species must be present to obtain a similar proportion of Cu-rich and Cu-poor phases. Alternatively, it is possible that a lower concentration of Se available for incorporation may necessitate the initial formation of Cu_3SbSe_3. Only after the Se precursor is fully heated to reaction temperature will the effects of the added base be observed, resulting in an increase in the rate of conversion to the $CuSbSe_2$ phase.

The initial formation of Cu_3SbSe_3, even in the presence of base that should lead to the formation more reactive species, suggests that the copper complex remains too reactive for Cu^+ and Sb^{3+} to incorporate at similar rates. This is slightly surprising given that amide-promoted syntheses have been successful with Cu in literature. In a silylamide synthesis of Cu-In-Se nanoparticles, Yarema et al. were able to synthesize $CuInSe_2$ nanoparticles with the chloride salts in both OLA and TOP.[25] In more recent work, without the use of silylamide, O. Yarema et al. were able to synthesize $CuSbSe_2$ nanoparticles under conditions very similar to ours with the use of CuCl and obtained phase purity at temperatures above 120 °C.[8] One important distinction in both systems may be the use of CuCl instead of $CuCl_2$, as the reduction of Cu^{2+} to Cu^+ in our system may change the coordinating ligand, altering precursor reactivity. However, we synthesized particles with CuCl, instead of $CuCl_2$ under our reaction conditions, and the resulting products are nearly identical to those obtained with Cu^{2+} (Figure S3.10). Another key difference may be the preparation method of the Se precursor, as O. Yarema et al. prepared their Se precursor as a stock solution, which may result in a difference in Se solvation compared to ours.

This supports our hypothesis that the Se precursor may play a role in favoring the initial formation of Cu_3SbSe_3, as this phase is Se deficient compared to the other ternary phases. Some inconsistencies between reactions products observed when Se precursors were prepared with

different sonicators and/or stir-times caused us to question whether changes in the solvation of the Se precursor affects phase formation. To test this hypothesis, separate reactions were performed with stirring of the Se precursor for 15 and 40 min. The reaction with a longer Se precursor stir-time gave considerably more $CuSbSe_2$ at 5 min (Figure S3.11). Assuming that a longer stir time leads to greater dissolution of the Se precursor, we propose that the increased formation of $CuSbSe_2$ is due to an increased concentration of Se available for incorporation. It is possible that with an even better solvated Se precursor, the Cu_3SbSe_3 phase may be bypassed entirely, which would be consistent with its lack of observation by Yarema et al. Due to the dissolution of the Se precursor altering the rate of phase transformation, we kept its preparation consistent to measure the impact of the cations in solution.

The purpose of using amide-promoted syntheses is to make reactive complexes of both cations, making differences in hard-soft pairings obsolete. If the base is not used in high enough excess, this will not be the case, and the effects of the complexation with the original solvent will still be evident. Yarema et al. observed this in the synthesis of Ag-In-Se NPs: high concentrations of amide were required to observe incorporation of In and Ag in the final product that corresponded to initial ratios of In and Ag added.[12] This could explain why in our case it appears that the hard-soft acid-base mismatch for the Cu^+ complex may remain an issue. However, in our system, reactions using a higher amount of amide (3 mmol) appeared to result in the formation of Cu in the reaction flask, identified by its characteristic red color, and only Cu_3SbSe_3 was observed in PXRD (Figure S3.12). As the active Cu precursor was likely changed in these reactions, only smaller quantities of LiHMDS were used.

Another important distinction between literature syntheses that use LiHMDS and that herein is that amide bases are typically included in the injection solution, while ours is added to

the reaction flask. Adding LiHMDS to the previously used Se alkahest solution inhibited the dissolution of both solids. The replacement of the alkahest Se solution with a TOPSe precursor, commonly used with LiHMDS, resulted in the formation of only Sb^0 (Figure S3.13). We opted to then add the base to the reaction flask, which maintained the solubility of the Se precursor. An alternative approach that preserves the integrity of the Se precursor is to inject both Se and amide base separately. While a number of double-injection reactions were performed, separating the bases into different mediums, results appeared similar to reactions without base, likely due to the fact that the room-temperature base solutions took additional time to form metal oleylamide complexes when compared to the standard base reactions (Figure S3.14).

Additional double-injection reactions were performed by separating Sb and LiHMDS into a flask in OLA, with the goal of preforming Sb oleylamide complexes, and once dissolved, this solution and the Se precursor were injected into a flask containing $CuCl_2$ and OLA (Figure S3.15). The most Sb-deficient phase, Cu_3SbSe_4, was favored, with slightly more $CuSbSe_2$ present when base was added. The Sb species may have been even less reactive because the injected solution was at room temperature, directing initial phase formation to the most Sb-deficient. In a synthesis with the Sb-LiHMDS flask heated to reaction temperature prior to injection, Cu_3SbSe_3 is observed again instead of Cu_3SbSe_4, and more $CuSbSe_2$ is present in the reaction flask than with the room-temperature injection (Figure S3.16). This may point to, once again, Se being the directing factor for initial Cu_3SbSe_3 formation. In-depth studies with the Se precursor would need to be performed to determine if this is the case and is thus beyond the scope of this work.

3.4 Conclusions

In this work we have begun to decouple the variable rates of reactivity of the cations and anions, thereby developing a better understanding of phase control in the Cu-Sb-Se system. Under

our reaction conditions, metastable Cu_3SbSe_3 forms initially and decomposes to $CuSbSe_2$ over time. However, without any Sb or Se complexes in solution, Cu_3SbSe_3 decomposes to Cu_3SbSe_4, suggesting that monomers in solution are essential to $CuSbSe_2$ formation. We initially hypothesized that the addition of an amide base would encourage more rapid incorporation of Sb^{3+}, resulting in the direct nucleation of $CuSbSe_2$. However, mostly Cu_3SbSe_3 was still observed at short times. It does appear that degradation occurs more quickly with the addition of the silylamide. We hypothesize that this is due to the increased reactivity of the Sb monomer allowing faster formation of $CuSbSe_2$ *after* Cu_3SbSe_3 begins to decompose. Formation of the Sb amide may take longer than the formation of the Cu amide. Separate double-injections of base or Sb precursor and base were performed in an attempt to decouple variables, but even with heating, $CuSbSe_2$ could not be formed as the initial phase. It is possible that the selenium precursor is the variable that drives the initial formation of Cu_3SbSe_3. Understanding phase control in the Cu-Sb-Se system can be extrapolated to other multinary chalcogenide systems in which one cation tends to incorporate much faster than the other.

References

(1) Peccerillo, E.; Durose, K. Copper—Antimony and Copper—Bismuth Chalcogenides—Research Opportunities and Review for Solar Photovoltaics. *MRS Energy Sustain.* **2018**, *5* (1), 1–59. https://doi.org/10.1557/mre.2018.10.

(2) De Souza Lucas, F. W.; Zakutayev, A. Research Update: Emerging Chalcostibite Absorbers for Thin-Film Solar Cells. *APL Mater.* **2018**, *6* (8), 084501. https://doi.org/10.1063/1.5027862.

(3) Xie, D.; Zhang, B.; Zhang, A.; Chen, Y.; Yan, Y.; Yang, H.; Wang, G.; Wang, G.; Han, X.; Han, G.; Lu, X.; Zhou, X. High Thermoelectric Performance of Cu_3SbSe_4 Nanocrystals with $Cu_{2-x}Se$ in Situ Inclusions Synthesized by a Microwave-Assisted Solvothermal Method. *Nanoscale* **2018**, *10* (30), 14546–14553. https://doi.org/10.1039/C8NR03550D.

(4) Luo, Y.; Du, C.; Liang, Q.; Zheng, Y.; Zhu, B.; Hu, H.; Khor, K. A.; Xu, J.; Yan, Q.; Kanatzidis, M. G. Enhancement of Thermoelectric Performance in $CuSbSe_2$ Nanoplate-Based Pellets by Texture Engineering and Carrier Concentration Optimization. *Small* **2018**, *14* (50), 1803092. https://doi.org/10.1002/smll.201803092.

(5) Liu, Y.; Yang, J.; Gu, E.; Cao, T.; Su, Z.; Jiang, L.; Yan, C.; Hao, X.; Liu, F.; Liu, Y. Colloidal Synthesis and Characterisation of Cu_3SbSe_3 Nanocrystals. *J. Mater. Chem. A* **2014**, *2* (18), 6363–6367. https://doi.org/10.1039/c4ta00085d.

(6) Hsiang, H. I.; Yang, C. T.; Tu, J. H. Characterization of $CuSbSe_2$ Crystallites Synthesized Using a Hot Injection Method. *RSC Adv.* **2016**, *6* (101), 99297–99305. https://doi.org/10.1039/c6ra20692a.

(7) Agocs, D. B.; Danna, T.; Prieto, A. L. Ambient Surface Stability of Thin Film Nanocrystalline Cu_3SbSe_4 and Structure-Property Relationships. *ACS Appl. Energy Mater.* **2019**, *2* (3), 1903–1910. https://doi.org/10.1021/acsaem.8b02019.

(8) Yarema, O.; Yarema, M.; Moser, A.; Enger, O.; Wood, V. Composition- And Size-Controlled I-V-VI Semiconductor Nanocrystals. *Chem. Mater.* **2020**, *32* (5), 2078–2085. https://doi.org/10.1021/acs.chemmater.9b05191.

(9) Li, D.; Li, R.; Qin, X. Y.; Song, C. J.; Xin, H. X.; Wang, L.; Zhang, J.; Guo, G. L.; Zou, T. H.; Liu, Y. F.; Zhu, X. G. Co-Precipitation Synthesis of Nanostructured Cu_3SbSe_4 and Its Sn-Doped Sample with High Thermoelectric Performance. *J. Chem. Soc. Dalt. Trans.* **2014**, *43* (4), 1888–1896. https://doi.org/10.1039/c3dt52447g.

(10) Yarema, O.; Yarema, M.; Wood, V. Tuning the Composition of Multicomponent Semiconductor Nanocrystals: The Case of I–III–VI Materials. *Chem. Mater.* **2018**, *30* (5), 1446–1461. https://doi.org/10.1021/acs.chemmater.7b04710.

(11) Yarema, O.; Bozyigit, D.; Rousseau, I.; Nowack, L.; Yarema, M.; Heiss, W.; Wood, V.

Highly Luminescent, Size- and Shape-Tunable Copper Indium Selenide Based Colloidal Nanocrystals. *Chem. Mater.* **2013**, *25* (18), 3753–3757. https://doi.org/10.1021/cm402306q.

(12) Yarema, O.; Yarema, M.; Bozyigit, D.; Lin, W. M. M. M.; Wood, V. Independent Composition and Size Control for Highly Luminescent Indium-Rich Silver Indium Selenide Nanocrystals. *ACS Nano* **2015**, *9* (11), 11134–11142. https://doi.org/10.1021/acsnano.5b04636.

(13) Yarema, O.; Yarema, M.; Lin, W. M. M.; Wood, V. Cu-In-Te and Ag-In-Te Colloidal Nanocrystals with Tunable Composition and Size. *Chem. Commun.* **2016**, *52* (72), 10878–10881. https://doi.org/10.1039/c6cc05571k.

(14) Miller, R. C.; Neilson, J. R.; Prieto, A. L. Amide-Assisted Synthesis of Iron Germanium Sulfide (Fe_2GeS_4) Nanostars: The Effect of $LiN(SiMe_3)_2$ on Precursor Reactivity for Favoring Nanoparticle Nucleation or Growth. *J. Am. Chem. Soc.* **2020**, *142* (15), 7023–7035. https://doi.org/10.1021/jacs.0c00260.

(15) Moser, A.; Yarema, O.; Yarema, M.; Wood, V. Synthesis of Small Ag-Sb-Te Nanocrystals with Composition Control. *J. Mater. Chem. C* **2020**, *8* (45), 15985–15989. https://doi.org/10.1039/d0tc00880j.

(16) He, M.; Protesescu, L.; Caputo, R.; Krumeich, F.; Kovalenko, M. V. A General Synthesis Strategy for Monodisperse Metallic and Metalloid Nanoparticles (In, Ga, Bi, Sb, Zn, Cu, Sn, and Their Alloys) via in Situ Formed Metal Long-Chain Amides. *Chem. Mater.* **2015**, *27* (2), 635–647. https://doi.org/10.1021/cm5045144.

(17) Yarema, M.; Caputo, R.; Kovalenko, M. V. Precision Synthesis of Colloidal Inorganic Nanocrystals Using Metal and Metalloid Amides. *Nanoscale* **2013**, *5* (18), 8398–8410. https://doi.org/10.1039/c3nr02076b.

(18) Liu, Y.; Yao, D.; Shen, L.; Zhang, H.; Zhang, X.; Yang, B. Alkylthiol-Enabled Se Powder Dissolution in Oleylamine at Room Temperature for the Phosphine-Free Synthesis of Copper-Based Quaternary Selenide Nanocrystals. *J. Am. Chem. Soc.* **2012**, *134* (17), 7207–7210. https://doi.org/10.1021/ja300064t.

(19) Parvizian, M.; Duràn Balsa, A.; Pokratath, R.; Kalha, C.; Lee, S.; Van den Eynden, D.; Ibáñez, M.; Regoutz, A.; De Roo, J. The Chemistry of Cu3N and Cu3PdN Nanocrystals**. *Angew. Chemie - Int. Ed.* **2022**, e202207013. https://doi.org/10.1002/anie.202207013.

(20) Ectors, D.; Goetz-Neunhoeffer, F.; Neubauer, J. A Generalized Geometric Approach to Anisotropic Peak Broadening Due to Domain Morphology. *J. Appl. Crystallogr.* **2015**, *48* (1), 189–194. https://doi.org/10.1107/S1600576714026557.

(21) Coughlan, C.; Ibáñez, M.; Dobrozhan, O.; Singh, A.; Cabot, A.; Ryan, K. M. Compound Copper Chalcogenide Nanocrystals. *Chem. Rev.* **2017**, *117* (9), 5865–6109. https://doi.org/10.1021/acs.chemrev.6b00376.

(22) Jain, A.; Ong, S. P.; Hautier, G.; Chen, W.; Richards, W. D.; Dacek, S.; Cholia, S.; Gunter, D.; Skinner, D.; Ceder, G.; Persson, K. A. Commentary: The Materials Project: A Materials Genome Approach to Accelerating Materials Innovation. *APL Mater.* **2013**, *1* (1). https://doi.org/10.1063/1.4812323.

(23) Jain, A.; Hautier, G.; Ong, S. P.; Moore, C. J.; Fischer, C. C.; Persson, K. A.; Ceder, G. Formation Enthalpies by Mixing GGA and GGA + U Calculations. **2011**, *045115*, 1–10. https://doi.org/10.1103/PhysRevB.84.045115.

(24) Agocs, D. Hot Injection Synthesis and Characterization of Copper Antimony Selenide Non-Canonical Nanomaterials toward Earth-Abundant Renewable Energy Conversion, Colorado State University, 2018.

(25) Yarema, O.; Bozyigit, D.; Rousseau, I.; Nowack, L.; Yarema, M.; Heiss, W.; Wood, V. Highly Luminescent, Size- and Shape-Tunable Copper Indium Selenide Based Colloidal Nanocrystals. *Chem. Mater.* **2013**, *25* (18), 3753–3757. https://doi.org/10.1021/cm402306q.

CHAPTER IV: MORPHOLOGICAL CONTROL AND TWINNING IN $CuSbSe_2$

4.1 Introduction

The bottom-up fabrication of thermoelectric materials has increased in popularity due to the ease of controlling particle morphology and defects, which can later then be annealed into a film with desired defects and grain boundaries.[1,2] "Twin-engineering," describing the intentional inclusion of highly twinned powders or particles into materials,[3–5] is a way to increase photon scattering without drastically affecting electronic conductivity. Being able to synthetically control the degree of twinning in nanoparticle synthesis would allow us to control the type and number of defects, making a film prepared from this bottom-up approach highly tunable.

In previous work in our group, Miller et al. found synthetic conditions in which nearly all nanoparticles were twinned in a Fe_2GeS_4 synthesis.[6] This high degree of twinning was attributed to two main factors: 1) this olivine structure's lattice parameters, which allow for a pseudohexagonal lattice, in which $a \approx \sqrt{3}\, b$ and 2) formation of highly reactive monomers. The injection of the reagent LiHMDS, known to form reactive metal oleylamide complexes,[7] as well as the high reaction temperature (320 °C), meant that metal oleylamide intermediates would form and decompose rapidly.[8] It is proposed that the initial high supersaturation of active species makes the nucleation of defected seeds favorable, and that rapid growth onto such seeds prevents their decomposition.

The compound $CuSbSe_2$ has been tested as a thermoelectric material,[9–12] and the isostructural sulfur analogue has been reported to twin in literature.[13,14] However, to our knowledge, twinning has not been observed for the selenide analogue. As $CuSbSe_2$ has the same space group as Fe_2GeS_4, *Pnma*, though lacks a pseudohexagonal lattice, we investigated whether

twinning could be obtained in this system. Previously, we were able to control twinning in the Fe-Ge-S system simply through tuning concentration.[6] In the Cu-Sb-Se system, however, altering precursor concentration frequently results in the formation of impurities such as other stable ternary compounds on the phase diagram, or binary selenide impurities. Being able to induce or tune the degree of twinning in this system while retaining phase purity would show that we have gained control of the tunable parameters in this sensitive system.

4.2 Materials and methods

4.2.1 Reagents

Copper (II) chloride ($CuCl_2$, 97%, Ridel-deHaen), antimony chloride ($SbCl_3$, ≥99%, Aldrich), selenium powder (Se, 99.99%, STREM chemical), lithium bis(trimethylsilyl)amide (LiHMDS, 97%, Sigma Aldrich), ethanol (90%, Fisher Scientific), toluene (98%, Fisher Scientific) and hexanes (isomer mixture, Fisher Scientific) were used as received. Oleylamine (OLA, 70% technical grade, Sigma Aldrich) and hexadecane (HD, 99%, Sigma Aldrich), were heated to 80 °C and degassed under vacuum for 2 h, and 1-dodecanethiol (DDT, ≥98%, Sigma Aldrich) was sparged with N_2 for 2 h prior to use.

4.2.2 Synthesis of $CuSbSe_2$ nanosheets

This synthesis was adapted from Kale et al.[15] with a few modifications. Briefly, 0.5 mmol $CuCl_2$, 0.5 mmol $SbCl_3$, 6 mL oleylamine (or 3 mL OLA and 3 mL DDT), and 0-1 mmol LiHMDS were combined in a N_2 glovebox in a 25 mL 3-neck round bottom flask equipped with a condenser and thermocouple. The Se precursor, adapted from Liu et al.,[16] was prepared by combining 1 mL OLA, 1 mL DDT, and 1 mmol Se in a glovebox in a sealed vial. The metals flask was connected to a Schlenk line and heated under N_2 to 90 °C, then degassed under vacuum for 30 min. The flask was heated to 200 °C under N_2, and the Se precursor was injected. Growth was allowed for 2-60

min. Particles were washed with a standard solvent/antisolvent procedure with toluene and ethanol, followed by a final wash in hexanes.[15] Particles were stored dry or in hexanes in test tubes under ambient conditions.

4.2.3 Characterization

Powder X-ray diffraction (PXRD) was performed with a Bruker D8 Discover X-ray diffractometer using Cu Kα radiation (λ=1.54 Å). Particles dispersed in hexanes were drop-cast onto zero diffraction Si wafers. Scanning electron microscopy (SEM) images were taken with a JEOL JSM-6500F field emission scanning electron microscope at 15 keV. Samples were prepared for SEM by drop-casting particles dispersed in hexanes onto carbon-taped Al stubs. High-resolution transmission electron microscopy (TEM) images and selected area electron diffraction (SAED) were collected with a JEOL JEM-2100F TEM at 200 keV. Samples were prepared for TEM by drop-casting nanocrystal dispersions in hexanes onto Ni grids. Scanning TEM energy-dispersive X-ray spectroscopy (EDS) was carried out with an Oxford X-Max 80 mm^2 detector and analyzed using Aztec software. Image J was used to measure angles between sheets in TEM and SEM images. Digital micrograph was used to perform fast-Fourier transforms (FFTs) on TEM images to aid in crystallographic characterization.

4.3 Results and discussion

4.3.1 Temperature survey and development of OLA/DDT synthesis

In designing a synthesis to induce twinning in $CuSbSe_2$, we wanted to form reactive active species that would rapid nucleate and grow into $CuSbSe_2$, so we aimed to use a higher reaction temperature than in our previous 150 °C synthesis.[15] As we hypothesized that the formation of other phases would decrease the active species available for incorporation into the $CuSbSe_2$ crystal structure, we ran a series of reactions to determine optimum time and temperature for targeting a

synthesis of phase-pure $CuSbSe_2$ in oleylamine (Table 4.1). Unfortunately, while $CuSbSe_2$ is formed at shorter times at higher temperatures, Cu_3SbSe_3 is also observed, and Sb impurities appear at 200 °C. The reduction of Sb by OLA has been observed previously,[17–19] and we thus investigated alternative synthesis conditions to lower the concentration of OLA.

The reagent DDT was incorporated into the reaction flask, in hopes that less OLA present would decrease the reduction of Sb, and that the stronger coordination of DDT, as a soft base, to Cu (I), as a soft acid, would slow Cu incorporation just enough to nucleate favor initial nucleation of only $CuSbSe_2$ (rather than also Cu_3SbSe_3). One reaction was performed with a fast injection of Se precursor (~3 s) and the other with a slow injection (~7 s). Products were phase-pure by $CuSbSe_2$ by PXRD, though occasionally Cu_3SbSe_3 impurities were observed with TEM energy-dispersive X-ray spectroscopy. Reactions aliquots were taken at 5, 20, and 60 min. To assess potential twinning, SEM imaging was used to identify branched nanoparticle morphologies. SEM images show that the frequency of nanosheet branching greatly increased over time and is only easy to spot in 60 min samples (Figure 4.1). A greater population of branched nanosheets in observed in the slow injection reaction, although a few micron-sized branched agglomerates are observed at 60 min in the slow-injection reaction Our hypotheses for the why branching is observed at long times will be discussed in the growth pathway subsection.

Table 4.1. Phases identified with PXRD at each temperature from the synthesis with only OLA in the reaction flask.

Growth Time	150 °C	175 °C	200 °C
5 min	Cu_3SbSe_3	$CuSbSe_2$ Cu_3SbSe_3	$CuSbSe_2$ Cu_3SbSe_3 Sb
20 min	$CuSbSe_2$ Cu_3SbSe_3	$CuSbSe_2$ Cu_3SbSe_3	$CuSbSe_2$ Cu_3SbSe_3 Sb
60 min	$CuSbSe_2$	$CuSbSe_2$ Cu_3SbSe_3	No data

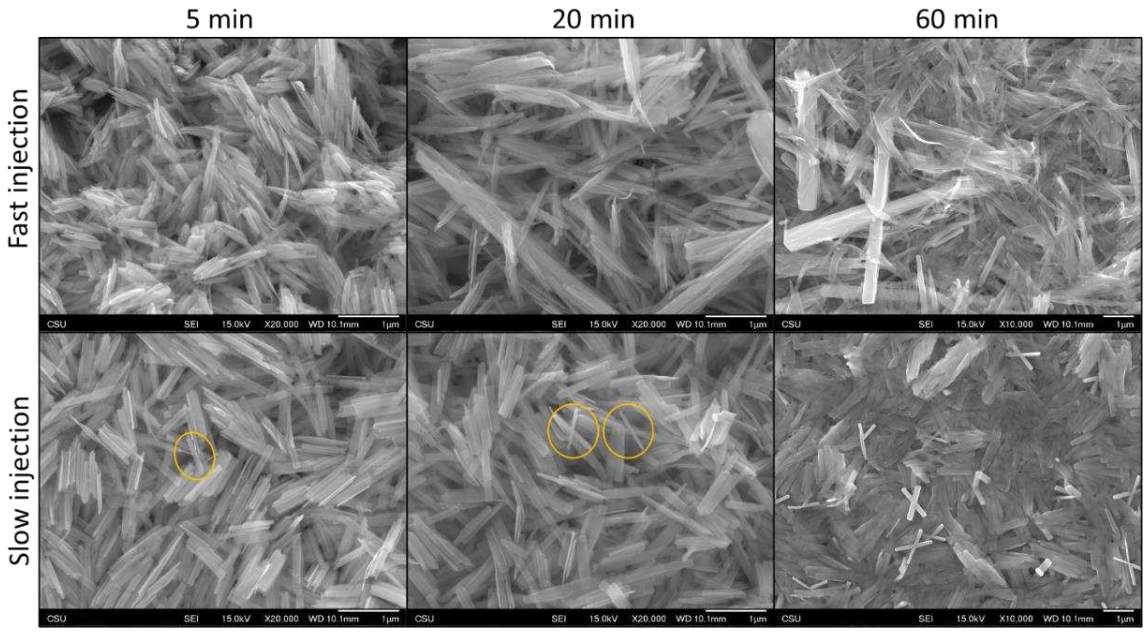

Figure 4.1. SEM images of $CuSbSe_2$ nanosheets in an oleylamine/dodecanethiol synthesis at 5, 20, and 60 min aliquots.

4.3.2 Characterization of growth in single $CuSbSe_2$ nanosheets at 200 °C

In order to hypothesize about directions of twin growth, we must know the crystallographic orientation of growth. We have previously characterized the growth of $CuSbSe_2$ nanosheets in our 150 °C synthesis in OLA, showing that growth is limited in [001], which we expect is due to the presence of Sb (III) lone pairs along this plane. Thus, growth is favored in the ab plane, with sheets growing longest in [020]. We observe the same growth pattern at 200 °C, for both the OLA only and combined OLA/DDT synthesis, and we show the selected area electron diffraction for nanosheets from the OLA/DDT synthesis (Figure 4.2). This growth pattern has been reported in literature in larger sheets in a 170°C synthesis in OLA and DDT.[9] The selected area electron diffraction (SAED) shows strongest diffraction from the $(01\bar{3})$, $(01\bar{5})$, and $(01\bar{7})$, though neither diffraction from {002} or {020} is observed. This is due to the nanosheet being slightly tilted away from the [200] zone axis.

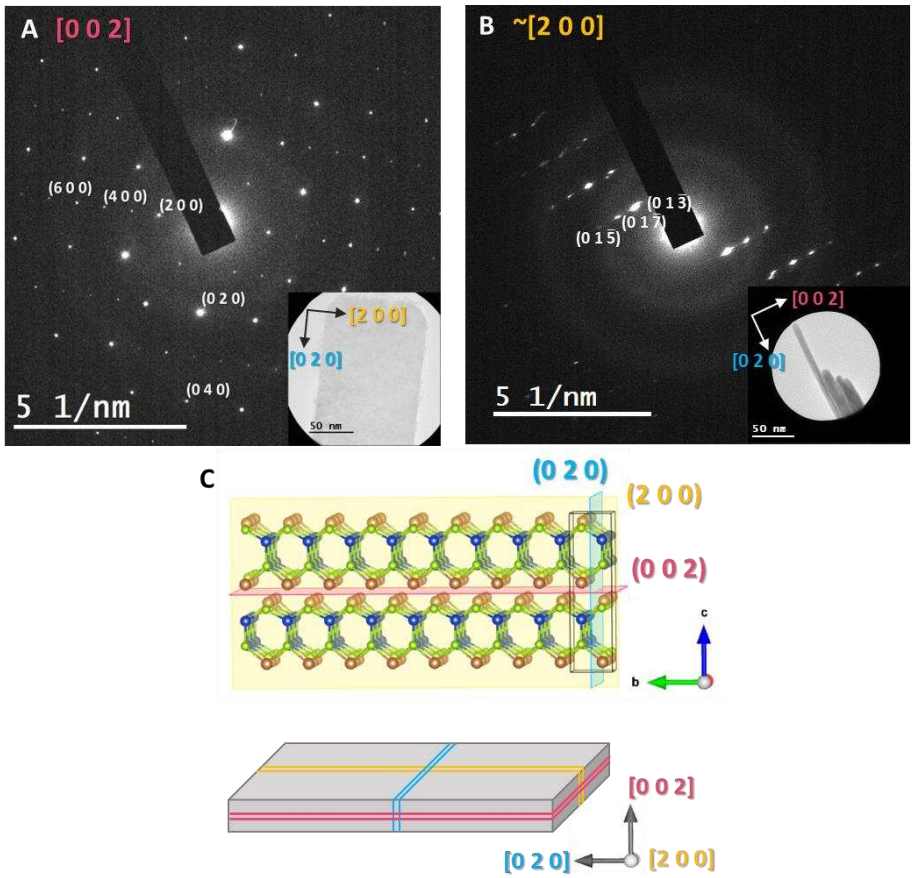

Figure 4.2. Selected area electron diffraction of single nanosheets from the 5 min OLA/DDT synthesis, showing (A) a nanosheet face and (B) nanosheets on their sides. (C) Crystal structure of $CuSbSe_2$ with growth longest in [020].

4.3.3 Assessment of nanosheet branching in OLA/DDT synthesis

Under these conditions, branched nanosheets have either one or two branches off a main sheet, and all occur consistently at ~60° angles as shown in Figure 4.3. As these ~60° angles cannot be accounted for by symmetry elements in the orthorhombic space group, it is highly unlikely that nanosheets are single crystals, so we propose that nanosheets are likely twinned. We initially hypothesized twinning was occurring in the (104), as this would be consistent with twinning reported for chalcostibite in literature and the ~60° angles observed, as long as some sheets grew long in [002] (Figure 4.4). If this were the case, SAED of branched particles lying flat should be

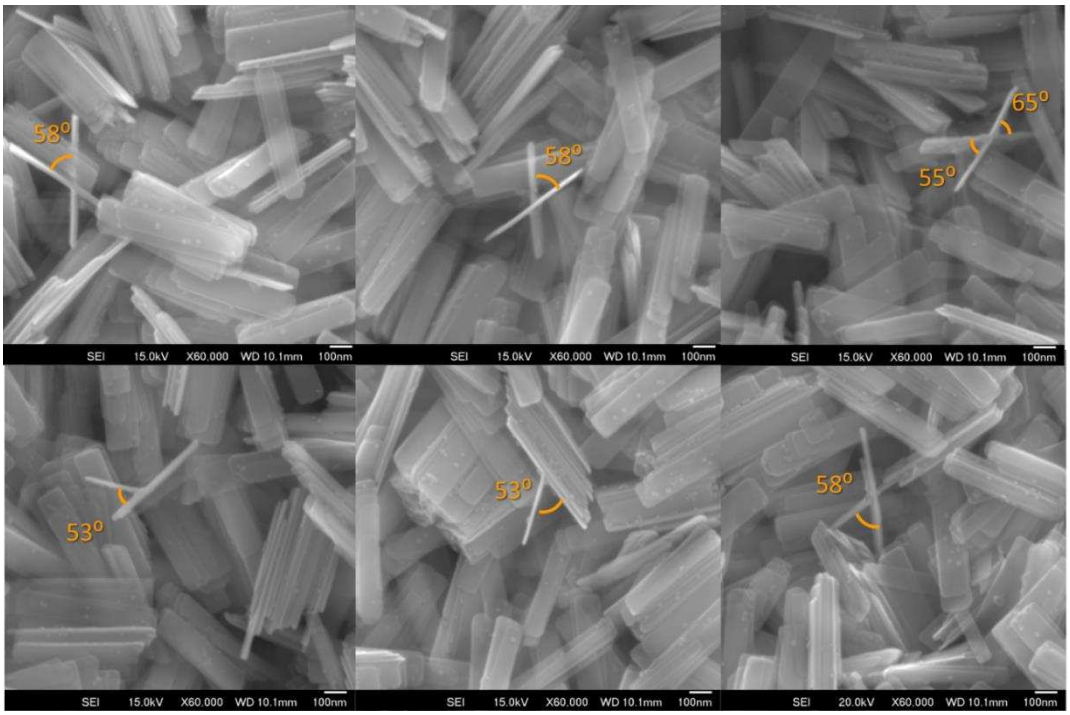

Figure 4.3. Representative SEM images of branched nanosheets from a 5 min OLA/DDT synthesis, showing that nanosheet branching occurs at 53-65° angles.

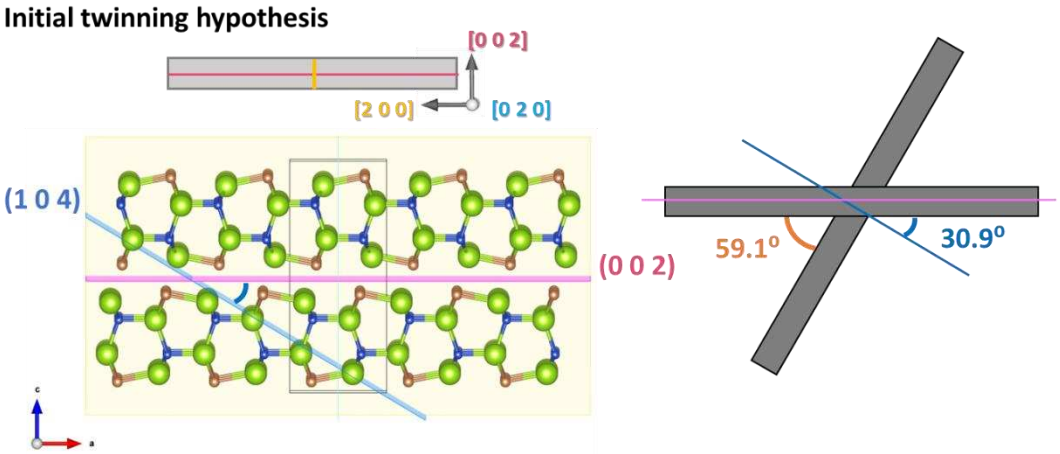

Figure 4.4. Crystal structure of a nanosheet if growth occurred longest in [200] and proposed twinning resulting from reflection or rotation from (104).

oriented on the [020] zone axis. However, the collection of additional SAED data does not show any single sheets growing long in the [200]. Additionally, SAED collected on branched particles show patterns that are consistent with the single sheets oriented on the [200] zone axis (Figure 4.5). This disproves our hypothesis of twinning occurring from the (104), in which case SAED

would have been observed in the [020] zone axis. Although the twinning reported in literature is for the sulfide, which has smaller unit cell parameters, the ratios between the a, b, and c parameters are very similar to the selenide, so the occurrence of twinning on a different plane is unexpected. Unfortunately, few particles with single nanosheet branches (not agglomerates of multiple sheets), were observed in 60 min sample, complicating SAED patterns, and at short times, branched particles were too few to reliably find in TEM. Both factors limit both the ability to obtain quality diffraction patterns and branch angle measurements at sufficient quantities. Thus, we aimed to alter the synthesis to form branched nanosheets at shorter times, before larger agglomerates of plates formed.

Our initial attempt to favor twinning at shorter times was to double the concentration of metal salts and Se, as Miller et al. was able to alter the degree of twinning through changing concentration.[6] However, even less particle branching was observed, as well as phase impurities.

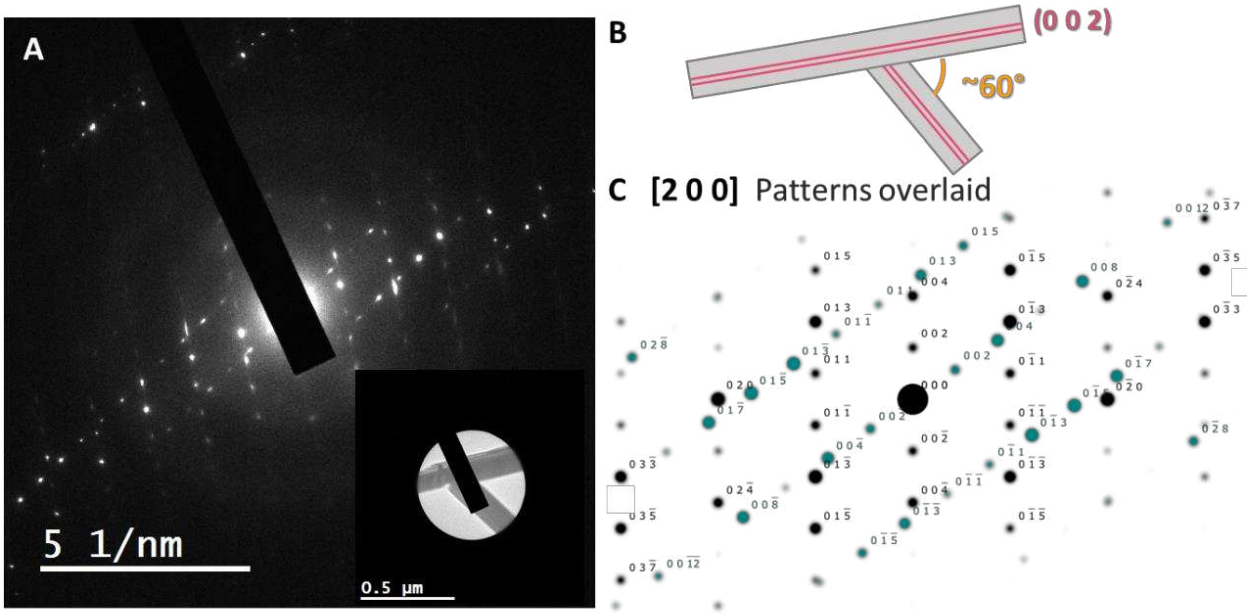

Figure 4.5. (A) SAED corresponding to a branched nanosheet from OLA/DDT synthesis with reference image as inset. (B) Schematic showing the orientation of branched nanosheets highlighting the (002) plane. (C) Two simulated electron diffraction patterns in the [200] overlaid at a 55.2° angle, with slight offset from the zone axis to match the diffraction pattern.

As our concentration is higher to begin with than when Miller et al. observed the highest degrees of twinning, we propose that there might be a "sweet spot" of precursor concentration, above which no additional benefits of twinning are observed. Thus, we aimed to increase precursor reactivity, such that monomers would react rapidly.

4.3.4 Amide-promoted twinning in OLA synthesis

We aimed to increase precursor reactivity by mimicking the synthesis conditions of Miller et al. and adding the silylamide base, LiHMDS, to form reactive metal oleylamide complexes. Operating off their hypothesis, we hoped that increasing the metal complex reactivity would create a supersaturation of monomers, favoring the formation of twin defects. As no branched sheets were observed in the standard 150 °C syntheses, we hypothesized that higher temperatures are necessary to have a supersaturation of active species and thus rapid initial nucleation, and pursued a 200 °C synthesis, despite the Sb reduction that occurs at that temperature. Upon the addition of LiHMDS to the reaction, a considerable increase in nanosheet branching is observed (Figure 4.6). As branched sheets are mostly single sheets (not agglomerates), it is easier to perform SAED, and the

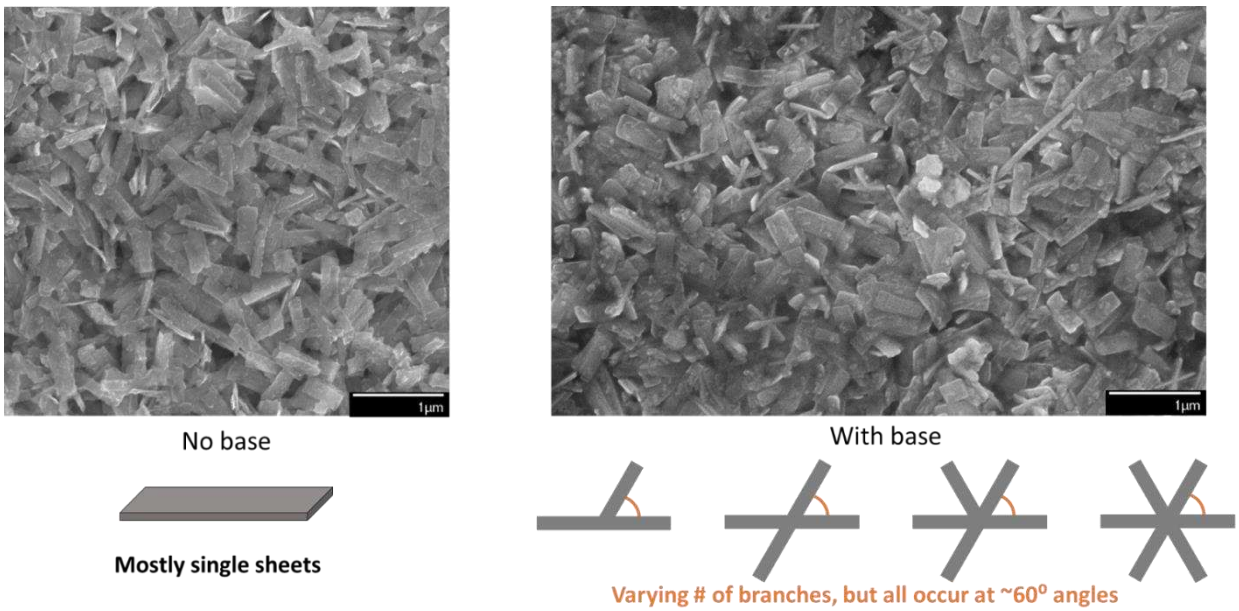

Figure 4.6. SEM images of nanosheets (A) without base and (B) with base.

same diffraction pattern is observed for these branched sheets, in the [020] zone axis, as those in the OLA/DDT synthesis. Interestingly, under these synthesis conditions, the number of branches vary, up to 4 additional branches to a single sheet, and still appear to occur at ~60° angles. Diffraction patterns of branched particles are comparable to those from the OLA/DDT synthesis. The presence of the same growth pattern in two different syntheses leads us to believe that twinning is occurring and does so off the same plane in both cases.

With the greater number of branched particles in the amide synthesis, we were able to obtain a clearer picture of twinning in the system. As we can measure with a higher degree of accuracy in TEM than SEM, and particle rotation is minimized, we were able to determine that branches occur off a nanosheet at 55.2±1.2° for 50 branches. In sheets with more than 4 branches, the angle between one set of branches is higher, as shown in figure 4.7, which caused us to initially approximate a larger angle of ~60°. The boundary between nanosheet branches in a particle were inspected by taking Fast-Fourier transforms across an image of intersecting nanosheet branches

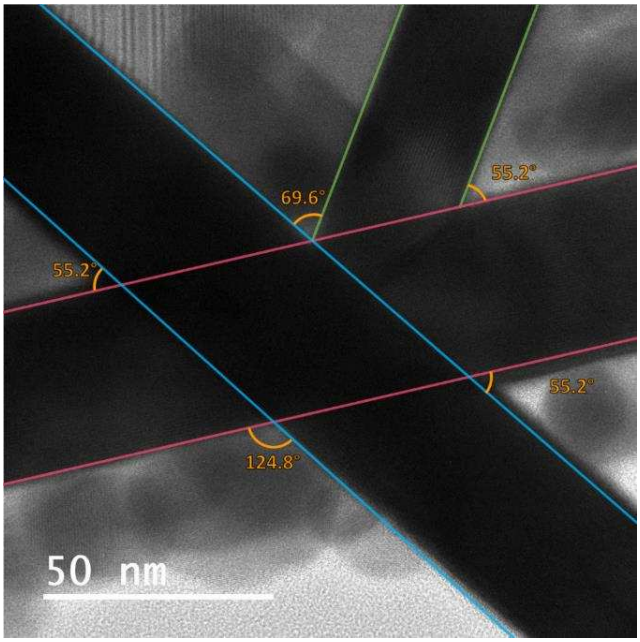

Figure 4.7. TEM image of branched nanosheet with angles between branches shown.

(Figure 4.8). The FFTs show the transition from one crystalline domain (Figure 4.8a), through the twin boundary (Figure 4.8c) to a second crystalline domain (Figure 4.8e).

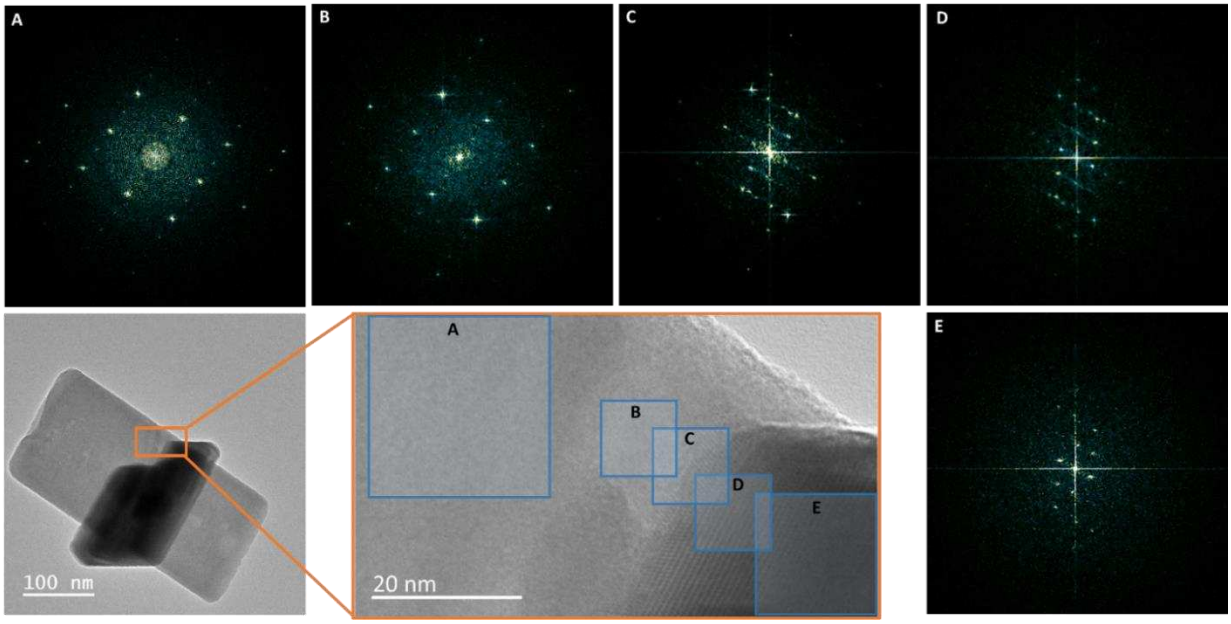

Figure 4.8. TEM image of branched nanosheet with FFTs taken across the twin plane.

4.3.5 Identification of a twin plane

To determine a possible twin plane for the twinning we observe, it is helpful to first evaluate twinning in the case of the sulfide, as it is isostructural with the selenide. Hoffman and Nespolo propose that twinning occurs along the (104) in chalcostibite because this plane is rich with metal atoms, thus their position is minimally affected by twinning, and upon a glide symmetry operation, shares many of the same crystal lattice points with the untwinned lattice. Nespolo evaluates the degree of structural restoration and finds that the atom displacements of the twin are compared to if the crystalline domain continued are minimal,[14] and our representation of these twinning operations is shown in figure 4.9. Hoffman reports that $CuSbS_2$ is likely a contact twin, in which a twinned and untwinned crystallite come together to share a single plane. Twinning in

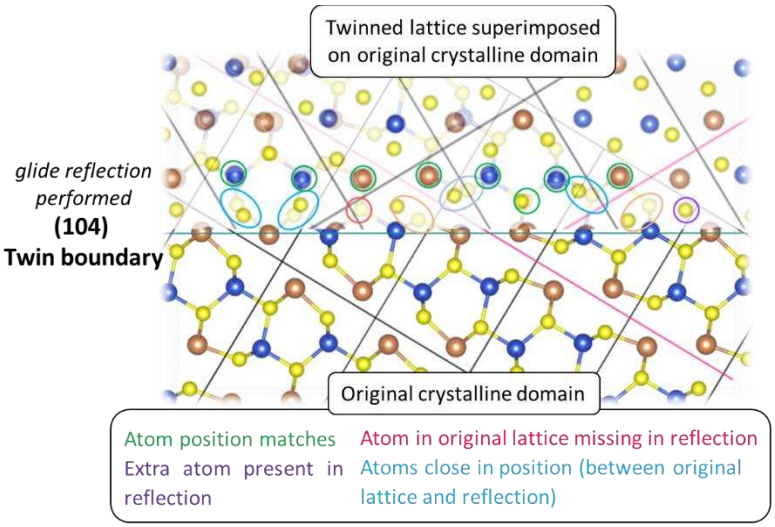

Figure 4.9. Our representation of possible twin operations across the (104) twin plane in $CuSbS_2$, including (A) a reflection and (B) glide reflection.

the (104) may be favorable due to the 2_1 screw axes present in <020>, as the n-glide reflection over this plane maps atoms to similar position as the screw axes. We hypothesized that as the *Pnma* structure has screw axes along all 3 crystallographic directions, the twinning in this structure for both the sulfide and selenide may both be related to this symmetry element and could explain why twinning seems to occur in the plane.

To account for the branching observed in the selenide, a candidate twin plane must be perpendicular to the (200) and oriented at a ~35° angle to the (002), and a twin operation must generate atom positions such that the lattice is somewhat restored, such that a substructure is retained throughout the crystal.[20] Because rotation and/or bending of nanosheets on the TEM grid is possible, we also looked at planes that are close to 55°. If the twin plane is exactly perpendicular to the (002), using the first two criteria, three lattice planes are likely for twinning to original from: (015), (0 2 11), and (016), with the expected angles that would result between planes shown in figure 4.10.

Based solely on the plane that is closest to our angle measurement, 55.2±1.2°, the (0 2 11) could be identified as the twin plane. This plane does appear to be metal rich, which is also the case for the reported chalcostibite twin plane. However, when the (0 2 11) is considered in relation to the 2_1 screw axes, we observe minimal similarities. We would expect that a plane likely to twin would be oriented such that a reflection or rotation from the plane would result in similar structural motifs, for example mapping some atoms onto the y=¼ special atomic positions in the crystal. As a comparison we looked at the (0 1 4), with the 1:4 ratio in the yz plane seeming to map atoms onto similar sites as the 2_1 screw axes (potentially in a similar manner as the (104) did for chalcostibite). However, as the expected angle between planes is nearly 10° smaller than the angles measured between branched nanosheets, we do not consider it a candidate plane. This leads us to believe that twinning may not occur through a symmetry operation to the sulfide. In these branched nanosheets, such as the one in figure 4.8, two crystallites appear to intersect one another and emerge through to the other side, making it a penetration twin, in which the surface where the two crystallites meet is more complex than a single plane. The fact that the sulfide twin is a contact twin and the ones observed here appear to be penetration twins further supports that different symmetry operations relate the crystalline domains.

We also acknowledge that the twinned particles could have slightly altered unit cell parameters from the single sheets that make them more susceptible to twinning. A slight change in the unit cell could substantially change the estimated angles between planes. The unit cell parameters used to calculate plane angles were those obtained from previous Rietveld refinements on single nanosheets from our work. A greater degree of twinning would need to be achieved synthetically in order to attribute differences in lattice parameters to twinned particles. A more accurate assessment of the degree of structural restoration obtained by a twin operation could be

obtained by comparing atom Wyckoff positions in the original and transformed lattice. To take it a step further, Marzouki et al. propose a method to evaluate the pseudo-eigensymmetry of the crystallographic orbits in the Wyckoff positions.[20] Either of these methods could be employed in future work to evaluate the likelihood that the proposed twin plane and twin operation accurately describe the branched nanosheets observed.

4.3.6 Hypothesized growth pathways

Our original hypothesis was that defected seeds formed initially and were preserved by rapid nanoparticle growth. In the OLA synthesis, growth likely occurs as was hypothesized. The presence of small, <100 nm defected sheets in 2 min aliquots may suggest that these form initially, and that rapid growth preserves the twinned seed (Figure 4.11). We cannot say definitively whether rapid growth onto defected seeds is a necessity, as we have not observed defected seeds in syntheses that result in unbranched particles. In the OLA/DDT synthesis, a substantial degree of branched sheets was only observed at long times. No small, defected seeds are observed, and the increased branched sheets at longer times may suggest that defected seeds either form throughout the synthesis, or that twinning originates as a nanosheet has already reached a substantial size. However, it is also possible that single branched nanosheets that form at shorter times are more difficult to identify, and that at longer times, the large agglomerates are much more apparent (the number could be comparable). The fact that the longer injection time changed the degree of twinning would suggest that the species available for nucleation and growth early in the synthesis are important. However, as the injection is room temperature, into a hot reaction medium, it is not clear whether it is the constant supply of Se precursor, or the more consistent flask temperature as injection occurs, that favors the formation of branched nanosheets. Additional syntheses will be

performed to assess the importance of these variables, and their potential role in the reaction pathway toward branched nanosheet formation.

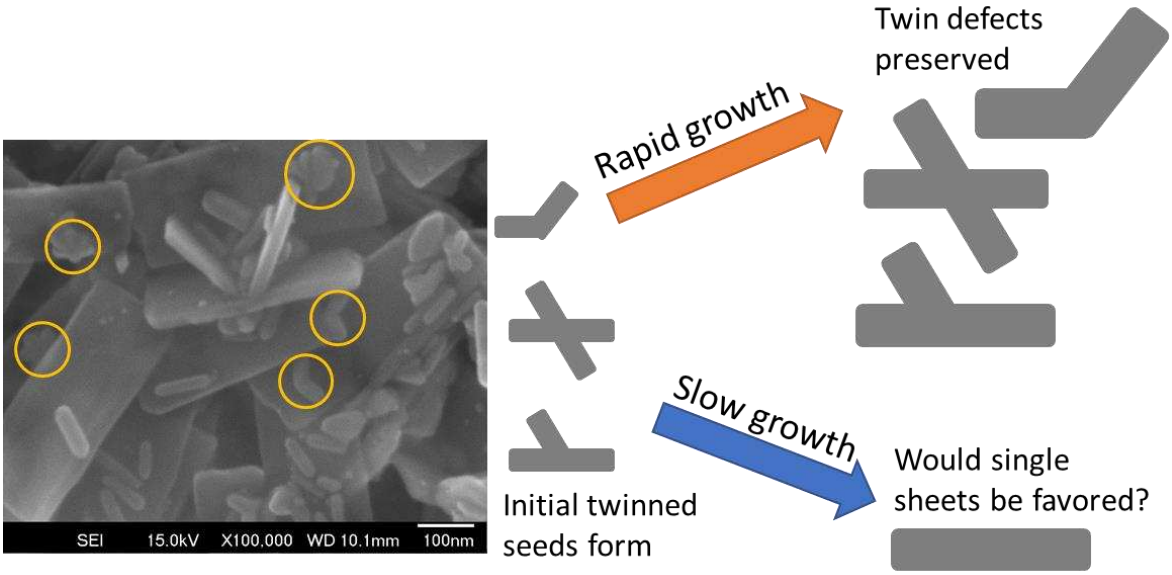

Figure 4.11. (A) SEM image showing the presence of small, <100 nm branched nanosheets in the 2 min aliquot of the OLA only synthesis. (B) Scheme showing proposed growth pathway of $CuSbSe_2$ branched nanosheets when defected seeds form initially.

4.4 Conclusions

We were able to induce nanosheet branching in various $CuSbSe_2$ syntheses. As branching occurs at consistent angles that cannot be explained by orthorhombic symmetry, and branches are separate crystalline domains that change orientation, we propose that these nanosheets are twinned. With the increased frequency of branched nanosheets in the OLA/LiHMDS synthesis, angles can be measured with a much higher frequency in TEM images, which will allow us to report a branching angle of 55.2±1.2°. Interestingly, the twinning we observe does not occur on the same twin plane as has been observed in literature for the analogous sulfide system. While we were able to propose possible twin planes, it is apparent even only with a qualitative inspection that the restoration of the lattice would likely not be as great as in the case of the (104) twin. Additional characterization would be necessary to support the identification of a different twin plane.

Specifically, future work will employ 4D STEM, which allows mapping at 3-5 nm spots across the sample, which would allow us to see the change in structure as we map across the twin boundary in much more detail than done in this work. Strain in the diffraction patterns (distinguishable by deviation in d spacings), would be expected near the boundary. Elucidating the twinning reaction pathway would be useful for inducing twinning in other systems. *In situ* X-ray absorption and scattering techniques would help to identify and quantify important intermediates, such as the initial active species, as well as track the formation of the initial nanoparticle seeds.

References

(1) Ortega, S.; Ibáñez, M.; Liu, Y.; Zhang, Y.; Kovalenko, M. V.; Cadavid, D.; Cabot, A. Bottom-up Engineering of Thermoelectric Nanomaterials and Devices from Solution-Processed Nanoparticle Building Blocks. *Chem. Soc. Rev.* **2017**, *46* (12), 3510–3528. https://doi.org/10.1039/C6CS00567E.

(2) Zhu, Q.; Wang, S.; Wang, X.; Suwardi, A.; Chua, M. H.; Soo, X. Y. D.; Xu, J. Bottom-Up Engineering Strategies for High-Performance Thermoelectric Materials. *Nano-Micro Lett.* **2021**, *13* (1), 119. https://doi.org/10.1007/s40820-021-00637-z.

(3) Zhang, A.; Zhang, B.; Lu, W.; Xie, D.; Ou, H.; Han, X.; Dai, J.; Lu, X.; Han, G.; Wang, G.; Zhou, X. Twin Engineering in Solution-Synthesized Nonstoichiometric Cu_5FeS_4 Icosahedral Nanoparticles for Enhanced Thermoelectric Performance. *Adv. Funct. Mater.* **2018**, *28* (10), 1705117. https://doi.org/10.1002/adfm.201705117.

(4) Wei, Y.; Zhou, Z.; Jiang, P.; Zheng, S.; Xiong, Q.; Zhang, B.; Wang, G.; Lu, X.; Han, G.; Zhou, X. Phase Composition Manipulation and Twin Boundary Engineering Lead to Enhanced Thermoelectric Performance of Cu_2SnS_3. *ACS Appl. Energy Mater.* **2021**, *4* (9), 9240–9247. https://doi.org/10.1021/acsaem.1c01483.

(5) Yu, Y.; He, D.-S.; Zhang, S.; Cojocaru-Mirédin, O.; Schwarz, T.; Stoffers, A.; Wang, X.-Y.; Zheng, S.; Zhu, B.; Scheu, C.; Wu, D.; He, J.-Q.; Wuttig, M.; Huang, Z.-Y.; Zu, F.-Q. Simultaneous Optimization of Electrical and Thermal Transport Properties of $Bi_{0.5}Sb_{1.5}Te_3$ Thermoelectric Alloy by Twin Boundary Engineering. *Nano Energy* **2017**, *37*, 203–213. https://doi.org/10.1016/j.nanoen.2017.05.031.

(6) Miller, R. C.; Geiss, R. H.; Prieto, A. L. Olivine Crystal Structure-Directed Twinning in Iron Germanium Sulfide (Fe_2GeS_4) Nanoparticles. *ACS Nano* **2021**, *15* (7), 11981–11991. https://doi.org/10.1021/acsnano.1c03237.

(7) He, M.; Protesescu, L.; Caputo, R.; Krumeich, F.; Kovalenko, M. V. A General Synthesis Strategy for Monodisperse Metallic and Metalloid Nanoparticles (In, Ga, Bi, Sb, Zn, Cu, Sn, and Their Alloys) via in Situ Formed Metal Long-Chain Amides. *Chem. Mater.* **2015**, *27* (2), 635–647. https://doi.org/10.1021/cm5045144.

(8) Miller, R. C.; Neilson, J. R.; Prieto, A. L. Amide-Assisted Synthesis of Iron Germanium Sulfide (Fe_2GeS_4) Nanostars: The Effect of $LiN(SiMe_3)_2$ on Precursor Reactivity for Favoring Nanoparticle Nucleation or Growth. *J. Am. Chem. Soc.* **2020**, *142* (15), 7023–7035. https://doi.org/10.1021/jacs.0c00260.

(9) Luo, Y.; Du, C.; Liang, Q.; Zheng, Y.; Zhu, B.; Hu, H.; Khor, K. A.; Xu, J.; Yan, Q.; Kanatzidis, M. G. Enhancement of Thermoelectric Performance in $CuSbSe_2$ Nanoplate-Based Pellets by Texture Engineering and Carrier Concentration Optimization. *Small* **2018**, *14* (50), 1803092. https://doi.org/10.1002/smll.201803092.

(10) Li, D.; Qin, X. Y. Thermoelectric Properties of $CuSbSe_2$ and Its Doped Compounds by Ti and Pb at Low Temperatures from 5to310K. *J. Appl. Phys.* **2006**, *100* (2), 023713. https://doi.org/10.1063/1.2218592.

(11) Zhang, D.; Yang, J.; Jiang, Q.; Fu, L.; Xiao, Y.; Luo, Y.; Zhou, Z. Ternary $CuSbSe_2$ Chalcostibite: Facile Synthesis, Electronic-Structure and Thermoelectric Performance Enhancement. *J. Mater. Chem. A* **2016**, *4* (11), 4188–4193. https://doi.org/10.1039/C6TA00039H.

(12) Chen, T.; Ming, H.; Qin, X.; Zhu, C.; Huang, L.; Hou, Y.; Li, D.; Zhang, J.; Xin, H. Improving the Power Factor and Figure of Merit of P-Type $CuSbSe_2$ via Introducing Sb Vacancies. *J. Mater. Chem. C* **2021**, *9* (41), 14858–14865. https://doi.org/10.1039/D1TC02728J.

(13) Hofmann, W. Strukturelle und morphologische Zusammenhänge bei Erzen vom Formeltyp ABC_2. *Z. Für Krist. - Cryst. Mater.* **1933**, *84* (1–6), 177–203. https://doi.org/10.1524/zkri.1933.84.1.177.

(14) Nespolo, M. Twinning in Chalcostibite Revisited. *Eur. J. Mineral.* **2018**, *30* (5), 967–973. https://doi.org/10.1127/ejm/2018/0030-2764.

(15) Kale, A. R.; Bullett, W. E.; Prieto, A. L. Controlling Phase Conversion of Cu-Sb-Se Nanoparticles through the Use of an Amide Base. *Nano Lett.* **2023**. https://doi.org/10.1021/acs.nanolett.3c00506.

(16) Liu, Y.; Yao, D.; Shen, L.; Zhang, H.; Zhang, X.; Yang, B. Alkylthiol-Enabled Se Powder Dissolution in Oleylamine at Room Temperature for the Phosphine-Free Synthesis of Copper-Based Quaternary Selenide Nanocrystals. *J. Am. Chem. Soc.* **2012**, *134* (17), 7207–7210. https://doi.org/10.1021/ja300064t.

(17) Hsiang, H. I.; Yang, C. T.; Tu, J. H. Characterization of $CuSbSe_2$ Crystallites Synthesized Using a Hot Injection Method. *RSC Adv.* **2016**, *6* (101), 99297–99305. https://doi.org/10.1039/c6ra20692a.

(18) Agocs, D. B.; Danna, T.; Prieto, A. L. Ambient Surface Stability of Thin Film Nanocrystalline Cu_3SbSe_4 and Structure-Property Relationships. *ACS Appl. Energy Mater.* **2019**, *2* (3), 1903–1910. https://doi.org/10.1021/acsaem.8b02019.

(19) Agocs, D. Hot Injection Synthesis and Characterization of Copper Antimony Selenide Non-Canonical Nanomaterials toward Earth-Abundant Renewable Energy Conversion, Colorado State University, 2018.

(20) Marzouki, M. A.; Souvignier, B.; Nespolo, M. Analysis of the Structural Continuity in Twinned Crystals in Terms of Pseudo-Eigensymmetry of Crystallographic Orbits. *IUCrJ* **2014**, *1* (1), 39–48. https://doi.org/10.1107/S2052252513026493.

CHAPTER V: SUMMARY, OUTLOOK, AND EXTENSION OF PRECURSOR REACTIVITY CONTROL TO SOFT BASES

5.1 Summary

In this dissertation, we focused on how to manipulate precursor reactivity in order to obtain control over phase and morphology in the Cu-Sb-Se system. In Chapter I, we discussed precursor reactivity and how it is described and manipulated in multinary chalcogenide syntheses, as well as the framework through which some of these interactions can be understood (HSAB theory, bond strengths). We motivated the study of the Cu-Sb-Se phases due to their energy-relevant applications, as well as the phases' unique structures and phase space. In literature, formation of anisotropic phases was common, and challenges with phase-pure syntheses were observed due to the similarities in composition and stability between the ternaries. This made the Cu-Sb-Se system an ideal choice for probing precursor reactivity, and in our work, we frequently found that multiple anisotropic phases were formed. In order to deconvolute anisotropic nanocrystalline Cu_3SbSe_3 and $CuSbSe_2$ phases in PXRD patterns, we developed a methodology for performing Rietveld refinements on such systems, which is discussed in Chapter II. While we suggest that additional characterization, such as electron microscopy, is needed to supplement such refinements, the publication of this resource builds on work addressing considerations for nanocrystalline XRD refinements and will allow users to perform more accurate Rietveld refinements on nanoscale materials and obtain physically meaningful structural information, which is particularly important given the growing popularity of performing refinements in such systems.

In Chapters III and IV, we discussed the bulk of our synthetic work in the Cu-Sb-Se system. Chapter III details the decomposition reaction of Cu_3SbSe_3 to $CuSbSe_2$. We used the Rietveld

refinement methodology developed in Chapter II to quantify the percentages of phases present, which allowed us to show that decomposition to the $CuSbSe_2$ phase occurs faster with the addition of base. In Chapter IV, we investigated morphological control, with specific focus on twinning in $CuSbSe_2$. We were able to induce twinning under two different sets of synthetic conditions and hypothesize what may be changing in terms of the active species to encourage this phenomenon. In this final chapter, we will discuss some key takeaways and future studies related to our work in the Cu-Sb-Se system—most importantly that while we can hypothesize about the changes in precursor reactivity that must have occurred to result in the formation of different phases and morphologies, additional characterization of the intermediates that occur prior to nucleation is needed. We leave the reader with some final notes on the promising direction of in situ studies in the field as a whole and how these could be used in our work.

5.2 Areas for consideration and future study

5.2.1 The use of LiHMDS as a widely applicable precursor for tuning reactivity requires additional characterization

In the phase control study of Cu-Sb-Se in Chapter III, our initial goal was to investigate if the use of LiHMDS as a reagent to balance reactivity in NP synthesis was widely applicable to a variety of systems. In a system in which precursor reactivity is balanced, we expect compounds to form of the stoichiometry present in the reaction flask. While the addition of LiHMDS did allow us to control the rate of conversion of the Cu_3SbSe_3 to the $CuSbSe_2$, we continually observed some formation of Cu_3SbSe_3 at short times in reactions with a 1:1:2 ratio of Cu:Sb:Se. To explain why LiHMDS is unable to control initial phase formation, we originally proposed that the hard-soft acid base mismatch between Cu (I) and Sb (III) means that the oleylamide species coordinates less strongly to the Cu than the Sb, making Cu incorporate faster.

Why LiHMDS is able to control phase formation in the Fe-Ge-S system, but not for the Cu-Sb-Se system, could be further rationalized within the hard-soft acid base framework— while Ge (IV) is a hard cation and Fe (II) could be classified as "intermediate," it is still harder than Cu (I), which is soft and Sb (III) is somewhat hard. Because the counterion, Cl^-, is hard as is the OLA, which is the solvent as well as ligand, any complex formed with the Cu (I) is going to be less stable than those formed with Sb (III). We should note that coordination to the silylamide is also possible and has been observed previously in for some metals in OLA.[1] We might expect that the RNH^- would be softer than RNH_2, making the RNH^- coordinate preferentially to the Cu (I), rather than Sb (III). Although syntheses with Cu (I) and other harder cations, such as In (III), have been able to balance reactivity with LiHMDS successfully in TOP,[2,3] the coordinating ligand is the silylamide itself, and the silylamide may coordinate more strongly to Cu than its oleylamide counterpart.

Being able to understand what makes a reagent able to allow phase control well in one system but not another is a crucial piece to developing more universal principles to guide tuning precursor reactivity in new systems. To address the questions discussed above, identification of the coordination complexes formed in situ would be particularly helpful—in situ X-ray absorption measurements would aid in the identification of coordination complexes,[4] and when paired with in situ X-ray scattering,[5] would allow nucleation and growth of nanoparticles to be related to the complexes formed. In the absence of a facility that performs in situ techniques, the isolation and precipitation of complexes from solution remain a crucial piece. H-NMR has been used to identify coordination complexes, both in their native solutions and precipitated,[1,4] and can be a useful technique if optimized. Preliminary H-NMR studies were attempted on simple control reactions in our system in which the separate metals were combined with just oleylamine, or also LiHMDS;

however complex isolation was a challenge and products were slightly contaminated, making definitive identification of complex formation difficult.

The use of HSAB theory to evaluate the potential stability (and therefore hypothesized reactivity) of a given complex, is a good starting point, but ultimately more quantitative values are desired. Bond dissociation energies (BDEs) allow this, but we have not been able to find many of the BDEs of interest for copper chalcogenide syntheses in literature. In particular, we have not found BDEs for Cu (I) – RNH_2, which is a very common complex in copper chalcogenide syntheses. We propose that this is an area where theorists and experimentalists could collaborate to generate BDE values for various metal-ligand bonds under relevant reaction conditions.

5.2.2 Developing more precise control over twinning in $CuSbSe_2$

In Chapter IV, we discussed two synthesis methods that were used to induce twinning. While mentioned briefly in the previous chapter, we will elaborate on future directions here. Upon comparing the two syntheses, it appears that twinned sheets are favored at long times in the OLA/DDT synthesis and are present at short times in the amide-promoted synthesis. Better understanding the reaction pathway of the two reactions conditions will allow us to determine what favors twinned nanosheet formation and how we could further encourage it in both syntheses. Of particular interest is the OLA/DDT synthesis as twinned sheets being favored at long times contradicts our growth pathway. We plan to perform syntheses that test the importance of a constant supply of Se precursor vs consistent flask temperature, and will image aliquots at short times in TEM to rule out the presence of tiny twinned Cu-Sb-Se nanosheets, in case they could be too small to see in SEM to shed additional light on the reaction pathway. Farther in the future, in situ X-ray diffraction and scattering techniques would help to identify and quantify important

intermediates, such as the initial active species, as well as track the formation of the initial nanoparticle seeds.

Additional future directions for this work are focused on characterization. We proposed a few possible twin planes based characterization of TEM, but as this contradicts what has been seen for the chalcostibite structure in literature, additional characterization of the atomic structure surrounding the twin plane is necessary to support a specific twin plane. We plan to perform 4D STEM, in which we can record diffraction patterns at 3-5 nm spots mapped across potential twin boundaries, which would allow us to see the change in structure as we map across the twin boundary. We expect to see strain in the diffraction patterns near the boundary, and identifying which planes are more strained than others would help to support along which plane twinning occurs.

5.2.3 Phase control through soft base ligand coordination to Cu

As discussed in Chapter III, the addition of LiHMDS does not allow much control over initial phase formation in our Cu-Sb-Se synthesis. As such, we pursued an alternative approach to controlling reactivity, attempting to selectively stabilize each cation, as has been used in literature.[6,7] We hypothesized that the use of soft base ligands would allow us to decrease the reactivity of the Cu, allowing Cu and Sb cations to incorporate at a more equal rate. To extend upon the amide base work, in a collaboration with William Bullett, a series of soft bases were investigated, including oleylamine (OLA), trioctylphosphine (TOP), trioctylphosphine oxide (TOPO), and dodecanethiol (DDT). To decrease the variables changed when ligands were swapped, as well as having a better picture of the interacting species in solution, we used a majority solvent of octadecane, and ligands were added in a 6:1 ratio of ligand to each cation (allowing complete coordination if up to 6 bonds, octahedral coordination, were formed). Most reactions still

resulted in the initial formation of Cu_3SbSe_3, which supports one of our hypotheses from Chapter III that perhaps the injection of room-temperature Se favors the Se-deficient phase. Attempts to heat the Se precursor resulted in a wide range of products, so we will need to pursue a different method to test this hypothesis: one option is to perform a heat-up synthesis containing the Se in the reaction flask or injecting the cations into solution. Both of these methods have been used successfully to form Cu-Sb-Se ternary nanoparticles.

One synthesis differed considerably from most of the other Cu-Sb-Se syntheses (in which Cu_3SbSe_3 is favored at short times and decomposes to $CuSbSe_2$ at long times). Powder X-ray

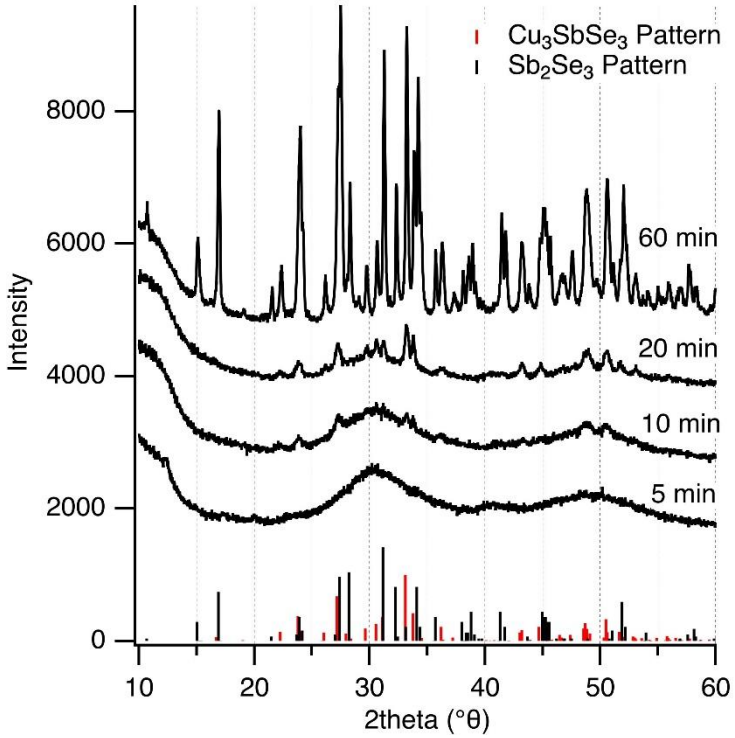

Figure 5.1. XRD pattern of products from the TOPO synthesis from 5-60 min aliquots.

diffraction patterns (PXRD) show the changes in crystalline phases that occur over time with TOPO as the main ligand (Figure 5.1). Interestingly, the products are poorly crystalline at 5 min, and characterization with TEM-EDS shows that these particles have a Cu:Sb:Se ratio of 1:1.1:2.

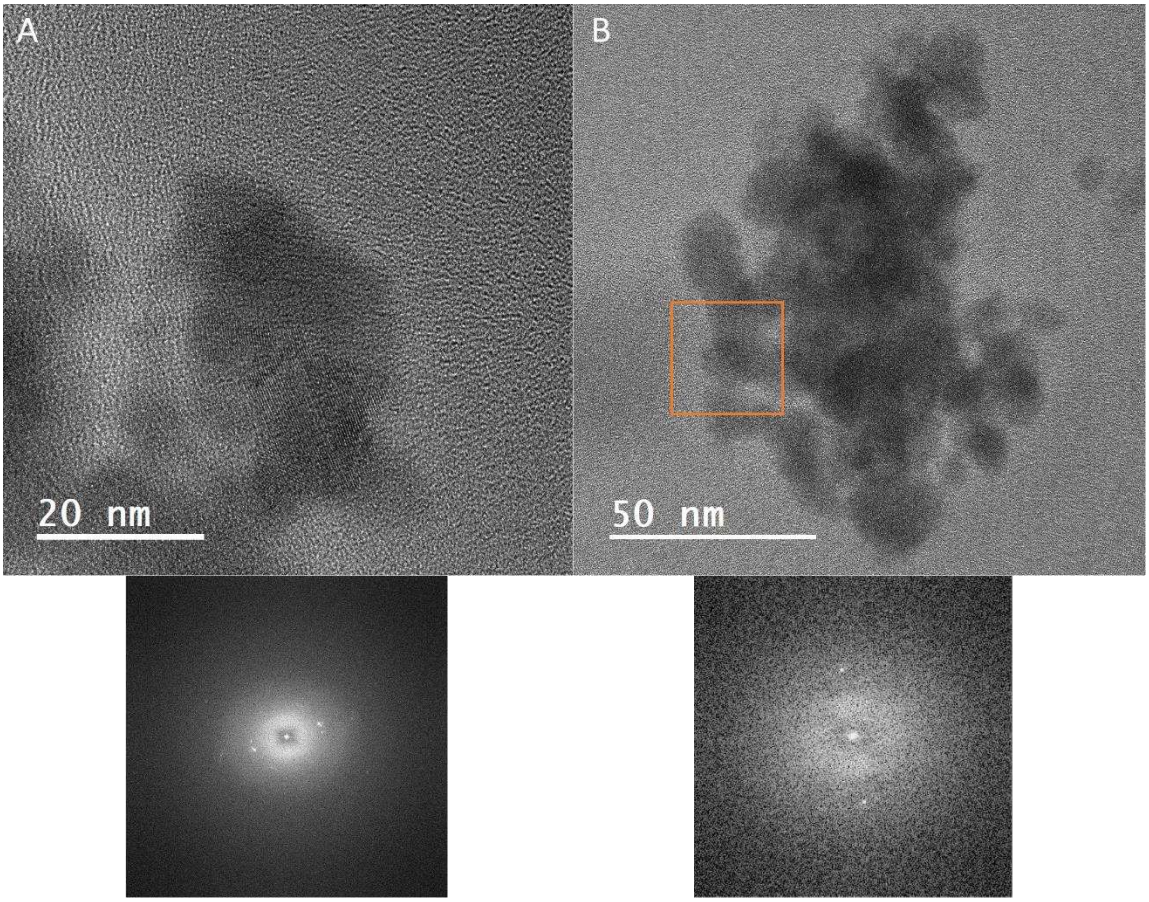

Figure 5.2 TEM images of particles from 5 min synthesis and corresponding FFT images.

Minimal lattice planes were observed in HR-TEM—of ~50 images of particles, only 2 FFTs contained identifiable diffraction spots (Figure 5.2). Electron diffraction was later attempted on this synthesis, though no diffraction was observed from the particles. The PXRD pattern for these particles is similar to one reported by Yarema et al.,[8] and both are considerably right-shifted from the $CuSbSe_2$ bulk reference pattern, suggesting a compressed unit cell. Thus, we suggest the initial phase formed is a strained and poorly crystalline $CuSbSe_2$ phase.

At longer times in the TOPO reaction, Cu_3SbSe_3 and Sb_2Se_3 are observed by XRD (Figure 5.1), and as such it appears that a reverse phase conversion pathway is observed to our previous reactions in OLA: $CuSbSe_2$ is formed initially and converts to Cu_3SbSe_3 over time.

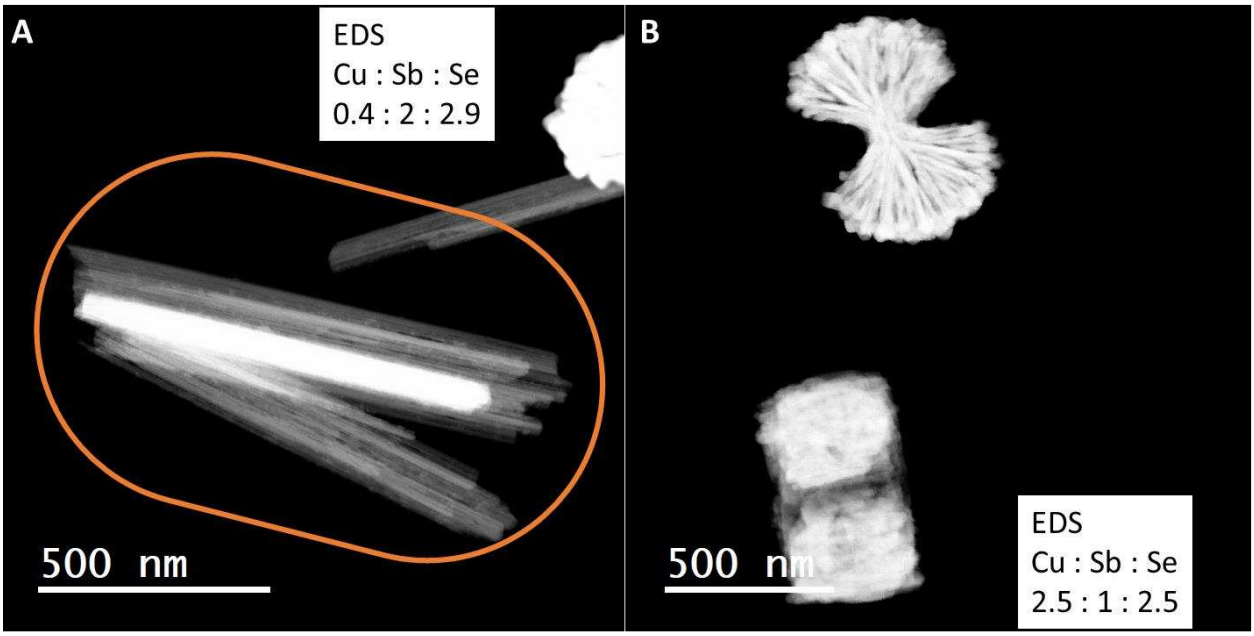

Figure 5.3. TEM images of (A) sheets and (B) bowties from 60 min synthesis.

Characterization of these products in TEM show that sheets appear to be Sb_2Se_3 with potential Cu incorporation, while bowties are likely Sb-rich Cu_3SbSe_3 (Figure 5.3). However, there was detectable Cu in EDS scans taken of background, thus EDS will be reproduced at the 60 min aliquot. Rietveld refinements will be performed on the 60 min diffraction pattern to determine if phases are stoichiometric or not. Additionally, performing TEM and EDS on intermittent time aliquots will shed light on the potential reaction pathway, and will help address whether Cu appears to intercalate into Sb_2Se_3 sheets. We propose that the TOPO must act as a stabilizer: either more stable Cu coordination complexes are formed with TOPO that allow for a compound to form that is reflective of the starting stoichiometry, or TOPO is more effective at stabilizing these small, strained particles. We performed a synthesis with a Cu:Sb:Se ratio of 3:1:3, in which mostly the Cu_3SbSe_3 phase formed, which supports the first hypothesis that TOPO allows the formation of a phase reflective of the starting stoichiometry.

The persistence of smaller particles due to the stabilization of TOPO is supported by literature. In a $CuInS_2$ synthesis, an excess of TOPO compared to amine was required in order to stabilize small particles,[9] and TOPO may have the same stabilizing effect on small $CuSbSe_2$ particles here, causing them to be the only product initially observed. It is possible that $CuSbSe_2$ particles form in syntheses with other ligands but are unstable and rapidly decompose, and other products also begin to form before the first time aliquot. When comparing the poorly crystalline PXRD pattern to the apparent background observed in previous reactions, the two appear to be a match. This supports that small $CuSbSe_2$ particles could be present in previous Cu-Sb-Se reactions, but they may be masked by more crystalline products in PXRD and by thicker/larger platelets and sheets in TEM. This case of tiny, poorly crystalline $CuSbSe_2$ particles emphasizes the importance of using alternative characterization techniques to ensure that other phases are not missed. As a start, we could attempt size-selective precipitation to isolate small particles in previous syntheses for characterization with TEM/EDS to determine if they match the $CuSbSe_2$ phase.

The dissolution of the initial $CuSbSe_2$ particles over time is expected, as this phase appears to be strained and poorly crystalline, and the small particles are likely not very stable. What is considerably surprising is the formation of the metastable phase Cu_3SbSe_3, which emerges in the reaction between 10 to 20 min, and persists at 60 min. The formation of Sb_2Se_3 alongside this phase is less surprising—Sb_2Se_3 has a low, favorable formation energy and is required to balance the initial stoichiometry of precursors added to the reaction flask. However, if the change in formation energy of the reaction $CuSbSe_2 \rightarrow Cu_3SbSe_3 + Sb_2Se_3$ (as bulk solids) is determined from calculated values of the compounds, the formation energy is a high, positive value.[10] We propose that this means that either the large entropy increase caused by the formation of the highly disordered Cu_3SbSe_3 is enough to make this reaction favorable, or perhaps the surface energy of

the tiny, strained $CuSbSe_2$ particles is much higher than its bulk counterpart. To further test how the thermodynamics of reaction pathway have been affected by the presence of TOPO we will begin by allowing particle growth to occur over a much longer period, such as 4-8 hours. It is possible that the reaction is simply slowed down considerably with TOPO, and that thermodynamic $CuSbSe_2$ would reform and persist as sheets, which is the morphology we usually observe at long times. Future work in the soft base ligand studies involves the isolation and characterization of metal coordination complexes with the different ligands. As has been discussed throughout this outlook, understanding speciation is crucial to developing a more comprehensive picture of the reaction pathway.

5.3 Outlook on precursory reactivity studies in nanoparticle synthesis

As precursor reactivity becomes more well-defined and is discussed more specifically in the field, strategies for predicting reactivity in new systems will become more accessible. An understanding of how different active species or intermediates lead to different products makes it easier to select reagents to direct specific products, which is required to put the field closer to the application of retrosynthesis in nanocrystal reactions.[11,12]

The best approach would involve increased characterization of the active species or complexes that form in reactions, *in situ*, as there is no guarantee that the species characterized ex situ are the same as those present in situ in the reaction flask, this calls for the use of *in situ* X-ray absorption and X-ray scattering techniques that have become increasingly common to monitor nanoparticle speciation as well as nucleation and growth.[4,13,14] This would allow us not only to better characterize intermediates as they form and decompose, but also track the formation of nanoparticles in real time, making modeling of nanoparticle nucleation and growth kinetics possible. Such studies would allow us to describe reactions pathways more clearly and

quantitatively. The increased prevalence of such *in situ* studies in the field as a whole could lead to clearer and more detailed descriptions of reactivity in a variety of systems, making it easier to compare differences in reactivity between systems.

A few recent works further emphasize the importance of characterizing reaction intermediates[11,12] and bolster our argument for further work in this area. In one perspective, Loiudice and Buonsanti discuss in detail the variety of intermediates that have been characterized that form prior to nucleation. These included complexes and clusters, as well as larger scale intermediates, such as coordination polymers and mesophases.[11] In another perspective entitled "Chemical Considerations for Colloidal Nanocrystal Synthesis," De Roo discusses the interactions that occur between precursors, ligands, and solvents, and emphasizes examples of clear characterization.[12] Here he suggests standards of reporting and characterization that the field should adhere to, which is essential to being able to compare reactivity across different reactions from different labs. From these works, and others, it is clear that moving the field of nanocrystal synthesis forward will depend on furthering and wholistic definition and characterization of reaction intermediates and precursor reactivity.

References

(1) He, M.; Protesescu, L.; Caputo, R.; Krumeich, F.; Kovalenko, M. V. A General Synthesis Strategy for Monodisperse Metallic and Metalloid Nanoparticles (In, Ga, Bi, Sb, Zn, Cu, Sn, and Their Alloys) via in Situ Formed Metal Long-Chain Amides. *Chem. Mater.* **2015**, *27* (2), 635–647. https://doi.org/10.1021/cm5045144.

(2) Yarema, O.; Yarema, M.; Bozyigit, D.; Lin, W. M. M. M.; Wood, V. Independent Composition and Size Control for Highly Luminescent Indium-Rich Silver Indium Selenide Nanocrystals. *ACS Nano* **2015**, *9* (11), 11134–11142. https://doi.org/10.1021/acsnano.5b04636.

(3) Yarema, O.; Yarema, M.; Lin, W. M. M.; Wood, V. Cu-In-Te and Ag-In-Te Colloidal Nanocrystals with Tunable Composition and Size. *Chem. Commun.* **2016**, *52* (72), 10878–10881. https://doi.org/10.1039/c6cc05571k.

(4) Strach, M.; Mantella, V.; Pankhurst, J. R.; Iyengar, P.; Loiudice, A.; Das, S.; Corminboeuf, C.; van Beek, W.; Buonsanti, R. Insights into Reaction Intermediates to Predict Synthetic Pathways for Shape-Controlled Metal Nanocrystals. *J. Am. Chem. Soc.* **2019**, *141* (41), 16312–16322. https://doi.org/10.1021/jacs.9b06267.

(5) Just, J.; Coughlan, C.; Singh, S.; Ren, H.; Müller, O.; Becker, P.; Unold, T.; Ryan, K. M. Insights into Nucleation and Growth of Colloidal Quaternary Nanocrystals by Multimodal X-Ray Analysis. *ACS Nano* **2021**, *15* (4), 6439–6447. https://doi.org/10.1021/ACSNANO.0C08617.

(6) Li, S.; Tang, X.; Zang, Z.; Yao, Y.; Yao, Z.; Zhong, H.; Chen, B. I-III-VI Chalcogenide Semiconductor Nanocrystals: Synthesis, Properties, and Applications. *Chin. J. Catal.* **2018**, *39* (4), 590–605. https://doi.org/10.1016/S1872-2067(18)63052-9.

(7) Coughlan, C.; Ibáñez, M.; Dobrozhan, O.; Singh, A.; Cabot, A.; Ryan, K. M. Compound Copper Chalcogenide Nanocrystals. *Chem. Rev.* **2017**, *117* (9), 5865–6109. https://doi.org/10.1021/acs.chemrev.6b00376.

(8) Yarema, O.; Yarema, M.; Moser, A.; Enger, O.; Wood, V. Composition- And Size-Controlled I-V-VI Semiconductor Nanocrystals. *Chem. Mater.* **2020**, *32* (5), 2078–2085. https://doi.org/10.1021/acs.chemmater.9b05191.

(9) Niezgoda, J. S.; Harrison, M. A.; McBride, J. R.; Rosenthal, S. J. Novel Synthesis of Chalcopyrite $Cu_xIn_yS_2$ Quantum Dots with Tunable Localized Surface Plasmon Resonances. *Chem. Mater.* **2012**, *24* (16), 3294–3298. https://doi.org/10.1021/cm3021462.

(10) Jain, A.; Ong, S. P.; Hautier, G.; Chen, W.; Richards, W. D.; Dacek, S.; Cholia, S.; Gunter, D.; Skinner, D.; Ceder, G.; Persson, K. A. Commentary: The Materials Project: A Materials Genome Approach to Accelerating Materials Innovation. *APL Mater.* **2013**, *1* (1). https://doi.org/10.1063/1.4812323.

(11) Loiudice, A.; Buonsanti, R. Reaction Intermediates in the Synthesis of Colloidal Nanocrystals. *Nat. Synth.* **2022**, *1* (5), 344–351. https://doi.org/10.1038/s44160-022-00056-x.

(12) De Roo, J. Chemical Considerations for Colloidal Nanocrystal Synthesis. *Chem. Mater.* **2022**, *34* (13), 5766–5779. https://doi.org/10.1021/acs.chemmater.2c01058.

(13) Whitehead, C. B.; Finke, R. G. Particle Formation Mechanisms Supported by in Situ Synchrotron XAFS and SAXS Studies: A Review of Metal, Metal-Oxide, Semiconductor and Selected Other Nanoparticle Formation Reactions. *Mater. Adv.* **2021**, *2* (20), 6532–6568. https://doi.org/10.1039/D1MA00222H.

(14) Pankhurst, J. R.; Castilla-Amorós, L.; Stoian, D. C.; Vavra, J.; Mantella, V.; Albertini, P. P.; Buonsanti, R. Copper Phosphonate Lamella Intermediates Control the Shape of Colloidal Copper Nanocrystals. *J. Am. Chem. Soc.* **2022**, *144* (27), 12261–12271. https://doi.org/10.1021/jacs.2c03489.

APPENDIX I: SUPPLEMENTARY INFORMATION FOR CHAPTER III:

SI Table of Contents

Experimental

Reagents. Copper (II) chloride ($CuCl_2$, 97%, Ridel-deHaen), antimony chloride ($SbCl_3$, ≥99%, Sigma-Aldrich), Selenium powder (Se, 99.99%, STREM chemical), lithium bis(trimethylsilyl)amide (LiHMDS, 97%, Sigma-Aldrich), n-butyllithium (n-BuLi, 2.7M in heptane, Sigma-Aldrich), ethanol (90%, Fisher Scientific), toluene (98%, Fisher Scientific) and hexanes (isomer mixture, Fisher Scientific) were used as received. Oleylamine (OLA, 70% technical grade, Sigma-Aldrich) was heated to 80 °C and degassed under vacuum for 2 h, and 1-dodecanethiol (DDT, ≥98%, Sigma-Aldrich) and trioctylphosphine (TOP, 90% tech., Sigma-Aldrich) were sparged with N_2 for 2 h prior to use.

Synthesis of Cu_3SbSe_3 and $CuSbSe_2$ nanocrystals. All precursors were prepared air-free in a N_2 glovebox, and reactions were run on a Schlenk line. In a 3-neck round bottom flask equipped with a thermocouple and condenser, 0.5 mmol $CuCl_2$, 0.5 mmol $SbCl_3$, and 4 or 7 mL oleylamine were combined. In the LiHMDS reactions, 1.0 mmol $LiN(SiMe_3)_2$ was also added to the reaction flask. To prepare the standard Se precursor, 1.0 mmol Se powder, 1 mL oleylamine, and 1 mL dodecanethiol were combined in a sealed vial, which was then stirred, then sonicated for 2 min (new sonicator) or 15 min (old sonicator). One synthesis was performed with a 4 mL injection of Se precursor, prepared as above with 2 mL oleylamine and 2 mL dodecanethiol. Another synthesis was performed with TOPSe, prepared by dissolving Se in 2 mL TOP. The flask was heated 90 °C under N_2 for 30 minutes, to allow full dissolution of precursors. Upon reaching 150 °C, the Se precursor was injected via syringe. Aliquots were quenched into plastic test tubes after the desired growth time.

Double injection syntheses. Double injection reactions used the same procedure as the standard synthesis with a single injection of the Se precursor, with an additional component (base or base with Sb) separated into a scintillation vial. The separated component was injected first, followed by the injection of the Se precursor 10 s after.

Washing. Particles were washed twice with a standard solvent/antisolvent procedure with toluene and ethanol in a 1:3 ratio and centrifugation at 5800 rpm for 5 min. Nanoparticles were re-dispersed in toluene by sonication between washes. Particles were washed a final time by dispersion in hexanes and centrifugation for 3 min.

Characterization. Powder X-ray diffraction (PXRD) was performed with a Bruker D8 Discover X-ray diffractometer using Cu Kα radiation (λ=1.54 Å). Particles dispersed in hexanes were drop-cast onto zero diffraction Si wafers. Scanning electron microscopy (SEM) images were

taken with a JEOL JSM-6500F field emission scanning electron microscope at 15 keV. Samples were prepared for SEM by drop-casting particles dispersed in hexanes onto carbon-taped Al stubs. Transmission electron microscopy (TEM) images were collected with a JEOL JEM-2100F TEM at 200 keV. Samples were prepared for TEM by drop-casting nanocrystal dispersions in hexanes onto Ni grids. Fast-Fourier transforms (FFTs) of high-resolution TEM images were performed using Digital Micrograph v3 software.

Rietveld Refinements

TOPAS v6 (Bruker AXS) software was used to perform Rietveld refinements on X-ray diffraction patterns (Table S3.1). A double-Voigt approach was used to fit peak profiles. An anisotropic fitting macro from Ectors et al. (ref 23 in main text) was used to fit anisotropic crystalline domains. The $CuSbSe_2$ sheets were fit with the cuboid model and Cu_3SbSe_3 ovular platelets were fit with the ellipsoid model. The weight percentage outputs from TOPAS of multiple phases were converted to mole percentages. Reactions are reproducible, and trends remain the same, though we note that there is slight variation in weight percentages obtained from reaction to reaction. Example Rietveld refinements are shown in Figure S4.

Table S3.1. Summary of crystalline phases identified by PXRD for standard reactions with 2 mL Se precursor volume. Rietveld refinements were used to obtain weight percentages, which were then converted to mole percentages.

Reaction	Flask volume (mL)	growth time (min)	$CuSbSe_2$ (mol %)	Error (mol %)	Cu_3SbSe_3 (mol %)	Error (mol %)
No base	7	2	26	9	74	9
		5	27	7	73	7
		10	41	5	59	5
		20	87	4	13	4
LiHMDS	7	2	34	8	66	8
		5	39	6	61	6
		10	53	5	47	5
		20	87	4	13	4
No base	4	2	32	6	68	6
		5	35	7	65	7
		10	40	5	60	5
		20	92	2	8	2
LiHMDS	4	2	51	7	49	7
		5	52	3	48	3
		10	60	4	40	4
		20	100	4	0	N/A

Control Discussion

Previous literature that injects LiHMDS commonly does so with TOP as the solvent. However, when a double injection with LiHMDS in TOP was performed in our system, only Sb particles were formed, as was also observed when TOPSe was used (Figure S3.13). As the problem appeared to be the use of TOP as the solvent, an injection of LiHMDS in toluene was tried as well as n-BuLi in hexanes. At 150 °C, base was injected first, shortly followed by Se. In both cases, minimal conversion to $CuSbSe_2$ was observed at 5 min (Figure S3.14), with less than 30% of products indexing to $CuSbSe_2$. Even more interesting is that additional conversion is not observed after 10 min, although full conversion was observed after 20 min. We hypothesize that that the

room-temperature base solution took additional time to form metal-oleylamide complexes when compared to the standard base reactions.

We then aimed to decouple the role of LiHMDS in the reaction by separating it into an injection solution with Sb. We hypothesized that the addition of LiHMDS would increase the reactivity of the Sb precursor alone, which would make more reactive Sb species than the Cu ones and encourage formation of $CuSbSe_2$. Interestingly, mostly Cu_3SbSe_4 formed regardless of whether base was present (Figure S3.15). Despite the addition of LiHMDS, the Sb precursor appears to be less reactive than the Cu. This may be due to the Sb precursor being at room temperature, so the complex has less energy than the Cu complex, inhibiting the complex degradation required for synthesis. Cu_3SbSe_4 likely formed because it is the most Sb deficient phase.

A final control was performed in which the solution of Sb and LiHMDS was heated (Figure S3.16), to test whether the injection of a precursor below reaction temperature is an inhibiting factor in its incorporation. Interestingly, a similar percentage of Cu_3SbSe_3 and $CuSbSe_2$ is formed as compared to the 7 mL single injection, but more $CuSbSe_2$ is present than in the room temperature double injections. This suggests that $CuSbSe_2$ growth is inhibited by the injection of a room-temperature precursor, but also that separating Sb and LiHMDS is still not an effective way of increasing the reactivity of only the Sb and not the Cu. Reactivity of Sb is likely more effectively controlled using ligands that take into account the disparity of hardness of the Cu^+ and Sb^{3+}. It is also possible that the initial formation of the Cu_3SbSe_3 is encouraged by a less reactive Se precursor, and that continuing to increase the reactivity of Sb will not result in initial formation of $CuSbSe_2$.

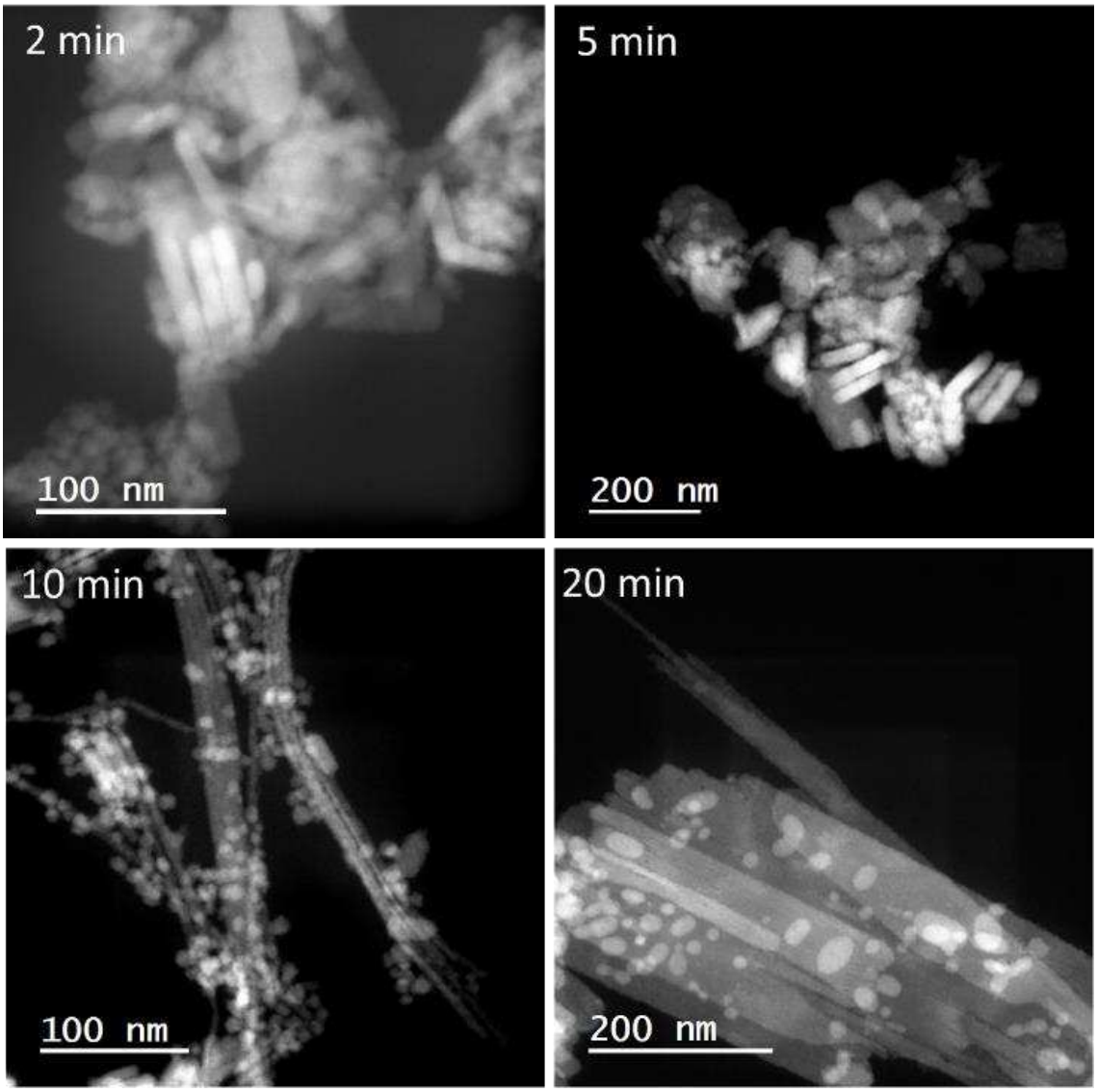

Figure S3.1. STEM images of nanoparticles from each time aliquot of the 7 mL OLA synthesis.

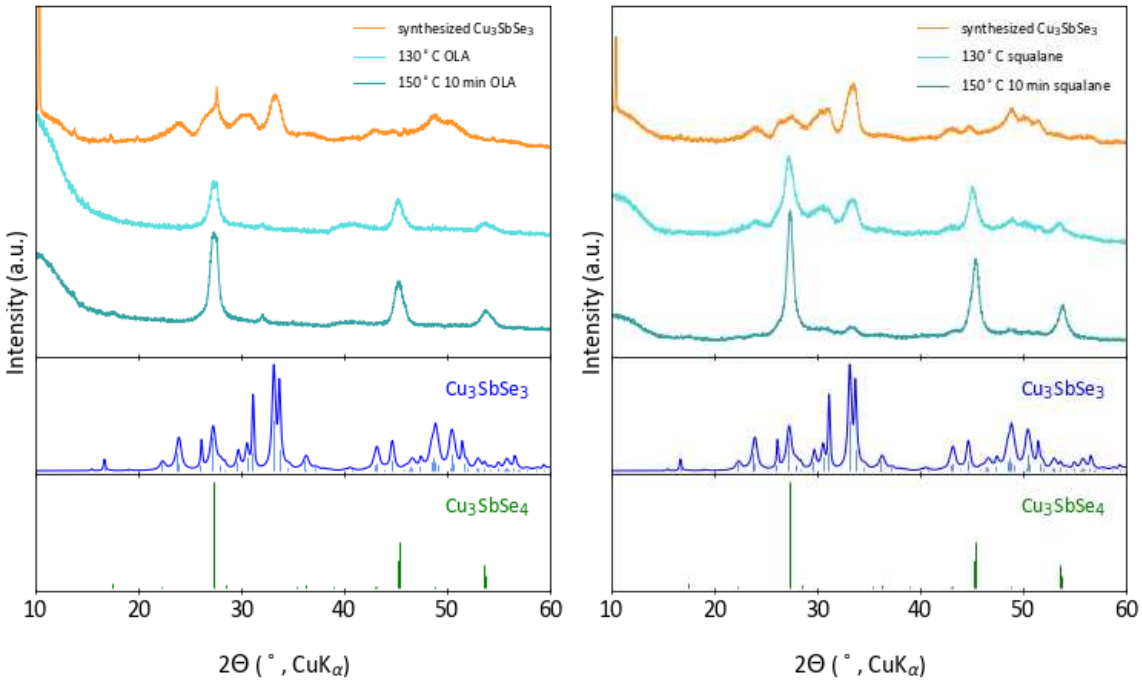

Figure S3.2. PXRD patterns of Cu_3SbSe_3 heating decomposition reactions in different solvents.

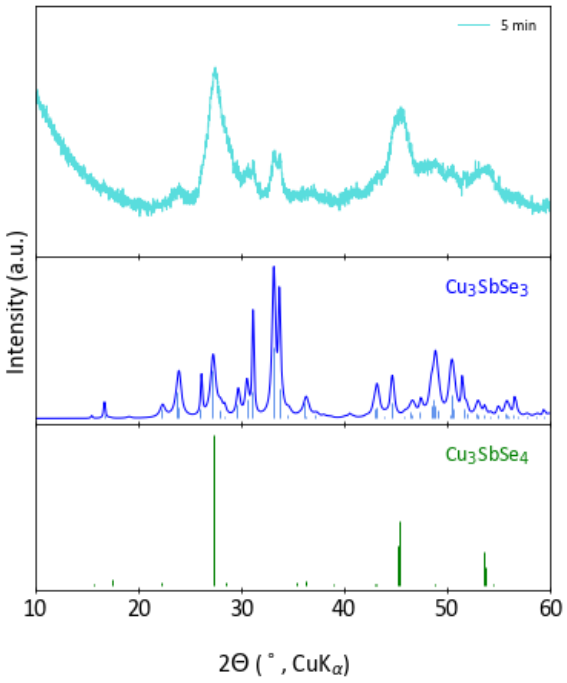

Figure S3.3. PXRD pattern of standard 7 mL OLA reaction with Cu:Sb:Se precursor ratio of 3:1:4.

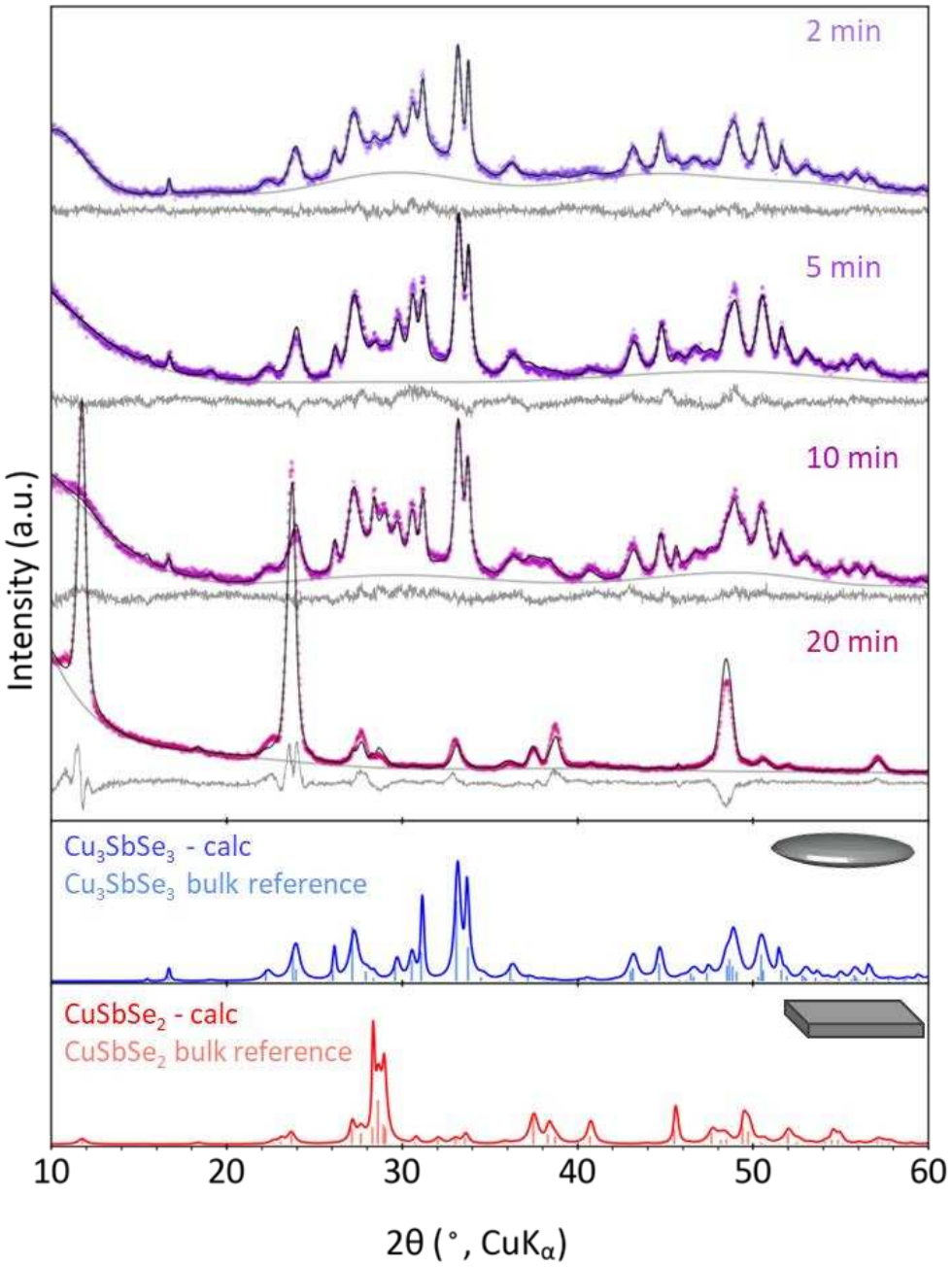

Figure S3.4. PXRD patterns of standard 7 mL OLA synthesis with Rietveld refinements overlaid.

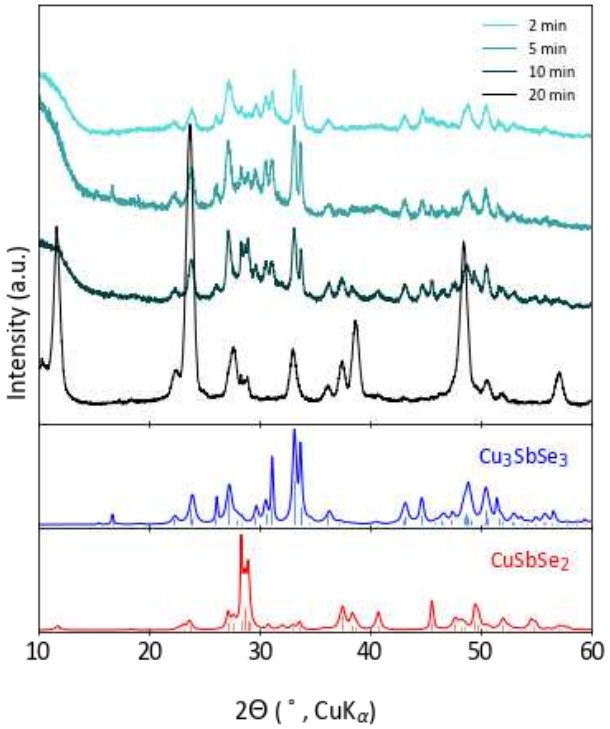

Figure S3.5. PXRD patterns of 7 mL OLA synthesis with LiHMDS.

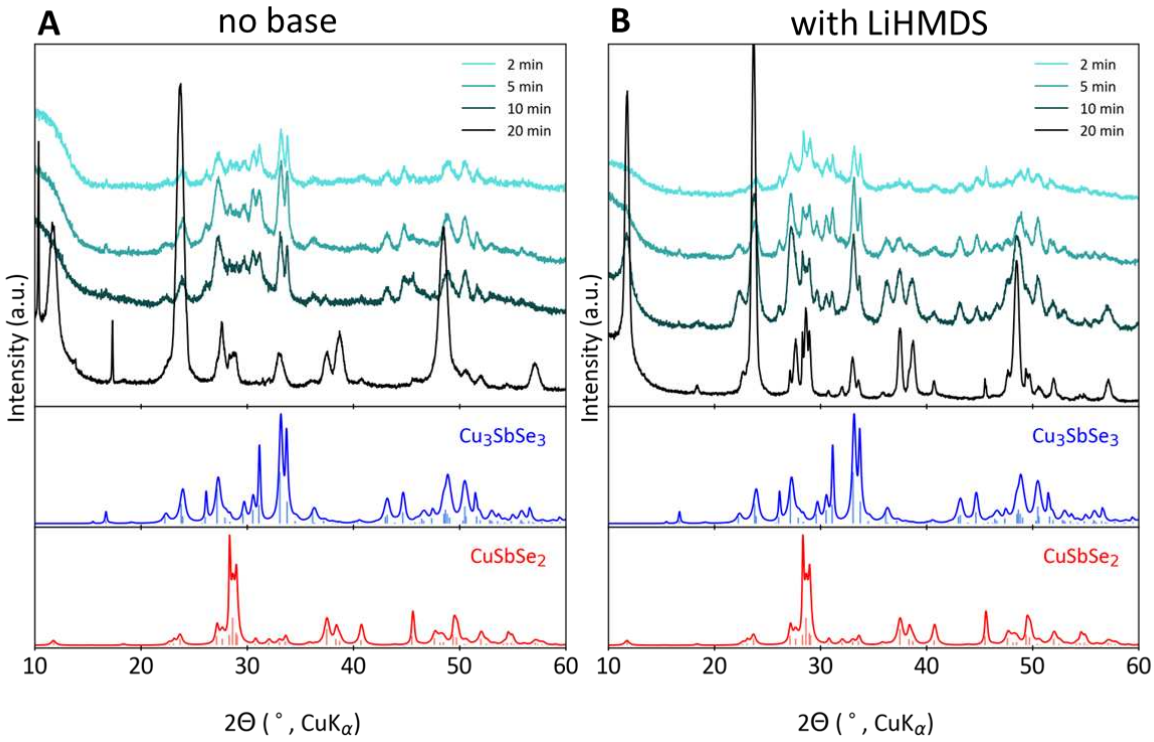

Figure S3.6. PXRD patterns of standard 4 mL OLA synthesis with and without LiHMDS present.

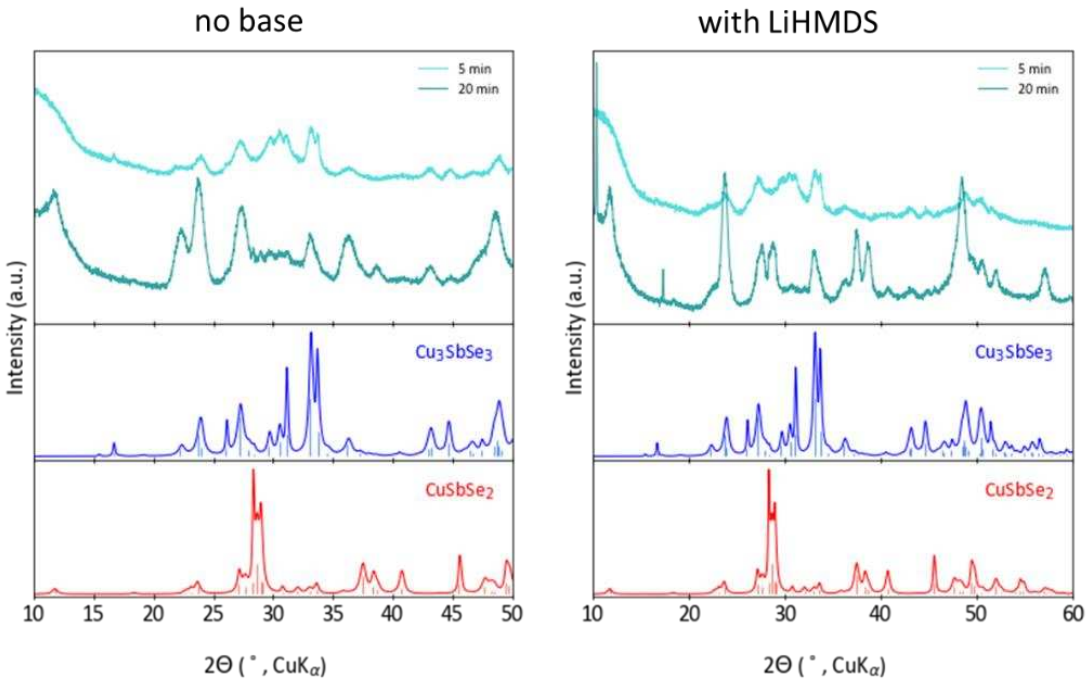

Figure S3.7. PXRD patterns of 4 mL OLA synthesis with 4 mL injection volume of Se precursor.

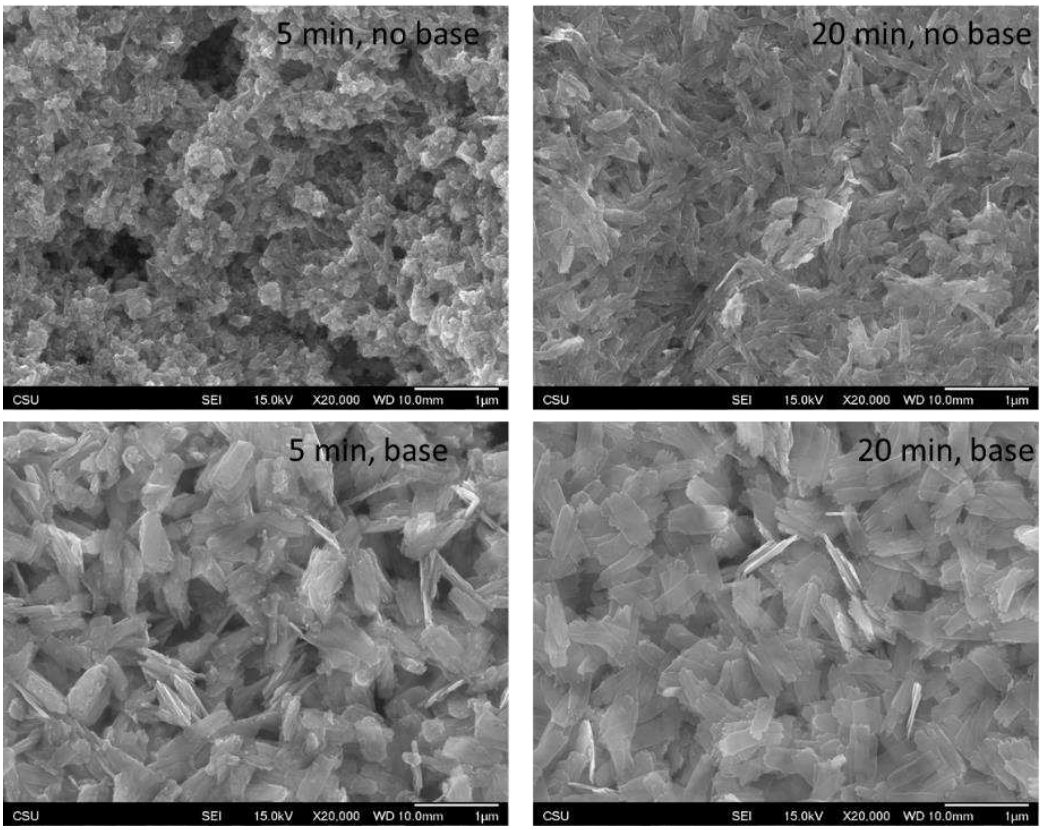

Figure S3.8. SEM images from 4 mL OLA synthesis with and without base present at 5 and 20 min aliquots.

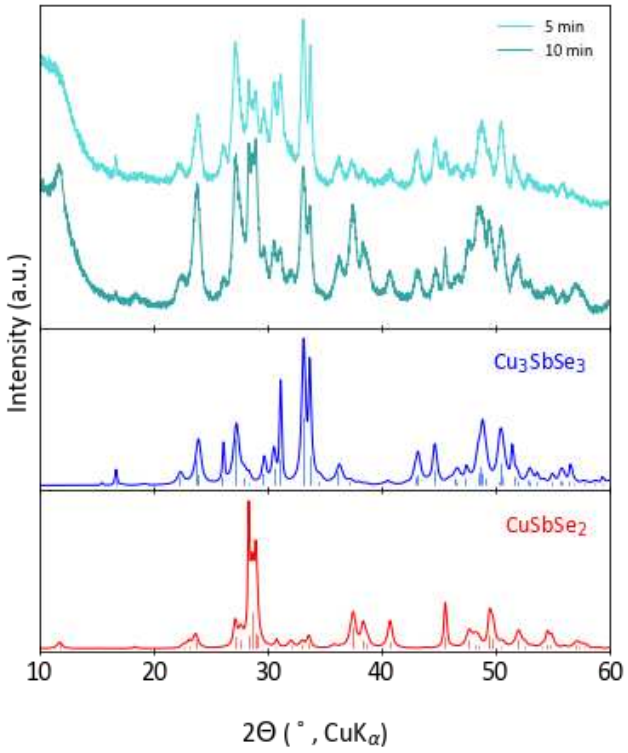

Figure S3.9. PXRD patterns of 7 mL OLA synthesis with n-BuLi.

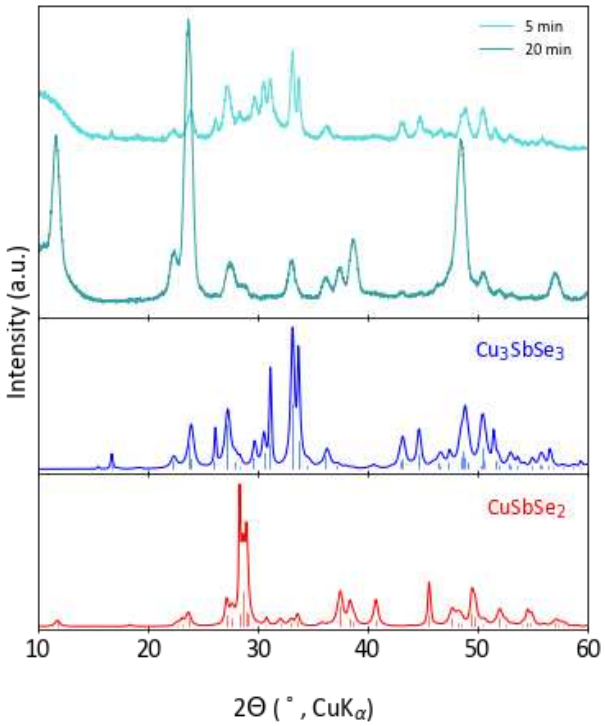

Figure S3.10. PXRD patterns of 7 mL OLA synthesis containing CuCl.

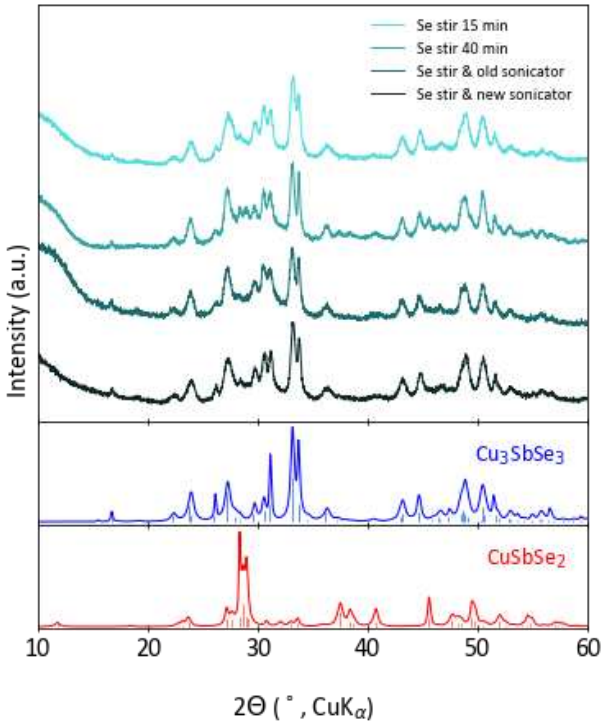

Figure S3.11. PXRD patterns of syntheses with different Se precursor stir and sonicate times.

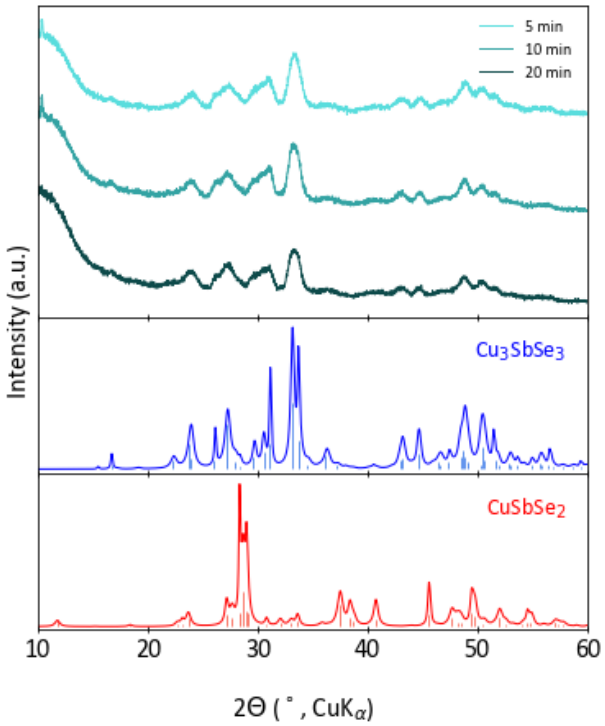

Figure S3.12. PXRD patterns of the excess base reaction containing 7 mL of OLA and 3 mmol of LiHMDS.

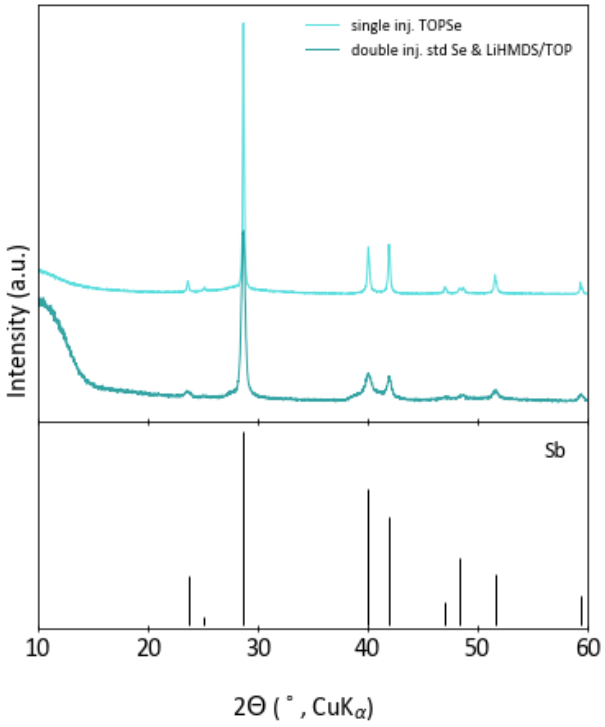

Figure S3.13. PXRD pattern of 7 mL OLA syntheses with injections containing TOP: single injection of TOPSe and double injection of 2 mL TOP and LiHMDS and 2 mL standard Se precursor.

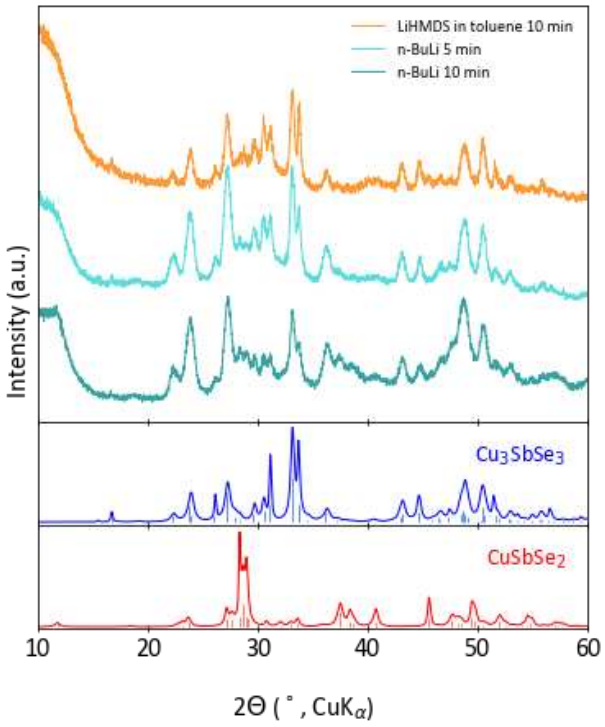

Figure 3.S14. PXRD patterns of base double-injection reactions containing 7 mL of OLA with a 2 mL injection of Se precursor and 2 mL injection base (LiHMDS or n-BuLi).

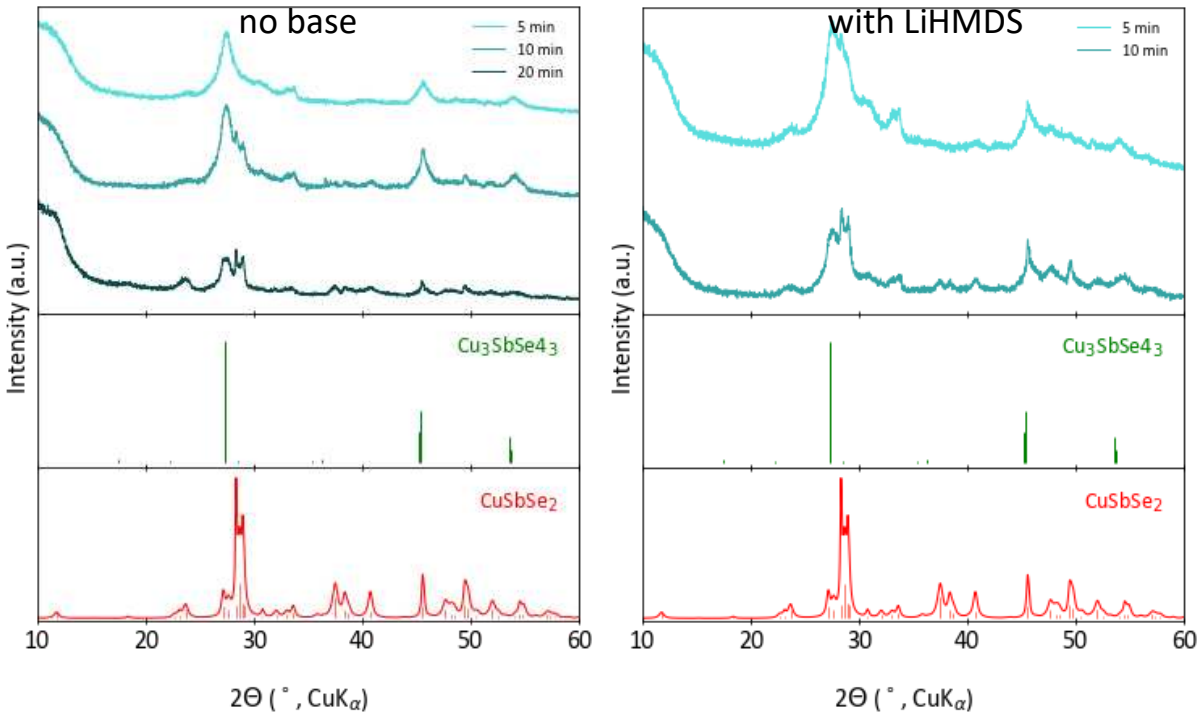

Figure S3.15. PXRD patterns of Sb and LiHMDS double reactions containing 7 mL OLA with 2 mL injection Se and 2 mL Sb injection solution with and without base.

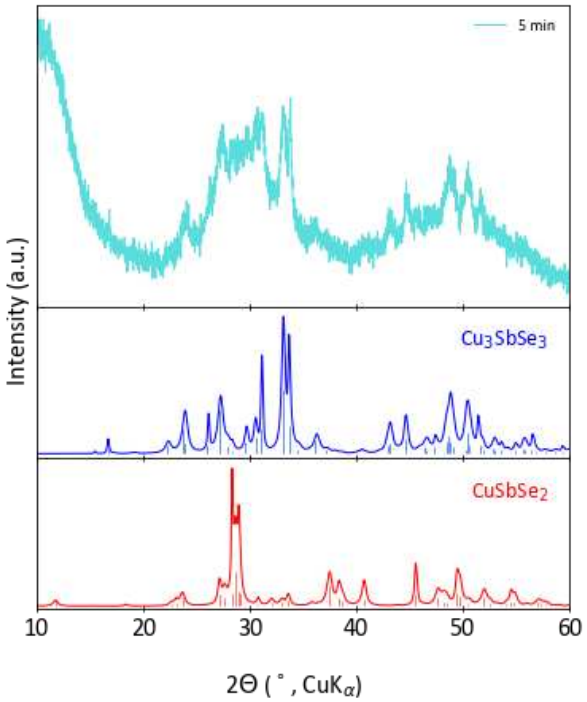

Figure S3.16. Heated LiHMDS and Sb double injection: 7 mL OLA, 2 mL injection Se, 2 mL injection Sb and LiHMDS (heated to 150 °C in flask prior to injection).